Dynamics in Microfluidics Measured by X-Ray Scattering Techniques

Inauguraldissertation

zur

Erlangung der Würde eines Doktors der Philosophie

vorgelegt der

Philosophisch-Naturwissenschaftlichen Fakultät

der Universität Basel

von

Raphael Benjamin Urbani

aus

Basel und Burg/AG, Schweiz

Basel, 2015

Genehmigt von der Philosophisch-Naturwissenschaftlichen Fakultät auf Antrag von:

Prof. Dr. Thomas Pfohl, Fakultätsverantwortlicher
Prof. Dr. Bert Müller, Korreferent

Basel, den 09. Dezember 2014

Prof. Dr. Jörg Schibler, Dekan

Abstract

Small angle X-ray scattering (SAXS) is a powerful technique to analyse characteristics of colloids, polymers and proteins. The large range of scattering vectors allows for investigations of dimensions in the range from a few ångstroms up to some hundred nanometres. Microfluidics incorporates the advantages of small sample volumes and the precise control of experimental parameters. It is thus an ideal tool to investigate a manifold of biological material and reactions. Besides an extensive variability in device fabrication, microfluidics offers easy and fast device production and high reproducibility. We combine X-ray scattering techniques with microfluidics in order to quantitatively describe the dynamics of protein folding. Moreover we analysed the flow behaviour in specific microfluidic devices.

For this purpose, we developed a microfluidic device for fast mixing and X-ray measurements. Soft lithography allowed us to produce microfluidic devices that were readily adaptable for SAXS experiments using synchrotron radiation or in-house setups. By the use of parallel lamination and hydrodynamic focussing, we were able to reduce the diffusion path and thus drastically decrease the mixing time. A very low dead time of 1 ms or less, depending on the flow velocity, and high temporal resolutions are crucial for the study of fast reaction dynamics. The use of hydrodynamic focussing in *y*-direction and specific flow-defining geometries to focus in *z*-direction results in minimal time dispersion (i.e. minimal velocity dispersion inside the sample), which is ideal for in-house SAXS measurements. Accordingly, we were able to measure the dynamics of lysozyme folding with an in-house setup and calculate the corresponding radii of gyration.

As microfluidic devices are used for various types of experiments, such as rheology, it is becoming more and more important to understand the flow dynamics in the channel. We took advantage of the newest generation of

coherent synchrotron radiation to analyse the flow behaviour of complex fluids. Coherent X-ray radiation grants the possibility of correlation spectroscopy, which allows measuring the flow dynamics of colloids. Common X-ray photon correlation spectroscopy (XPCS) uses point detectors to collect the intensity and calculate the autocorrelation function. Here, we used a fast read-out 2D X-ray detector to collect full-frame scattering intensity images. Unlike previous one-dimensional analyses, we calculate the autocorrelation functions for the full, two-dimensional q-range (i.e. pixel-by-pixel for the full image). This leads to sequences of correlation images (one for each τ), or in other words, a correlation movie. The patterns revealed by these images depend strongly on the flow situation in the channel. Consequently, the correlation movies allowed us to determine diffusion constant, flow orientation and flow velocity under different flow scenarios. We could therefore derive information about the device anisotropy directly from the correlation images.

In essence, we developed a new microfluidic device to measure fast reaction dynamics and evolved a method to quickly analyse flow behaviour inside microfluidic channels.

Content

1 Introduction

Incoming light that interacts with a particle sized in the range of the lights wavelength is scattered, i.e., deflected or reflected. The scattering depends mainly on the size but also on the structure and the shape of the particle. Well-known examples for scattering phenomena are the red sky at sunset, the white colour of clouds and milk or the blue sky. If the particle size is small in comparison to the wavelength, the light is scattered in random direction; this phenomenon is known as Rayleigh scattering[1] where light of different wavelengths gets scattered in different angles.
With increasing particle size, i.e. a size range similar to the wavelength, the visible light gets scattered more uniformly (differences in wavelengths are less pronounced compared to the particle size). This effect is called the Mie scattering[2].

Visible light is just a small part of the large spectrum of electromagnetic waves, which also includes radio waves, microwaves or X-rays. The scattering effects described above are valid not only for visible light but for all kinds of electromagnetic radiation. The discovery of X-rays at the end of the 19th century[3] opened up new avenues to investigate smaller structures than was possible with visible light. Subsequently Max von Laue first commented on diffraction of X-rays by crystals[4]. His findings were followed by numerous discoveries around the nature and the diffraction of X-rays[5-7]. The fact that X-rays show diffraction patterns eventually proved that X-rays are electromagnetic waves, similar to those of visible light. One year after the publication of these observations, William Henry Bragg and his son William Lawrence Bragg first defined a relation between wavelength, distance between scattering planes and the scattering angle; the Bragg's Law[8].

$$n\lambda = 2d\sin(\theta) \tag{1.1}$$

Where θ is the scattering angle, d is the separation, λ is the wavelength and n is an integer. The characterization of X-rays and their incorporation into analysing tools led to countless scientific findings during the next one hundred years[6,9,10]. Not only could many mineral structures be solved due to Bragg's Law, also the structures of haemoglobin and myoglobin were understood by means of X-ray crystallography. Moreover, one of the most important discoveries in the 20th century, the crystalline structure of DNA by Rosalind Franklin and its interpretation by Watson and Crick[11] were based on X-ray diffraction studies. Even today, researchers are awarded Nobel prizes for achievements based on X-ray crystallography, for example the unravelling of the structure and function of ribosomes, a catalyst in protein synthesis[10,12-14].

For a long time X-ray diffraction was limited to wide angles and crystallized samples. Towards the middle of the 20th century, an increasing amount of research on X-ray diffraction also included the scattering to smaller angles[15]. As a result, it became possible to study not only lattice constants but also sizes and shapes of particles, making crystallized samples no longer a prerequisite. The initial findings and developments on small angle X-ray scattering (SAXS) and small angle neutron scattering (SANS) were mainly propagated by André Guinier, Otto Kratky, Peter Debye and Günther Porod[16-20] (in chronological order). The main focus was on the orientation and periodicity of protein fibres such as cellulose[21-23], on colloidal systems[17] and on polymers[24]. In the late 1950s, catalase was characterized using small angle scattering[25] and after the start of ab-initio modelling by Svergun in the 1990s[26] the number of publications regarding small angle scattering increased rapidly.

1.1 Small angle X-ray scattering (SAXS)

Compared to wide angle X-ray scattering (WAXS) and diffraction, with scattering angles up to 180° in SAXS the angles measured are usually below one degree. As mentioned above, light interacts with matter that has a size in the range of its wavelength. The spectrum of X-rays ranges from 1 picometre (pm), which is 10^{-12} m, up to 10 nanometres (nm), which is 10^{-8} m. The wavelength used for SAXS depends on the X-ray generator used. Sources used in conventional laboratories accelerate electrons onto a metal anode, where a spectrum of X-rays is emitted. This spectrum is very specific for the anode material. Generally, copper is used as anode, resulting in a wavelength of 1.54 Å, with one Å being 0.1 nm. In synchrotron facilities the X-ray radiation is produced by the acceleration of electrons (i.e., the change of flight direction induced by magnets). The so-called "bremsstrahlung" is emitted tangentially to the electrons orbit and has a spectrum ranging from 10^{-11} m (0.1 Å) to 10^{-4} m (long infrared and short microwaves). Furthermore, by applying monochromators and filters, the wavelength can be changed and adapted to the corresponding experiment.
Figure 1.1 shows the evolution of the brilliance of X-ray sources.

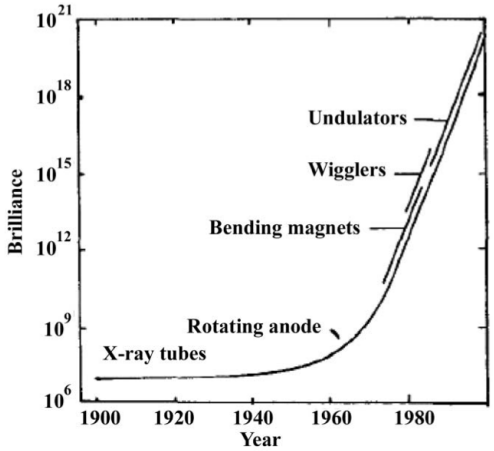

Figure 1.1: Temporal development of the intensity of X-ray sources. The unit of brilliance is [photon/s mm2 mrad2 0.1% bandwidth]. Taken from [27].

In X-ray diffraction, the sample needs to be in a crystalline conformation and parameters such as lattice constant or orientation are measured. However, while typical diffraction angles are above 2°, in SAXS the measured angles are usually below 2° or 1° and thus larger dimensional parameters of the sample, such as its size, shape and orientation are of interest. When measuring in solution, which is often the case for SAXS, the sample is isotropic. In other words, the particles can freely rotate and present themselves in different spatial orientations. The isotropy of the particles leads to a 2D scattering signal with a rotational symmetry (i.e. rings or circles), as scattering in different directions occurs with the same probability. The rotational symmetry of the recorded scattering image allows for an azimuthal averaging (for each scattering angle 2θ, the intensity is averaged over all scattering directions χ). As follows, we obtain a 1D plot with scattering intensity on the *y*-axis and scattering angle on the *x*-axis.

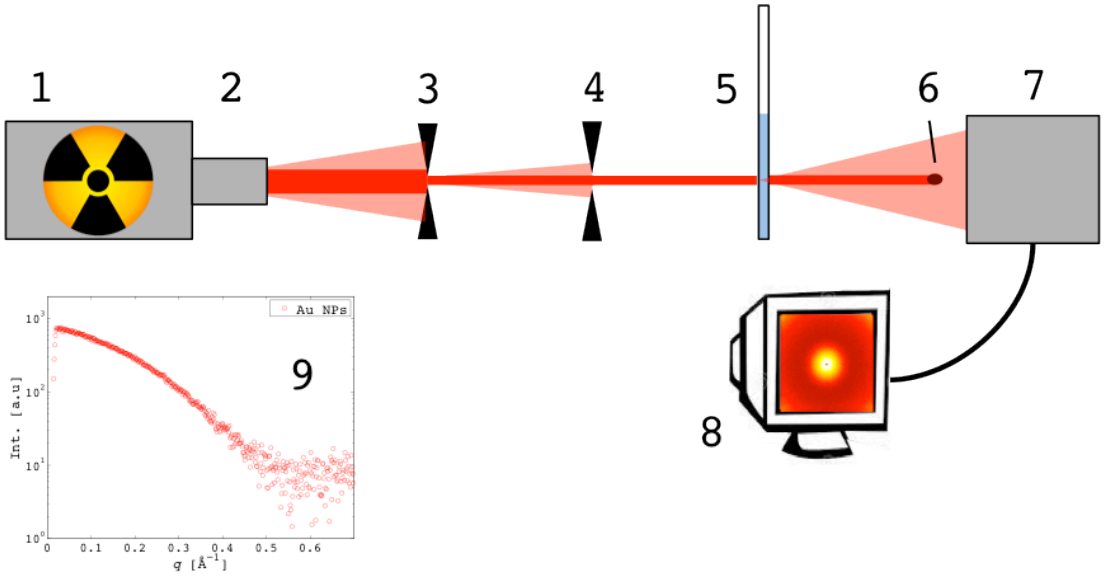

Figure 1.2: Scheme of a typical SAXS setup. With X-ray source (1), mirrors or filters for beam alignment and monochromation (2), beam defining aperture (3), pinhole for parasitic scattering (4), sample (5), beamstop to block direct beam (6), detector (7), computer (8) to collect and analyse the data and an example of a scattering plot (9) after azimuthal averaging.

Figure 1.2 shows a typical setup of a small angle scattering experiment. The X-ray source generates radiation, which is filtered and aligned to a parallel beam. An aperture, this can be lenses, slits or pinholes, defines the size of the beam. To

avoid undesired parasitic scattering from the aperture, another pinhole or filter is usually installed shortly upstream of the sample. To minimize the loss of radiation by scattering with air, the beam path between source and sample is kept under vacuum. Whether the sample is kept under vacuum or not depends on the type of sample and on the SAXS setup. At synchrotron facilities, samples are not kept under vacuum because on one hand, small sample chambers are lacking and on the other hand the intensity loss due to air scattering is negligible compared to the high beam intensity. In contrast, in-house – setups have a much lower intensity ($I_{0,\,\text{synchrotron}} \approx 10^{24}$, $I_{0,\,\text{in-house}} \approx 10^{18}$, the unit is photons/s/mm^2/mrad^2/0,1%BW in both cases) and therefore, samples are often measured under vacuum to avoid loss of intensity through air scattering. As a consequence, the sample has to be protected from evaporation, which for instance can be achieved by using a flame-sealed glass capillary. To avoid saturation of the detector and hence signal loss, a beamstop (usually a piece of lead) is placed behind the sample, i.e. directly in front of the detector. Finally, data is collected on a computer.

For a diluted solution of spherical particles, the size of the particles directly correlates with the angle of the scattered X-ray beam. As indicated by Braggs Law (1.1), the correlation is inversely proportional.

In the small angle regime, it is plausible to assume that no long-range order exists when measuring in solution. This means, that there is no correlation between two particles as they are far enough apart. Hence, only one single particle needs to be considered[28].

The actual property that is measured in SAXS is the difference between the electron densities of the sample (ρ_s) (i.e. particles in a solution), and its surrounding matrix (ρ_0) (i.e. the solvent). Accordingly, if $\rho_s = \rho_0$, the particles cannot be distinguished from the solvent by X-rays (i.e. the X-ray beam doesn't "see" them), and no signal will be measured. The established parameter used to plot the scattering intensity is the momentum transfer q, or the scattering vector.

It is defined by the scattering angle 2θ (see figure 1.3) and the X-ray wavelength λ as

$$q = \frac{4\pi \sin(\theta)}{\lambda}. \tag{1.2}$$

The typical unit for q is $Å^{-1}$ or nm^{-1}, again showing that the scattering intensity is depicted in reciprocal space, which means that bigger q-values correspond to smaller scattering objects.

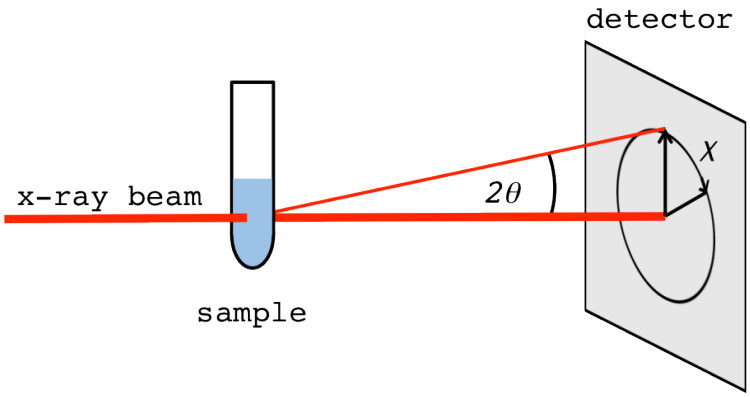

Figure 1.3: Sketch of the small angle scattering of a sample. The scattering angle (2θ), scattering vector (q) and orientation angle (χ) are outlined.

A SAXS intensity curve of spherical particles can be analysed in different ways. First information about typical length scales (d) in the sample can be calculated using equation 1.3, where q is the location of the scattering intensity feature (i.e. a peak or a minimum).

$$d = \frac{2\pi}{q} \tag{1.3}$$

André Guinier found the first approximation that apparently fits all kind of particles. It is thus known as the Guinier-approximation and used to calculate the size of the particles[29]:

$$\ln\left(I\left(q\right)\right) = \ln\left(I\left(0\right)\right) - \frac{1}{3}R_g^2 q^2 \,. \tag{1.4}$$

When plotting the logarithm of the scattering intensity versus q^2, the intensity will show a linear decay at very small q-values that only depends on the radius of gyration, R_g. It is defined as the mean square distance from the centre of gravity, where mass is given by the electrons[28].
The behaviour of the scattering intensity at higher q-values can be approximated using equation 1.5, where S is the surface of the particle.

$$I\left(q\right) \propto S \cdot q^{-4} \tag{1.5}$$

This fourth power law, known as "Porod's Law", was independently described by Günter Porod[30] and Peter Debye[31] and is applied to the final slope of the scattering intensity[28]. Nowadays analysis methods, such as those described by Guinier and Porod, are included in various computer software, like Primus[32].

1.1.1 X-ray photon correlation spectroscopy (XPCS)

In classical X-ray scattering experiments, the large diffracted beam includes many small coherence volumes (i.e. small volumes with coherent radiation, D_i). Over all, only an incoherent sum of the intensities ($A_i(q)$) of many of these domains is measured[27].

$$I\left(q\right) = \sum_{i \in N} \left|A_i\left(q\right)\right|^2 \tag{1.6}$$

The high brilliance of third generation synchrotron sources opened the possibility to obtain coherent X-ray beams of reasonable intensity and of nearly macroscopic dimensions. The coherent X-ray beam is obtained by selecting a part of the incoherent beam in the two transverse directions[27]. This is mostly

achieved by using slits. This part of the originally incoherent beam needs to fulfil the following conditions for diffraction:

$$\sigma\sigma' \cong \frac{\lambda}{4\pi}, \tag{1.7}$$

where σ' is the root mean square divergence of the beam and σ is the root mean square beam size. This condition applies to fully coherent Gaussian beams, however, in practice the beam cannot be considered Gaussian due to limitations of the optics. Consequently, conditions for obtaining an X-ray beam with good coherence are:

$$\Phi\varepsilon \leq \lambda, \tag{1.8}$$

where Φ is the size of the beam defined by a slit aperture or pinhole and ε is the full width at half maximum (FWHM) divergence of the beam[27].

Initial coherent scattering methods were developed and used for studies of fluctuations in dynamic processes. The scattering of a coherent beam leads to interference signals, which are no longer averaged out as in equation 1.6. These interference signals are called speckle patterns and show fluctuations if the scattering object is moving. The fluctuations of the intensity is analysed by means of an intensity-intensity correlation function (equation 1.9) in analogy to dynamic light scattering (DLS)[27,33].

$$g_2(q,t) = \frac{\langle I(q,t) \cdot I(q,t+\tau) \rangle}{\langle I(q,t) \rangle^2} \tag{1.9}$$

For intensity autocorrelation, the intensity at a given time point t ($I(q,t)$) is correlated with the intensity at a time point shifted by τ ($I(q,t+\tau)$) at a constant q-value. The transposition of this method to X-ray scattering is called X-ray

photon correlation spectroscopy (XPCS) and has two main advantages compared to DLS. First, the ability of X-rays to observe order fluctuations in the vicinity of Bragg peaks, i.e. at very small sizes (larger q-values) and second their high penetration depth that renders studying opaque materials or strongly multiplies scattering samples[27].

In order to measure fast dynamics with XPCS, small τ and large beam intensities are needed. The latter is given by the latest synchrotron radiation, whereas for small τ (i.e., fast detection), slits and point detectors, in particular an avalanche photo diode (APD), proved most efficient for studying fast phenomena. The apertures of these detectors (~ 10 µm), the commonly used sample to detector distances (2 – 5 m) and the typical wavelength (1.6 Å) determine the beam diameter used for XPCS, which is often 5 – 10 µm (equation 1.8)[27].

The use of point detectors limits XPCS experiments to a very small q-range (basically one q-value) and one scattering direction per measurement. Recent advances in the development of fast 2D detectors such as the MAXIPIX[34] or the Eiger[35], with frame rates up to MHz at full frames enable the collection of whole scattering images during XPCS measurements. This will open new possibilities such as the analysis of the autocorrelation function of whole images, as well as simultaneous cross correlation between two different points (i.e. two different q-values or two different scattering directions)[27,33,36].

1.2 Microfluidics

The term microfluidics describes the science and the technology of small fluid systems (i.e. small dimensions of fluid channels or particles in flow). The dimensions range from atto- to nanolitres (10^{-18} to 10^{-9} l) of fluid volume and from one to several hundred micrometres in channel width or particle size[37]. This already points out one of the many advantages of microfluidics: very small sample volumes. Other advantages include precisely controllable environments, high resolution and sensitivity as well as very low fabrication costs[37,38]. Most

characteristics of microfluidics are based upon the laminar flow behaviour. Laminar flow occurs when mass transport is dominated by viscous dissipation and inertial forces are negligible. As inertia provides the nonlinearity responsible for turbulence flow, the laminar flow regime is free of turbulences[39].

The absence of turbulences can be explained by the fact that in the case of very small dimensions, the fluid velocity is smaller than the velocity of pressure waves in the liquid. The fluid can hence be considered incompressible[40]. The velocity field of an incompressible fluid is described by the Navier-Stokes equation[39,41]:

$$\rho\left(\frac{\partial v}{\partial t} + v \cdot \nabla v\right) = -\nabla p + \eta \nabla^2 v + \rho g + \rho_{el} E \,, \tag{1.10}$$

where ρ is the density, η the viscosity and v the velocity of the fluid. E is an electric field, ρ_{el} is the charge density, p the pressure and g the acceleration due to gravity. The left side of the equation resembles the inertial forces, while the right side represents both the intrinsic and applied forces. To perceive whether a system is in the laminar flow regime or not, one has to compare the two parts of the Navier-Stokes equation. This is done by calculating the Reynolds number, Re which resembles the ratio of the inertial and the viscous forces[39,42]:

$$Re \equiv \frac{f_i}{f_v} = \frac{\rho v l}{\eta} \,, \tag{1.11}$$

with $f_i \sim \rho v^2/l$ and $f_v \sim \eta v/l^2$, where l is the characteristic length of the system (i.e. the channel width, or particle size). For microfluidic devices where viscous forces dominate, $Re << 1$, whereas for large systems where inertial forces dominate, $Re >> 1$. Owing to the small size and low velocity of a microfluidic environment with $Re << 1$, we can neglect the inertial term of the Navier-Stokes equation (1.10). Similarly, gravitation can be neglected due to the small volumes

handled in microfluidics, and no electric fields are applied, such that the Navier-Stokes equation can be simplified to the linear Stokes equation.

$$0 = -\nabla p + \eta \nabla^2 v \,. \tag{1.12}$$

Similar to the Reynolds number, there are many other dimensionless numbers to characterize a fluidic system. Besides *Re*, one of the most commonly used number in microfluidics is the Péclet number *Pe*. The dominance of viscous forces in a microfluidic environment leads to the situation, that lateral transfer of molecules in the channel happens mainly through diffusion. The Péclet number calculates the ratio of diffusion time versus flow time[39].

$$Pe \equiv \frac{t_D}{t_F} = \frac{vw}{D} \sim \frac{Z}{w}, \tag{1.13}$$

where $t_D \sim w^2/D$ and $t_F \sim w/v$ and Z is the distance along the channel. D is the diffusion constant and w the channel width. Knowing the diffusion constant, channel width and flow velocity, we can therefore use *Pe* to calculate the channel length needed for a given molecule to distribute evenly.
Furthermore, The diffusion-controlled transport enables the control of concentrations inside such a device. The special conditions associated with microfluidics entail a huge diversity of applications. Figure 1.4 shows some of the possibilities in microfluidics, where liquid interfaces are used[43].

Floating interfaces (figure 1.4 A) are used to produce well-defined microfluidic droplets using two immiscible fluids. Surface wettability and flow rates give a perfect control over droplet size, which makes such devices ideal for commercial uses with parallel, high throughput droplet formation[43]. Consequently, double emulsions can be used to form vesicles or single emulsions as nanoreactors for chemical or biological processes, providing smallest sample volumes and high reproducibility. The versatility of microfluidics allows numerous manipulations

of the droplets, including coalescence, sorting, mixing of the content, splitting or storing[43,44].

Pinned interfaces (figure 1.4 B) provide a two-phase flow supported by different surface treatments for each of the streams. These streams can be two immiscible fluids or air and liquid[45,46]. The large surface to volume ratio of these interfaces allows efficient transport between the two streams. This makes the pinned interface setup attractive for various applications such as the study of drug partitioning, enzymatic reactions, multiphase, phase-transfer or interfacial reactions[43,45,47-49].

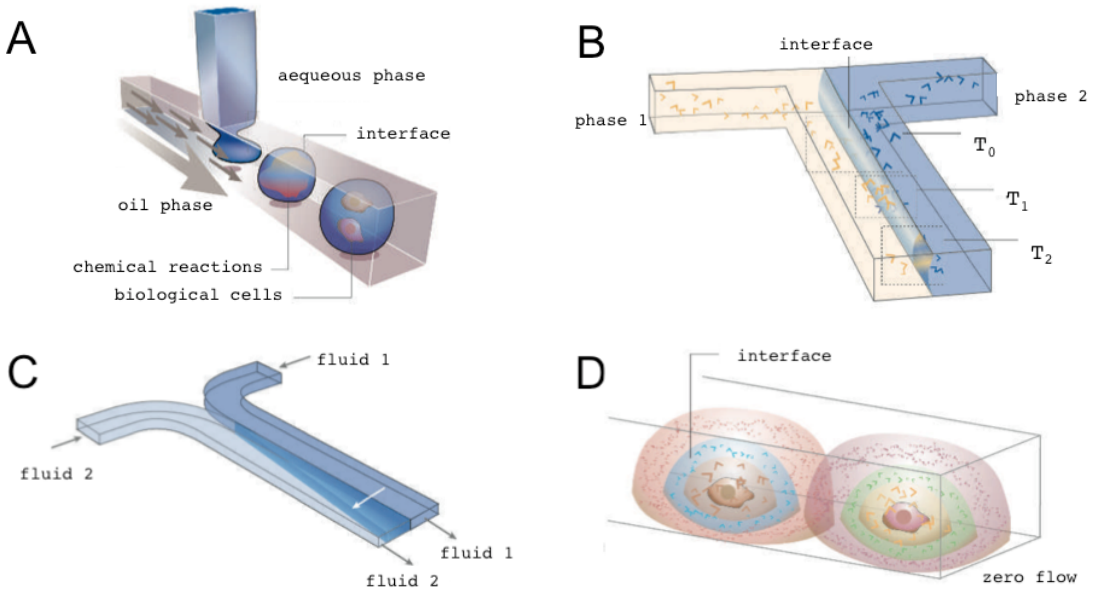

Figure 1.4: Four different applications of microfluidic devices providing liquid interfaces. A: floating interface used to create droplets with two immiscible fluids. B: pinned interface of two immiscible fluids, suitable for investigating interface reactions. C: moving interface between two miscible fluids often used as filtering or mixing device. D: secondary interface of convection-free environments. Taken and modified from [43]

Using a similar design as for pinned interfaces but with two miscible fluids produces a moving interface (figure 1.4 C). Due to the laminar flow, mixing between streams occurs only through diffusion. The extent of mixing is controlled by specific channel dimensions and flow rates (cf. Péclet number). A high *Pe* results in a kinetically stable and sharply defined interface whereas at

low *Pe* a complete mixing occurs. This setup was first established for protein fractioning[50-52] and subsequently developed into the 'H-filter', which illustrates the potential of diffusion and laminar flow[53,54]. An attractive feature of the 'H-filter' and particularly the 'T-sensor'[55] is the fact that the time available for diffusion and reaction correlates with the travel distance of the fluid. This allows the observation of reaction kinetics, binding affinities, analyte concentrations and the calculation of diffusion constants[43,56].

The dominating viscous forces in microfluidic systems allow not only the fabrication of flow-controlled devices but also of purely diffusive, convection-free environments (*Pe* = 0). These secondary interfaces (figure 1.4 D) are diffusive layers, which depend on the rate of solute release at the source and on the solutes diffusivity. Additional constraints such as impermeable microchannel walls make the system even more predictable. The usage of secondary interfaces in microchannels is versatile and includes studies of protein crystallization, cell division and migration and intercellular communication[43,57]. The introduction of microchambers as flow-free microfluidic environment creates an even more controllable and predictable type of secondary interface to study biological systems[58].

1.2.1 Mixing in microfluidics

Miniaturization, integration and automation led to the rapid evolution of microfluidics and a simultaneous development of heterogenuous "micro"-devices for microfluidic applications. Examples include micropumps, microreactors and micromixers[59]. Mixing in particular has become an important part of microfluidics as it is currently widely applied in chemistry and biology (cf. figure 1.4). The need for more efficient and faster mixing devices produced many different types of micromixers. They can be classified into two main categories: active and passive micromixers[60].

While active mixing devices work with many different modes of external impact, such as acoustic, thermal, magnetic or electrodynamic disturbances, in passive

micromixers transport happens mainly by diffusion[60]. The most common passive mixing devices are based on a moving interface (figure 1.4 C), allowing the substances to diffuse between the different fluid streams. Following the basic T-mixer and Y-mixer[61-63], the systems were improved over time to shorten mixing times. There are two main types of passive mixers: In lamination micromixers, the two inlets are split into several parallel substreams which are fused to form one stream with alternating parallel substreams. In injection micromixers, only the solute flow is split into many streams that are injected into one solvent flow. Other types of passive micromixers include droplet mixers (figure 1.4 A) and micromixers based on chaotic advection[60].

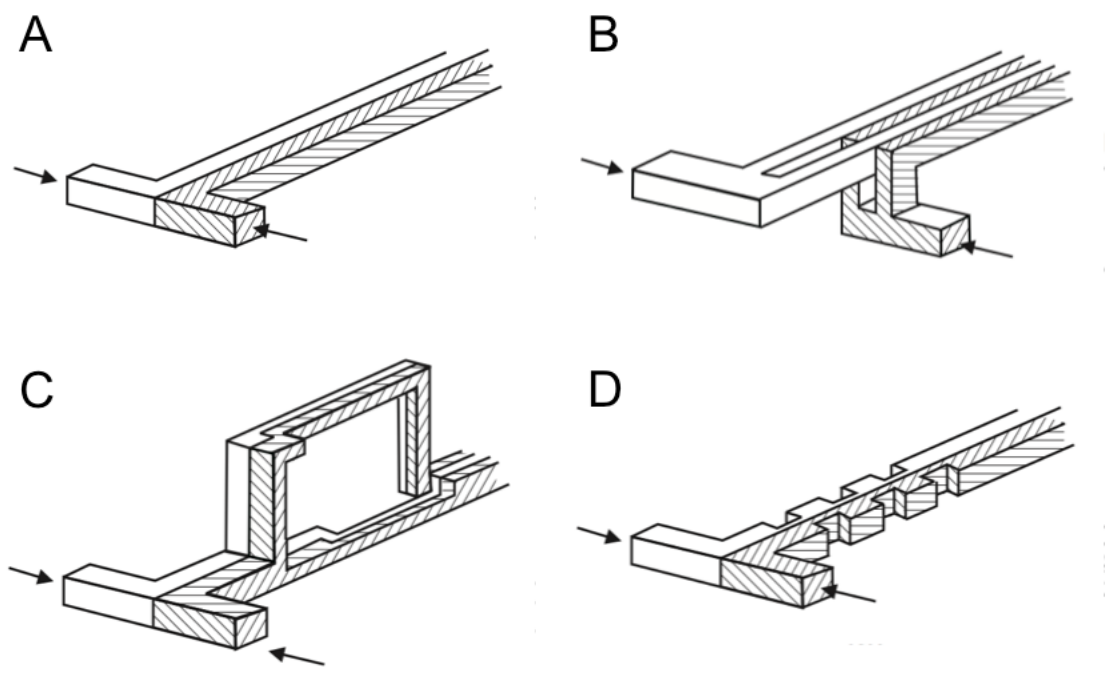

Figure 1.5: Different passive micromixers. A: the basic T-mixer. B: mixer using parallel lamination. B: an example for serial lamination. D: introduction of chaotic advection. Taken and modified from [60].

The main point of lamination mixers is the shortening of the diffusion path for the mixing fluids[64]. The easiest way to achieve this is by hydrodynamic focussing. Controlled by flow velocities, the width of the focussed jet can be varied and it is possible to follow chemical or biological reactions[65]. For very narrow jet dimensions, however, the sampled volume (i.e. protein) becomes less. Hence,

multiple parallel streams are favoured if mixing should be fast without losing sampled volume. Decreasing the diffusion length by these means significantly reduces the channel length and, in parallel, the time needed for complete mixing[60,66-69]. Figure 1.5 shows an overview over different passive micromixers.

1.2.1.1 Hydrodynamic focussing

As mentioned earlier, a smaller diffusion path (i.e., narrower sample streams) is one of the main parameters in fast mixing. Hydrodynamic focussing devices have two lateral buffer streams that focus a sample stream in the middle. Like this, the diffusion length for particles in the buffer streams into the middle stream is much shorter compared to a simple T-mixer[65,70]. The width of the sample stream can be controlled by the relative flow rates of the different inlets. Due to no-slip boundary conditions, the flow velocity at the walls is zero, and a maximal flow velocity occurs in the middle of the channel[42]. Thus, the sample stream here has a uniform flow velocity, and measurements along the jet can reliably be assigned to specific reaction times.

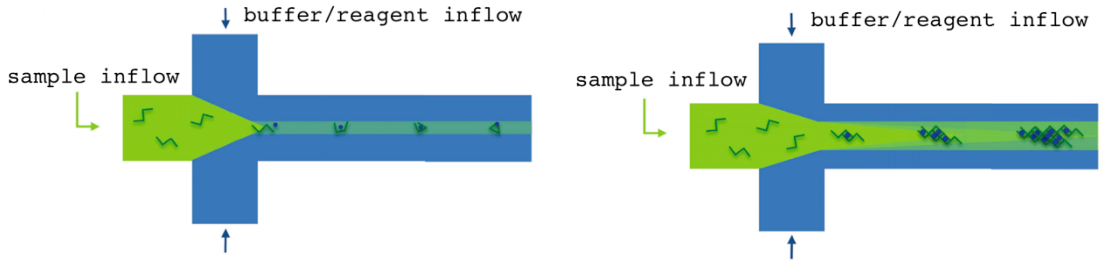

Figure 1.6: Two types of hydrodynamic focussing. Narrow sample stream enabling fast mixing and measurements at different reaction times. Wide sample stream creating a gradient along the flow axis enabling measurements of concentration dependent reactions. Taken and modified from [70].

There are two main operation types of a hydrodynamic focusing device (figure 1.6)[71]. First, applying relatively high flow rates for the focussing buffer results in a narrow middle jet. Like this, the reactants will be completely mixed after a short time, and the flow axis corresponds to the reaction axis enabling measurements at different time points during a reaction. This setup enables the

adaption of exposure times to the experimental needs without loosing the temporal resolution[70].

The second application of a hydrodynamic focussing device creates a wider sample/middle stream resulting in slower mixing. In this case, the reactants mix over time along the flow axis, thus creating a concentration gradient in the middle stream. This allows measurements of concentration dependent reactions[70].

All these features of hydrodynamic focussing provide a perfect environment to study biological reactions such as the fibre formation of silk[72,73], assembly of cytoskeletal proteins[74] or the interaction of DNA with H1 histones[75] and cationic dendrimers[76-78]. Thanks to these circumstances, it was possible to measure intermediate steps of reactions that are usually not accessible in bulk measurements[70,79,80].

1.3 SAXS meets microfluidics — a powerful combination

The combination of microfluidics and small angle X-ray scattering offers a wide spectrum of applications. Advantages of both techniques are united, for example the small sample volumes needed, the precisely controllable experimental environment and the cheap fabrication of microfluidics as well as the wide range of momentum transfer of X-rays. Especially in biological systems including cells and cellular components, length scales between nano- and micrometres apply[70]. However, the small dimensions of microfluidic channels ask for a narrowing of the X-ray beam without compromising its intensity. Newest generation of synchrotron sources provide peak brilliances that can be focused down to micrometres or even several nanometres[81-84]. Small beam sizes are also prerequisite for microfluidic devices using hydrodynamic focussing[81-83]. In this case, the sample stream has a small width of a few micrometres and hence a small X-ray beam of similar dimensions helps to prevent dilution of the signal[70]. The combination of very small X-ray beams with hydrodynamic focussing allows

measurement of reaction kinetics at high temporal resolution. The continuous flow in the channel provides the possibility of long measuring times at the same spot in the channel, without radiation damage on the sample[70]. In this way, reaction kinetics of fast-folding proteins (cytochrome c, *β*-lactoglobulin)[81,82] and folding of RNA and DNA[76,83] could be measured.

The high beam intensities of newest generation synchrotrons demanded new kinds of microfluidic devices. The strong scattering signal and the absorption of X-rays of standard PDMS/glass devices makes them unsuitable for many X-ray studies. The goal is to have at the same time a minimal scattering signal from the device and a high resistance to intense radiation. Although a well-defined low background signal could be subtracted from the data, polymer-based materials, such as PDMS, frequently suffer from radiation damage and hence change signal in the process of a measurement[70].

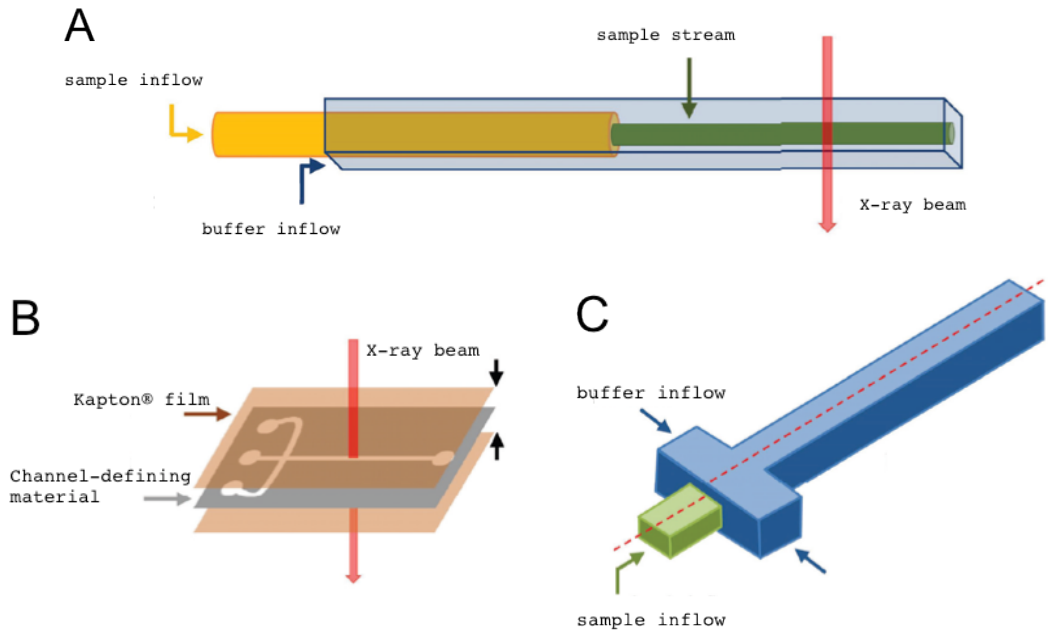

Figure 1.7: Different approaches for SAXS compatible microfluidic devices. A: glass capillary device. B: Kapton® film device with channel defining material, such as steel plate, PDMS or NOA 81. C: 3D device for mixing conditions similar to the glass capillary device with no wall contact. Taken and modified from [70].

Glass capillary devices[72] (figure 1.7 A) with thin walls down to 50 µm thickness are a good alternative. In addition, tube-in-tube geometries[85] offer a way to avoid wall contact of biological molecules, which otherwise tend to stick on surfaces and thus lead to clogging of the channel[70]. However, since devices made of glass capillaries are not as versatile as standard microfluidic ones, other materials have also been investigated. Beside the requirements for X-ray usage mentioned above, the expectations regarding these materials are the same as for standard microfluidic channels: stability, flexibility in channel geometry and dimensions as well as easy manageability[70]. One alternative material proved to be Kapton (polyimide), which is relatively resistant not only to high intensity radiation but also to solvents and has a very weak X-ray scattering signal[86]. Several channel-defining materials between the two Kapton foils or tapes have been used so far; stainless steel plates despite their limitations in geometrical diversity[87], PDMS[71,88] or Norland Optical Adhesive 81 (NOA 81)[74] (figure 1.7 B).
All these materials fulfil the requirements for versatile, X-ray compatible microfluidic devices. Nevertheless, the problem of adsorption of biomaterials to the walls remains. In addition, the parabolic flow profile leads to a high velocity dispersion across the channel which makes it difficult to assign reaction times to positions along the channel. One way to overcome this problem are droplets; here the whole sample volume moves at the same velocity, but the interface between droplet and carrier fluid might affect the X-ray scattering measurement. In studies on protein solutions in flow focussing geometries[73,74] both issues, velocity dispersion and sample adsorption, were overcome by using 3D devices that have been fabricated by multi-layer soft lithography (figure 1.6 C). The principle is similar to the glass capillary device, however, the NOA 81 devices show severe beam damage for higher X-ray intensities[70]. To meet all challenges it is thus most useful to combine different materials and designs. For example, PDMS-capillary devices for protein crystallization combine the functionalities of controlled mixing in PDMS channels with the advantage of good SAXS properties of the glass capillaries[89,90].

1.4 In-house SAXS and its advantages

In the 1950s, Otto Kratky invented the first SAXS setup for laboratories, the Kratky camera[91]. Ever since, in parallel to synchrotron radiation, lab sources evolved rapidly. The intensity of in-house X-ray sources is significantly lower compared to synchrotron radiation (nowadays 10^6 times lower peak brilliance). Hence, first publications about experiments performed on laboratory SAXS systems mainly covered strong scattering materials such as gold or silica structures[92,93].

The advantages of an in-house SAXS setup are obvious. While measurements at synchrotrons require long term planning and visits to synchrotron facilities, in-house experiments can be performed at any time and on short notice. The ability to react to results or to adapt setup or experimental' conditions is another big plus. Improvements in laboratory X-ray sources and setups led to an increase of research on in-house setups in recent years[94-97]. The smaller beam intensity of lab-sources compared to a synchrotron facility can be compensated by longer exposure times. This is rarely a problem as less or no radiation damage occurs at in-house setups.

Despite the requirement for new experimental approaches (i.e., new microfluidic geometries), SAXS in combination with techniques like microfluidics, stopped flow devices or Raman spectroscopy[94,97] offers exceptional control and flexibility of the conditions that influence measurements[97].

1.5 Goals of the thesis

In this work, we combine X-ray scattering techniques and microfluidics in order to measure the dynamics of biological reactions and Brownian as well as convective motion.

For this purpose we create a microfluidic mixing device with very short (1 ms or lower) mixing times on one hand, but also a narrow velocity dispersion in both

transversal directions and thus a high temporal resolution for SAXS measurements on a laboratory setup on the other hand. High temporal resolution and fast mixing time will allow for measuring the folding dynamics of fast folding proteins such as lysozyme.

Moreover, fast 2D X-ray detectors are used for full *q*-range XPCS scanning microscopy. In this manner, we want to study the dynamics of Brownian and convective motion inside a microfluidic channel. Sequences of correlation images will give information about the anisotropy of the system in one sight.

2 Materials and methods

2.1 Materials

2.1.1 Lysozyme

Lysozyme from chicken egg white was purchased from Sigma-Aldrich (St. Louis, USA) as lyophilized powder. It was solved at room temperature in buffers at concentrations of 10 mg/ml for capillary X-ray measurements and 30 mg/ml for microfluidics measurements.

2.1.2 Chemicals and solutions

Guanidinium chloride (GdmCl), sodium acetate and glycine for the unfolding and refolding of lysozyme were purchased from Sigma-Aldrich (St. Louis, USA), and dissolved as explained in the experiment. SiO_2-particles for XPCS measurements were synthesized by Fabian Westermeier[36,98,99] and PPG-4000 purchased from Sigma-Aldrich (St. Louis, USA).

The self-emulsifying systems CrMTrans and TTMI for the measurements of nanoemulsions were prepared by Zdravka Misic[100,101] at the Institute of Pharma Technology of the University of Applied Sciences in Muttenz, Switzerland.

2.2 Soft lithography

Soft lithography is a technique to produce and replicate structures in elastomeric molds, usually polydimethylsiloxane (PDMS). Soft lithography evolved in the last 20 years into a powerful technique used in a variety of fields such as

microfluidics, photonics, electronics or biotechnology[102]. The elastic properties and the transparency to visible light of PDMS offer many advantages. The easy and straight-forward production, huge applicable size range from hundreds of micrometre down to 50 nm or the low pricing are only a few of them. In our case soft lithography was used for microfluidic devices, down to sizes of 10 µm.
Standard state-of-the-art microfluidic devices consist of PDMS and glass[103,104]. Both of them have a strong impact on X-ray measurements through absorption and scattering. Thus, different materials were used for the fabrication of microfluidic devices throughout this thesis. Each of it adapted to the needs of the appropriate experiment.
A typical process of device fabrication includes designing of a mask, preparation of a master and replica fabrication.

2.2.1 Mask design

The masks for the microfluidic devices were all designed using QCAD Professional version 2.2.2.0 by RibbonSoft GmbH and produced on polyester films by J.D. Photo-Tools, Oldham, UK. Masks of polyester films are cheaper than glass/chrome masks and can be produced in large sizes. However, they are limited to structures down to 10 µm though.

2.2.2 Master preparation

A master (see figure 2.1) is a usually hard, negative structure, which is used to produce replicas of softer materials. The masters were made of silicon wafers that were coated with photoresist. After exposure through a designed mask, the unexposed photoresist was washed away and a hard, durable negative structure of our design was left. The replica was usually produced using PDMS.

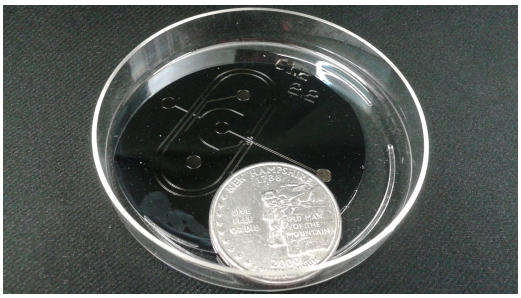

Figure 2.1: Image of a master: silicon wafer with photoresist-structure on top. An American quarter dollar is put next to for size comparison. The structure is a fast mixing device as used in section 4.

The procedure for the fabrication of a master is schematically shown in figure 2.2. First, a silicon wafer (Si-Mat, Kaufering, Germany) was heated to 200 °C for 10 minutes (hard baking). After cooling to room temperature, the appropriate SU-8 photoresist (Microchem, Newton, MA, USA) was spin-coated onto the wafer. The type of photoresist and the velocity of spinning determined the thickness of the coated layer, the choice was made according to the guideline of the producer. Another baking step followed, this time at 95 °C (soft baking). The wafer with photoresist was exposed through the polyester film mask for a few seconds to UV light (365 nm, 30 mW/cm^2) using a MJB4 mask aligner (SUSS MicroTec AG, Garching, Germany).

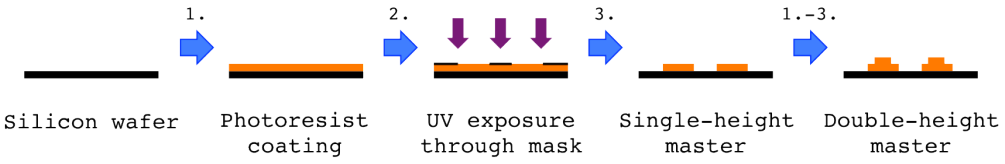

Figure 2.2: Fabrication of a soft lithography master. For double- or multi-height devices, steps 1.-3. were repeated before developing the structure.

Before exposure, contact wedge error compensation (WEC) was performed to make sure that the wafer was parallel to the mask and to adjust the pressure that was applied during exposure to press the mask on the silicon wafer. The

exposure was done in hard contact mode. Directly after exposure, the device was baked at 95 °C again for a few minutes (post exposure baking) followed by developing, i.e. the non-exposed resist was washed away with SU-8 developing solution (Microchem, Newton, MA, USA). All steps from soft baking to developing vary in time with the thickness of the photoresist layer. At the end, the final structure was hard baked at 200 °C for 10 minutes to ensure long durability of the device. For the different use of the microfluidic devices, different types of masters were developed and produced.

2.2.3 Standard PDMS/glass microfluidic devices

PDMS/glass devices (figure 2.3) are used for standard microscopy experiments. The thin glass slide enables the use of high magnification objectives with a short focus length. PDMS is transparent to the full spectrum of visible light and therefore ideal for bright field or fluorescence microscopy.

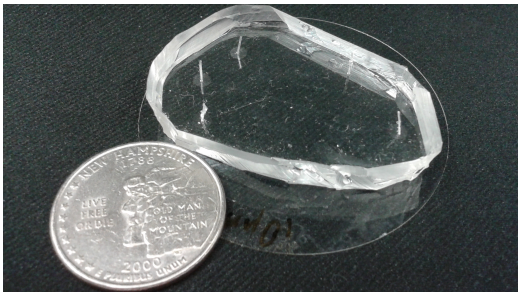

Figure 2.3: Image of a standard PDMS/glass device. An American quarter dollar is put next to for size comparison. The structure of the channel is a cross for standard hydrodynamic focus use.

The workflow to produce PDMS/glass devices is shown in figure 2.4. First, PDMS was thoroughly mixed 9:1 with crosslinker (Sylgard 184, Dow Corning GmbH, Wiesbaden, Germany) and mixed thoroughly. The PDMS was then given into a petri dish containing the produced master and degassed under vacuum until no bubbles

were visible anymore. It was then cured in an oven at 80 °C usually over night yet for at least 4 hours.

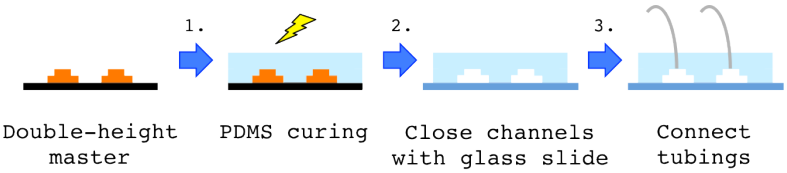

Figure 2.4: Fabrication of standard microfluidic devices using PDMS and a glass coverslide.

Using a disposable scalpel (B. Braun, PA, USA) the cured device was cut out around the structure, leaving a 1 - 2 mm margin between the cut and the outer structures on the master. The PDMS device was taken out of the petri dish very carefully in order to prevent any defects in the structure. In cases of a very delicate structure (such as high aspect ratios) few drops of isopropanol were added between PDMS and master to avoid sticking of the PDMS to the master. After removing the device from the master, holes were punched into the in- and outlets with a hole-puncher (Harris Unicore, diameter 0.5 mm). PDMS-device and a round glass-coverslide (VWR, PA, USA, 50 mm diameter, thickness no. 1) were cleaned with isopropanol and dried with nitrogen before being plasma cleaned in an oxygen plasma (Harrick Plasma, NY, USA) for 30 s at 2 mbar. The two parts were brought in contact and at the end PTFE-tubings (Adtech polymer engineering Ltd., Stroud, UK, 0.78 mm outer diameter) were connected to the in- and outlets.

2.2.4 Polystyrene/optical adhesive – devices

For the use of microfluidics combined with SAXS measurements, a special type of device had to be designed, in order to minimize the background scattering of the device and its material. This was achieved using Norland optical adhesive® 81 (NOA 81, Norland Products, Inc., Cranbury, USA) as main material to form the channel structures and 50 µm polystyrene foil (Goodfellow Cambridge Limited,

Huntingdon, UK) as covers on both sides to close the channels. Figure 2.5 shows an example of a polystyrene/NOA 81 device as used for XPCS measurements.

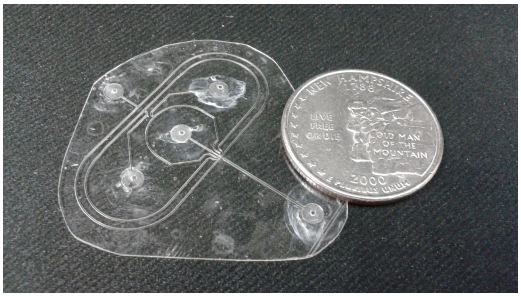

Figure 2.5: Image of a polystyrene/optical adhesive device. An American quarter dollar is put next to for size comparison. The structure is a fast mixing device as used in section 4.

2.2.4.1 Master fabrication

The master was made using SU-8 2100 photoresist, spun first at 500 rpm for 20 s and after ramping up the speed, at a rate of 3000 rpm for 60 s. After soft baking for 10 min the spinning procedure was repeated to double the total height of photoresist and the master was then soft baked for 20 min. It was exposed for 9 s at 36 mW/cm^2 which was followed by post exposure bake of 15 min. While being continually stirred, the structure was developed for about 5 min to wash off the unexposed resist.

2.2.4.2 PDMS replica production

PDMS and crosslinker (Sylgard 184, Dow Corning GmbH, Wiesbaden, Germany) were mixed in a 9:1 ratio and poured into a petri dish containing the prepared master. The PDMS was then degassed under vacuum and cured at 80 °C for a minimum of 4 hours. After curing, the PDMS was taken out of the petri dish, including the master which was then cut out using a disposable scalpel. First, all the PDMS on the back of the wafer was removed, resulting in having only the wafer side with the design on it

covered with PDMS. In a second step, all PDMS around the wafer was cut off in a slight angle, to the effect of leaving the edge of the wafer accessible to grab. The PDMS was then gently removed from the wafer. A round piece of plastic (e.g. cut from a 0.5 L PET bottle) was glued onto the PDMS replica, which now served as a master for another PDMS replica. To make sure that the two PDMS parts were still separable after curing, the PDMS master was plasma cleaned and left under a low-pressure atmosphere of (heptafluoropropyl)-trimethylsilane (Sigma-Aldrich, St. Louis, USA) for 40 min. This atmosphere was achieved by adding a drop of (heptafluoropropyl)-trimethylsilane close to the PDMS master in the desiccator. Afterwards, liquid PDMS was poured over it and it was again cured for at least 4 hours at 80 °C. The two pieces were separated and the second replica could now be used as a master for producing NOA 81 devices.

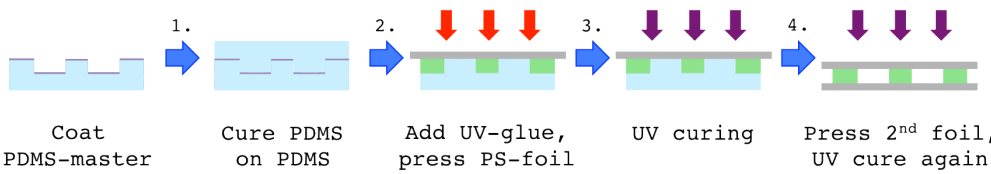

Figure 2.6: Fabrication of NOA/polystyrene-foil microfluidic devices used for XPCS. Alternatively, a negative silicon-master could be fabricated.

2.2.4.3 NOA 81/polystyrene devices

To produce NOA devices, a drop of NOA 81 is given on the PDMS master. Then a piece of polystyrene foil is put on top of the NOA 81 and by using a flat piece of glass the foil is pressed down on the PDMS. This was done manually until there were no bubbles visible anymore and no NOA 81 was left between the foil and the PDMS.

The half device was cured under a UV lamp (366 nm, 2 x 8 W from Camag, Muttenz, Switzerland) for about 30 s. To finalize the device, holes were made using a hole puncher (Harris Unicore, diameter 0.75 mm), a second polystyrene foil was put on the other side, gently pressed onto the whole device and everything was cured for 10 minutes.

2.2.5 Kapton®/PDMS – devices for fast mixing

The PDMS/NOA 81 devices described in the previous chapter showed beam damage when used at high intensities in synchrotron measurements (i.e. focussed beam). Additionally, when producing structure dimensions smaller than 20 µm, the channels made with NOA 81 tended to collapse after the first curing step. Therefore, another type of microfluidic devices for SAXS experiments was needed. Kapton® tape (5 cm, Swiss RepRap Tardo GmbH, Subingen, Switzerland) was used instead of polystyrene foil and NOA 81 was replaced by PDMS. Figure 2.7 shows a Kapton®/PDMS device, fabricated for fast mixing experiments.

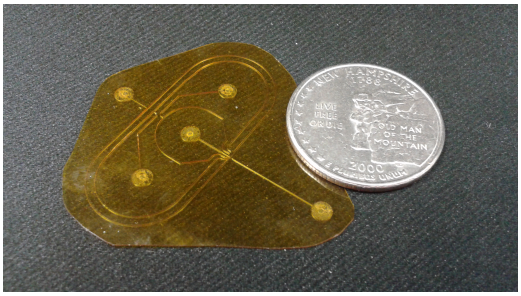

Figure 2.7: Image of a Kapton®/PDMS device. An American quarter dollar is put next to for size comparison. The structure is a fast mixing device as used in section 4.

2.2.5.1 Master fabrication

The devices for fast mixing include a double height structure. With other words the channel has different heights on different positions. To enable double height fabrication two different masks were needed; one for all structures on each of the two height steps. In comparison to a single height structure/master the coating, soft baking, exposure and post exposure baking steps were performed twice. In our case, SU-8 2100 photoresist was spun on the wafer for 10 s at 500 rpm and then for 30 s at 3500 rpm. Soft baking for 20 min, exposure for 5 s and post exposure baking for 10 min were performed. After the post exposure

baking, a second layer of SU-8 3025 photoresist was spun on the wafer, 10 s at 500 rpm and then 30 s at 4000 rpm, resulting in a height of 100 µm for the first plus 20 µm for the second step according to the supplier's protocol. Soft baking was done for 10 min and exposure for 3 s and post exposure baking for 3 min. After the WEC step before exposure, the contact lever was closed to bring wafer and mask in contact and then the gap lever was opened, to allow alignment of the mask to the structure already on the wafer. Developing for 5 - 10 min and hard baking for 10 min finalized the process.

In order to get a device with double height structures on top and bottom, two masters showing mirrored structures were produced. This enables the fabrication of two half devices that were aligned to get one single 3D device.

2.2.5.2 Fabrication of Kapton®/PDMS devices

The procedure to fabricate a Kapton®/PDMS device is shown in figure 2.8. The two masters were fixed on a tile to improve the handling of them during the fabrication. PDMS was mixed in a 9:1 ratio with crosslinker and degassed directly after mixing. Approximately 1 ml of degassed PDMS was then poured on each master and then covered by 5 cm wide Kapton® tape. To distribute the PDMS over the whole master, gentle pressure was manually applied on the tape. The ends of the tape were fixed onto the tile on both sides of the master and the remaining PDMS was pressed outwards using a rectangular piece of plexiglass until the structure of the master could be felt and the whole device was planar. The two device halves where then cured at 80 °C for at least 30 min.

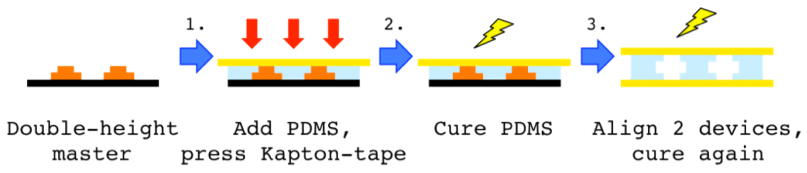

Figure 2.8: Fabrication of a Kapton®/PDMS device directly from silicon master.

After curing, the tapes were cautiously removed from the master and cut out around the actual channel. Holes were punched into one side using a 0.75 mm hole puncher. The two half devices were plasma cleaned for 30 s in an low pressure (2 mbar) oxygen plasma, aligned and brought into contact using a homebuilt setup with an *x*-*y*-*z*-stage from Thorlabs Inc., Newton, USA and a stereomicroscope (Olympus SZ61). The final device was cured in the oven at 80 °C for 4 hours or over night.

2.2.6 Adapted fast mixing devices for synchrotron

The use of synchrotron radiation focussed down to few hundred nanometre beams led to an interaction of the Kapton®/PDMS device with the X-rays. Consequently a new device was fabricated to avoid beam damage. The mixing and focussing part of the device was still produced as described in section 2.2.5, but the channel downstream was replaced by a 200 µm glass capillary (see figure 2.9).

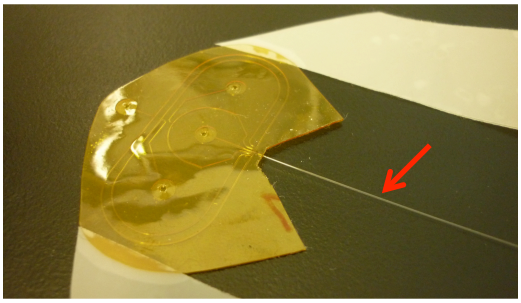

Figure 2.9: Image of an adapted Kapton®/PDMS device with connected capillary (red arrow). The size of the Kapton® part is the same as in figure 2.7.

First, a normal Kapton®/PDMS device as described in the previous section (2.2.5) was produced. After the final curing of the device in the oven, it was cut under the microscope about 300 - 500 µm downstream of the end of the mixing part. The cut was done with a sharp scalpel to avoid bruises or frazzles at the

newly created edge. A glass capillary with 200 µm outer diameter and a wall thickness of 10 µm (Hilgenberg, Malsberg, Germany) was put into the small part of the measuring channel. PDMS was prepared in a 9:1 ratio with crosslinker and left at room temperature for about half a day to partially cross-link. This was done to increase the viscosity of the PDMS in order to avoid the clogging of the whole channel when sealing the device-capillary connection. This connection was then sealed with PDMS by adding a small drop using a needle. Directly after adding the PDMS and ensuring that the channel was not blocked completely, the device was put into the oven at 80 °C and left for at least 1 hour to cure the connection. Figure 2.10 shows the steps of adding a capillary to a Kapton®/PDMS device.

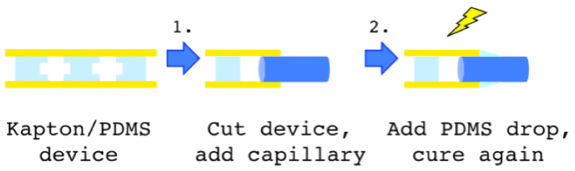

Figure 2.10: Fabrication of Kapton®/PDMS/capillary microfluidic devices for synchrotron use.

2.2.7 Fast mixing devices for in-house experiments

To adapt the microfluidic device for in-house experiments, the channels were fabricated with double the width of the Kapton®/PDMS device used at the synchrotron. The fabrication of the master was performed in the same way as described in section 2.2.5.1. Because with NOA 81 it is easier to align two half devices (compared to PDMS), the fast mixing devices were fabricated with polystyrene foil and NOA 81 (figure 2.11). Two half devices were done using a PDMS master as described in sections 2.2.4.2 and 2.2.4.3, with the difference of having a double height structure this time.

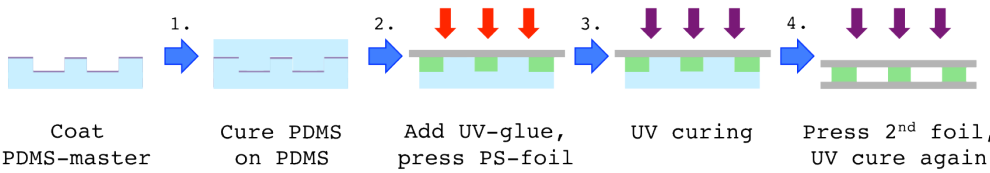

Figure 2.11: Fabrication of NOA/polystyrene-foil microfluidic devices. By adding two half-devices together, real 3D-structures can be formed.

The two half devices (one with wholes in the inlets) were aligned and put together using a homebuilt x-y-z-stage from Thorlabs Inc., Newton, USA and a stereomicroscope (Olympus SZ61). The completed device was UV cured again for 10 min.

2.2.8 Fabrication of PDMS/PDMS devices for liquid jet

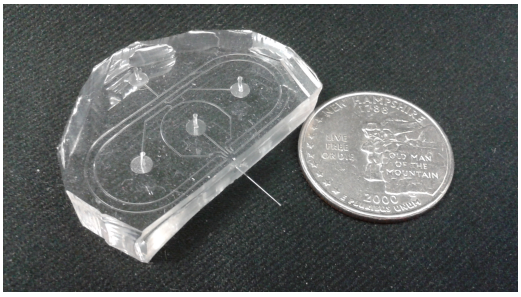

Figure 2.12: Image of a PDMS/PDMS device for liquid jet. An American quarter dollar is put next to for size comparison.

To show the potential of our fast mixing device, a liquid jet device was fabricated (figure 2.12). For easier handling, both half devices were formed from PDMS as described in section 2.2.3, however, without binding them to a glass slide. Instead, the two PDMS half devices were aligned and put together using the homebuilt setup already mentioned in sections 2.2.5.2 and 2.2.7. The final device was again cured in the oven at 80 °C for at least 4 hours. After curing, the PDMS/PDMS device was cut shortly behind the mixing part. A 200 µm wide glass capillary was sealed in a flame and cut at a point, where the inner diameter was

approximately 10 µm. The short piece of capillary was inserted into the PDMS device and a small drop of PDMS was added to seal the connection. Finally, the whole device was cured in the oven again for a few hours. Fabrication steps are shown in figure 2.13.

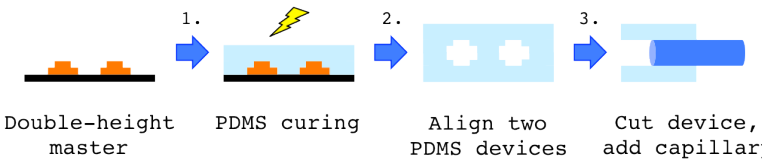

Figure 2.13: Fabrication of PDMS/PDMS device with glass capillary for liquid jet application.

2.3 Holder for SAXS microfluidic devices

A holder for the fabricated polystyrene/NOA and Kapton®/PDMS devices was fabricated by our mechanical workshop in the department.

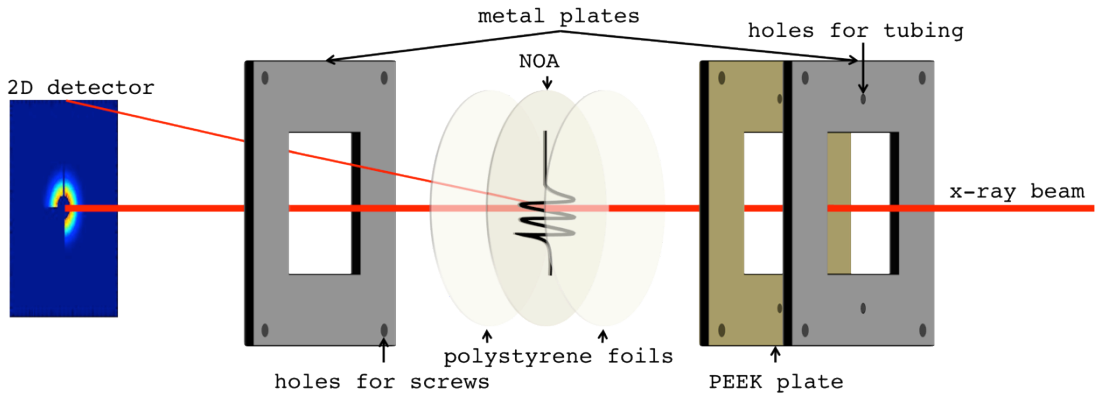

Figure 2.14: Setup for microfluidic SAXS-measurements using the home-built holder for microfluidic devices.

Figure 2.14 shows a schematic representation of the home built holder for microfluidic devices used in SAXS. Three plates, two made of stainless steel and one of PEEK, were screwed together with the device between the PEEK and one

of the steel plates. Holes in the PEEK and one of the steel plates (on the right site of the device on figure 2.15) allow the connection with PTFE-tubing. The diameter of the holes is 0.8 mm which is slightly bigger than the PDTFE-tubing (0.76 mm). Viton o-rings (Kubo Tech AG, Effretikon, Switzerland) are used to close the system and prevent it from leaking. A sketch of an inlet and the o-rings closing the system by the pressure applied to the screws can be seen in figure 2.15.

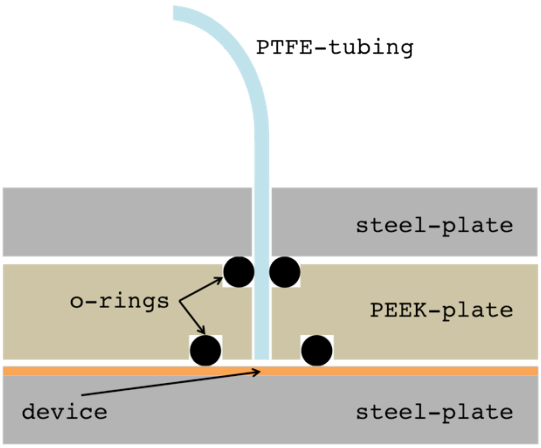

Figure 2.15: Inlet of home-built device holder. The viton o-rings close the system in order to prevent leaking.

2.4 In-house SAXS and WAXS setup

All in-house SAXS and WAXS measurements were performed at either of the two Bruker AXS NanoStar setups in our lab. The first setup includes an Incoatec Microfocus Source (IμS) using a Cu-K-α radiation with a wavelength of 1.54 Å and an intensity of up to 10^{10} photons/s/mm^2. The beam was aligned using Montel optics from Incoatec and collimated by a 3-pinhole system from Bruker AXS. The pinhole sizes used were 750 μm - 400 μm - 1000 μm for measurements in glass capillaries and 500 μm - 150 μm - 500 μm for measurements in microfluidic devices. The divergences of the beams for the two setups were

1.3 mrad and 0.72 mrad for the big and small pinholes, respectively. The sample chamber could be evacuated independently from the flight tubes. This was usually done during measurements of capillaries. Microfluidic experiments were done under atmospheric pressure. The use of removable flight tubes between sample and detector allowed us to change sample-to-detector distance and therefore also the measured scattering angles in a short time. As a detector a Bruker AXS Vantec-2000 with a 14 cm x 14 cm active area and a pixel size of 68 µm was used. This resulted in an angular resolution of the system of 0.95 mrad. The Vantec-2000 detector has a dynamic range of 10^9 (90 dB). The experiments were conducted at a Voltage of 45 kV and 650 µA (29.25 W) current on the filament. Most of the experiments were performed with this setup.

Only few measurements of gold-nanoparticles were performed on the second setup having a Turbo X-ray Source (TXS) rotating anode with Cu-K-α radiation with a wavelength of 1.54 Å and an intensity of roughly 10^{11} photons/s/mm^2 for our setup. Alignment by Göbel-mirrors and collimation by a 3-pinhole system similar to the first setup is used with pinhole diameters of 750 µm, 400 µm and 1000 µm. For this setup a Bruker AXS Hi-Star detector with a circular active area of 11.5 cm diameter and a 1024 x 1024 pixel sized frame was installed, the dynamic range of the Hi-Star detector is 10^6 (60 dB). All measurements were carried out at 50 kV and 108 mA and in complete vacuum. The angular resolution of this setup was 1.5 mrad.

The data was collected using the up to date Bruker AXS GADDS (Hi-Star detector) or SAXS (Vantec-2000 detector) software.

2.5 SAXS measurements in capillaries

For SAXS solution measurements 10 - 50 µl of sample volume were filled into a glass capillary (Hilgenberg, Malsberg, Germany). The capillary was sealed using a standard Bunsen-burner to ensure that the samples do not evaporate under

vacuum during the measurement. A capillary for each different solvent used was added to enable background subtraction later on.

The capillaries were first scanned using a piece of glassy carbon between sample holder and flight tube that scatters the beam homogenously up to relatively large angles. Consequently, an absorption image of the samples was taken and the exact position of the capillaries could be determined.

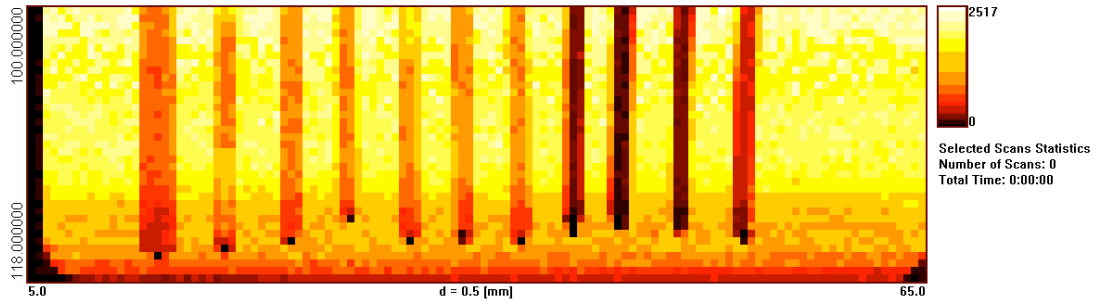

Figure 2.16: Sample of an absorption scan using the nanography tool from the SAXS software. Brighter spots correspond to higher intensity and hence to less absorption.

Figure 2.16 shows an example of an absorption scan. Due to the cylindrical shape of the glass capillaries, it is preferable to measure in their middle to avoid any scattering effects of the curvature. *X*- and *y*-coordinates correspond to the positions of the goniometer, while *d* is the step size between two pixels. The exact positions, the integrations times and the numbering of the samples were written down in a text file. The SAXS software from Bruker (version 4.1.4.2), which was used to take the scattering images, is able to read the text file with all the targets and measure one after the other, saving the results on the hard-drive. A 60 second absorption measurement was performed using the glassy carbon, before the scattering measurement of each sample capillary.

The obtained scattering images (see figure 2.17 for an example) were azimuthally averaged using the SAXS software's tool to integrate over all orientation angles (χ). The solvent was measured separately to allow its signal to be subtracted from the combined signal (sample + solvent) later on. The subtraction of the background was done in two different ways. Either by directly subtracting the scattering image of the background from the image of the sample

and then azimuthally averaging the final image or by averaging both images individually and subsequently subtracting the scattering curve of the background from the sample signal. In case of differences in absorption, the subtracted background had to be multiplied by the factor *S* which was calculated according to the ratio of the measured absorptions. *I* is the scattering intensity.

$$I(sample + solvent) - S \cdot I(solvent) = I(sample) \tag{2.1}$$

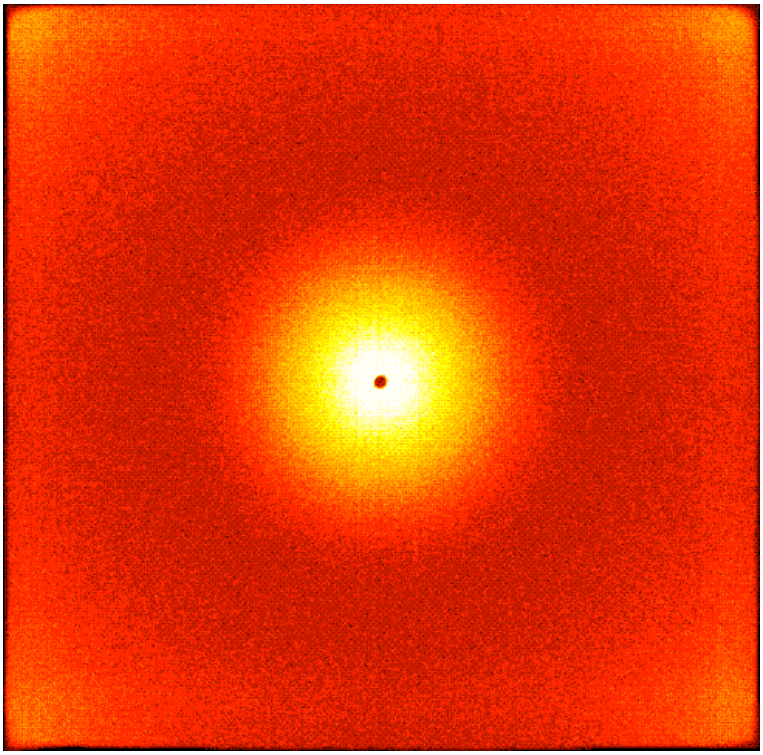

Figure 2.17: Scattering image of gold nanoparticles. The dark spot in the centre corresponds to the beamstop position. Intensity is decreasing towards the outside, relating to the particle's size.

2.5.1 Data analysis with NanoFit

Bruker directly supplies the software to analyse and fit integrated data. NanoFit (version 1.2) offers the possibility to fit scattering data with models of different standard shapes, such as spheres, cylinders, ellipsoids etc., additionally, different fitting routines can be used. For spherical samples, NanoFit was used to fit the

data and get information about the scattering objects. Radius and polydispersity were fitted using a Levenberg-Marquardt refinement [105,106].

The differential scattering cross-section $d\sigma/d\Omega$ for a monodisperse, spherically symmetric particle can be written as

$$\frac{d\sigma(q)}{d\Omega} = n\Delta\rho^2 V(R)^2 F(q,R) S(q), \tag{2.2}$$

where $d\Omega$ is the differential solid angle, n the number density of particles, $\Delta\rho$ the difference in scattering length density between the particles and the solvent, $V(R)$ the volume of the particles, $F(q)$ the particle form factor, $S(q)$ the structure factor and R the radius of the particles. For very dilute systems $S(q) = 0$, because correlation between particles can be neglected. For polydisperse samples the scattering cross-section becomes

$$\frac{d\sigma(q)}{d\Omega} = \Delta\rho^2 \int_0^\infty D(R) V(R)^2 F(q,R) dR \tag{2.3}$$

Here, $D(R)$ is the number size distribution, in our case we used a normalized Gaussian distribution[107] with R_{av} being the average radius of the measured particles and σ the standard deviation.

$$D(R) = e^{-\left(\frac{R_{av}-R}{\sigma}\right)^2} \tag{2.4}$$

We often measured spherical particles or objects that can best be described using a spherical form factor. The form factor of a homogeneous sphere was initially calculated by Lord Rayleigh and is given by equation 2.5.

$$F(q,R) = \frac{3\left[\sin(qR) - qR\cos(qR)\right]}{(qR)^3} \tag{2.5}$$

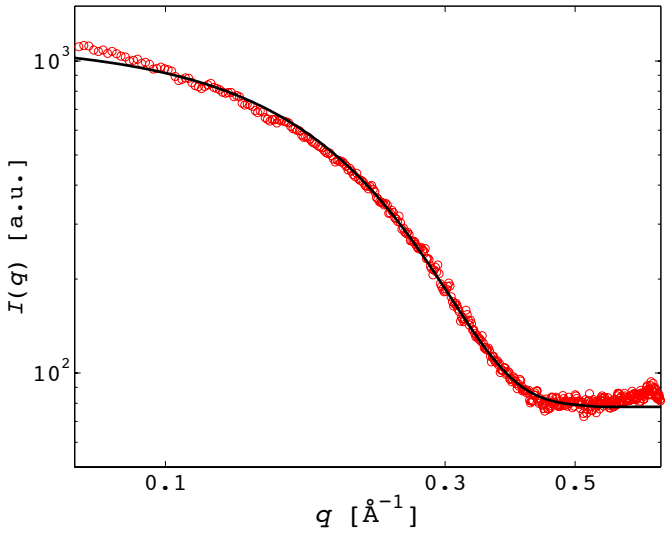

Figure 2.18: Example for scattering data of gold nanoparticles with a best-fit using equation 2.5, resulting in a radius of R = 8.7 Å ± 1.9 Å.

Figure 2.18 shows an example of scattering data that was fitted with the models described above (eq. 2.3, 2.4 and 2.5). The measured gold particles had a radius of R = 8.7 Å ± 1.9 Å.

2.5.2 Fit and PDDF using Primus and GNOM

As a second analysis method for spherical particles the Primus software[32], developed by Dmitri Svergun *et al.* at EMBL Hamburg, was used. The software was originally developed for biological samples such as proteins and enzymes but can also be used to analyse other samples with a homogenous shape distribution. This means that Primus is able to analyse different kinds of shapes, yet is not applying any polydispersity function during the analysis.

The data was imported in Primus software and plotted. The GNOM-function of the Primus software was then used to analyse the scattering intensities. First, the

data was fitted using a form factor for a sphere and thus giving results for the radius of the particle. The *q*-range for fitting could be varied in order to avoid bad intensity data to be considered (for instance the influence of the direct beam at very low *q*-values) The scattering intensity was fitted using equation 2.6 & 2.7[108].

$$I(s) = 4\pi \int_0^{D_{\max}} r^2 \gamma(r) \frac{\sin(sr)}{sr} dr \tag{2.6}$$

$$\gamma(r) = \left\langle \int \Delta\rho(u)\Delta\rho(u+r)dr \right\rangle \tag{2.7}$$

Here, $\gamma(r)$ is the spherically averaged autocorrelation function of the excess scattering density. For distances bigger than the maximal particle diameter, $\gamma(r)$ becomes zero. The variable *s* is another way of writing the momentum transfer *q* with $s = 2\pi/d$. Fitting of the data is important for further calculations, because due to incomplete background correction and possible concentration effects at high and low *q*-values respectively, the dataset can be incomplete (not starting at $q = 0$). Hence an inverse Fourier transform could not be applied directly on the scattering data. The inverse Fourier transform is needed to calculate the pair distance distribution function (PDDF) from the scattering intensity $I(s)$ using equation 2.8.

$$p(r) = \frac{r^2}{2\pi^2} \int_0^{\infty} s^2 I(s) \frac{\sin(sr)}{sr} dr \tag{2.8}$$

The PDDF $p(r)$ is another way to present the data obtained by a SAXS measurement. It contains the same information as the scattering curve but displays it in real space (nm), whereas the scattering intensity plot shows the data in reciprocal space (nm^{-1}) and therefore making it more intuitive to analyse the PDDF compared to the original scattering intensity. The PDDF gives the

probability $p(r)$ to find a pair of two elements with a distance r inside the scattering object. In this way, it provides information about the conformation of the sample.

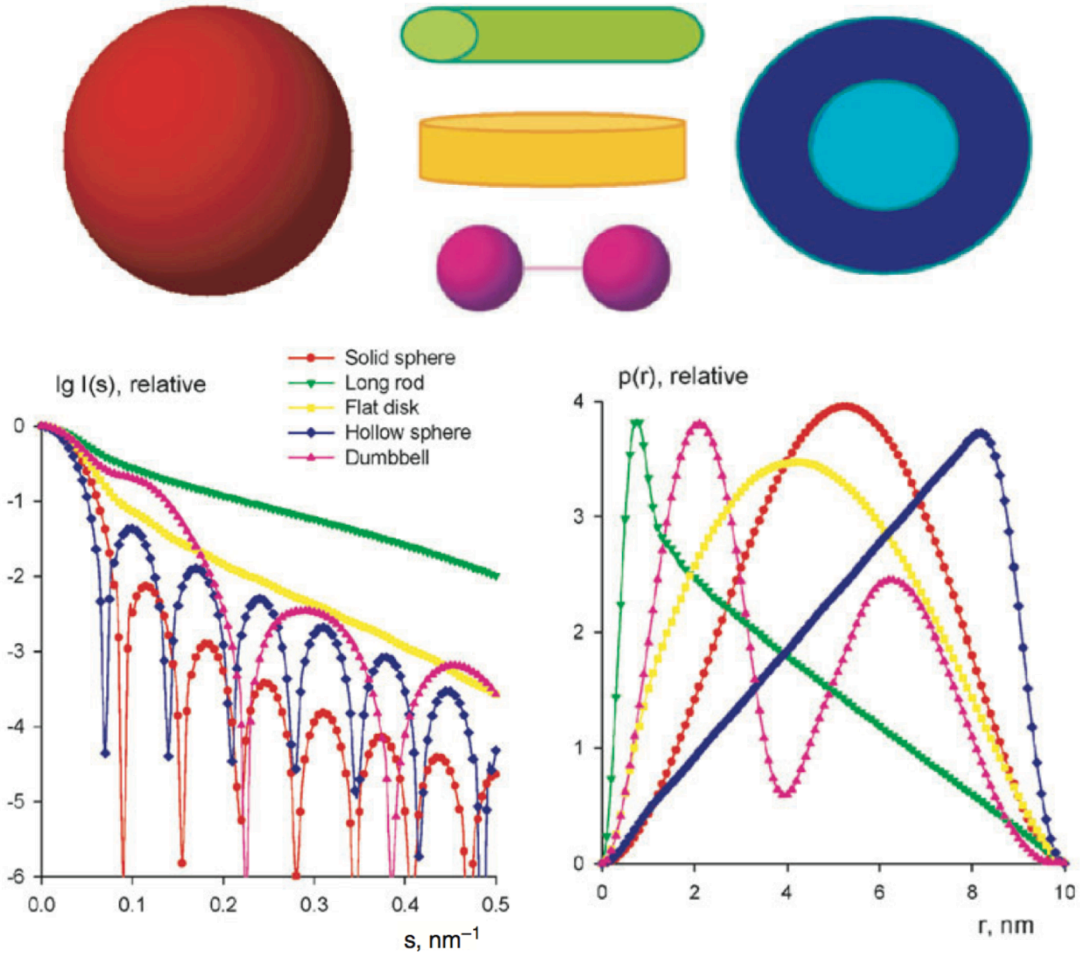

Figure 2.19: SAXS intensity plots ($I(s)$) and pair distance distribution functions ($p(r)$) of typical shapes. Taken and modified from [108].

Figure 2.19 shows intensity plots and PDDFs of different stereotypic shape styles. While the curve of the scattering intensity in reciprocal space is difficult to analyse directly, the PDDF gives a clear and intuitive idea about the most common distances in the measured particle[28]. Thus, it is possible to obtain information about the size and the shape of the measured sample.

For spherical particles for instance, the maximum of the bell-shaped PDDF corresponds to the radius of the particle (red dataset in figure 2.19). A hollow

sphere on the other hand has more scattering pairs with larger distances (blue dataset), therefore the maximum of the PDDF is shifted to higher *r*. The explicitness of the peak shift depends on the thickness of the wall.

2.6 Computational fluid dynamics simulations

The computational fluid dynamics simulations for the fast mixing device in section 4 were all done using COMSOL Multiphysics software version 4.3.1.161. The sequence type was a physics-controlled mesh with a coarse element size. All simulations were done for room temperature, laminar flow and no-slip boundary condition. Water was taken as fluid with different concentrations of diluted species (salt ions and protein). In a first step, the laminar flow inside the channel was simulated and in a second step the transport of the diluted species was calculated.

3 Characterization of self emulsifying systems

Not only hard hard-shelled particles such as spheres, rods or cylinders but also more complex systems like polymers or mixtures of immiscible fluids can be characterised with SAXS. Polymers have become a major part of chemical research, mainly connected with the term drug delivery in both, microscopic (nanocontainers) and macroscopic (capsules) applications. Commonly used gelatine capsules for drug delivery in the body show some major drawbacks such as their animal source, potentials cross-linking and drug migration[109]. Hence, there has been a great interest in finding substitutes for gelatine over recent years. Artificial polymer mixtures that spontaneously disperse into microemulsions with a large surface area when added to water proved to be promising alternatives for gelatine[100,110-112]: using such self emulsifying systems as artificial capsule material would solve the problems of gelatine usage. However, these systems have to be understood in detail before *in vivo* tests can be performed. Different mechanisms for the spontaneous emulsification are proposed and investigated[101,111,112]. Only in recent years, SAXS has been used to study the hydration phases of such self-emulsifying systems in order to get insights into the microstructural changes during emulsification[101,113-117].

This chapter deals with our study of two different self-emulsifying systems using SAXS to get an idea about their microstructures. CrMTrans and TTMI diluted in water were measured in glass capillaries at different concentrations. Information about domain size and periodicity were obtained by applying a Landau-theory based model developed by Teubner and Strey[118].

3.1 Microemulsions

Microemulsions are defined as thermodynamically stable mixtures of water, oil and amphiphiles[119-121]. Macroscopically, they appear as homogeneous phase, but microscopically, water and oil rich domains are separated by a layer of amphiphiles[118]. To understand the arrangement and the microstructures of microemulsions, different experimental investigations were performed. Thereof NMR self diffusion and scattering techniques (DLS, SAXS) were the most promising ones[118]. First SAXS measurements showed a single broad peak and a characteristic q^{-4} dependence at large q-values[122]. The q^{-4} dependence can be assigned to monolayers of amphiphile molecules at a well-defined internal interface[28,122-124]. The broad peak found in a variety of microemulsion systems was first explained by the simple approach, that microemulsions were conceived as a collection of droplets[118]. Like this, the peak could be explained as the first maximum of the structure factor, resulting in a typical scattering ring for simple fluids[125,126]. This explanation was later corrected, as the single scattering peak was also found in water/oil mixtures which were known to have a bicontinuous structure[118,122-124]. The features of microemulsion phase behaviour could be explained by the thermodynamic description of the global phase behaviour of multicomponent mixtures[127,128]. The phenomenological Landau theory explains the three phase monohedron (i.e. a tricritical point in ternary and quaternary fluid mixtures, where three phases simultaneously become identical[127]) and phase sequences observed in optimum microemulsion formulations (i.e. microemulsions containing equal volumes of oil and water)[129-133]. When gradient terms were introduced into the Landau model, fluctuation theory predicted the occurrence of a single broad peak together with a q^{-4} dependence[118].

3.2 The Landau model and its application to microemulsions

The general Landau model is a treatment of phase transitions and critical points. It is based on the idea, that coexistence curves at critical points can be described as mathematical functions with two minima at low temperatures, merging into a single minimum at higher temperatures[134]. This function can be specified by expressing the Landau free energy F as a polynomial function of an order parameter ψ[135] of the free energy density f[118]. An order parameter describes the degree of order across the border in a phase transition system[136]. For a liquid/gas transition for instance, the order parameter is the difference in densities.

$$F = \int f\left(\psi, \nabla\psi, \Delta\psi\right) d^3r \tag{3.1}$$

$$f = a_0 + a_1\psi + a_2\psi^2 + a_3\psi^3 + \ldots + c_1\left(\nabla\psi\right)^2 + c_2\left(\Delta\psi\right)^2 + \ldots \tag{3.2}$$

The coefficients a_i and c_i depend on the physical problem at hand. For the simplest problems, the free energy function is expected to be symmetrical around $\psi = 0$, hence, all terms involving odd powers are eliminated[134]. Here, three examples of coefficients for specific physical problems are listed.

$a_i \equiv 0$ for $i > 4$; $c_i \equiv 0$. This case represents the application of the classical theory of Landau to binary systems of two partially miscible liquids. It describes the vicinity of ordinary critical points qualitatively correct[118].

$a_i \equiv 0$ for $i > 6$; $c_i \equiv 0$ represents the phenomenological theory of tricritical points for multicomponent systems[127]. Microemulsions are often near-critical (i.e. close to a critical point, where two phases become similar)[131-133].

$a_i \equiv 0$ except $a_2 > 0$; $c_i \equiv 0$ except $c_1 < 0$, $c_2 > 0$. These are the coefficients that Teubner and Strey claim to be sufficient to explain the typical features of scattering curves of microemulsions, as explained in the following paragraph[118].

The X-ray scattering of an isotropic liquid is strongly linked to the fluctuations of the order parameter ψ, which in our case depends on the oil-to-water ratio. As for small fluctuations in a homogeneous isotropic phase higher orders than second can be neglected, only $a_2 > 0$ is kept in equation (3.2). According to the classical van der Waals-Cahn-Hilliard theory[137], surface tension σ is proportional to $\sqrt{c_1}$. The tendency in microemulsions is to create interfaces (i.e. domain walls) spontaneously, which corresponds to a negative "microscopic surface tension". Hence, $c_1 < 0$ seems to be an essential ingredient of microemulsions[118]. One higher order gradient term is required to stabilize the system ($c_2 > 0$), this results in the simples possible F for microemulsions[118]:

$$F = \int \left[a_2 \psi^2 + c_1 \left(\nabla \psi \right)^2 + c_2 \left(\Delta \psi \right)^2 \right] d^3 r \,. \tag{3.3}$$

The stability condition is given by $4 a_2 c_2 - c_1^2 > 0$ [118].

For scattering intensity distribution $I(q)$ we get the relation:

$$I(q) \sim \frac{1}{a_2 + c_1 q^2 + c_2 q^4} \,. \tag{3.4}$$

The negative c_1 results in one single broad peak and the positive c_2 leads to the q^{-4} decay towards high q-values, as it was found in experiments. There are two featuring length scales known about microemulsions, one being the alternating arrangement of oil and water domains and the other the loss of long-range order. Thus, for microemulsion two length scales are needed to describe the system[118]. This stands in contrast to an ordinary Ornstein-Zernike behaviour (where $c_2 \equiv 0$) with only one single length scale[135,138]. Thus, the domain size d (periodicity) and the correlation length ξ were defined to describe a microemulsion system[118].

$$d = 2\pi\left[\frac{1}{2}\left(\frac{a_2}{c_2}\right)^{1/2} - \frac{1}{4}\frac{c_1}{c_2}\right]^{-1/2} \tag{3.5}$$

$$\xi = \left[\frac{1}{2}\left(\frac{a_2}{c_2}\right)^{1/2} + \frac{1}{4}\frac{c_1}{c_2}\right]^{-1/2} \tag{3.6}$$

In this chapter, the SAXS data measured from CrMTrans and TTMI self-emulsifying systems were fitted using equation (3.4). The length scales *d* and ξ were calculated to estimate the microscopic structure of the two different systems.

3.3 CrMTrans and TTMI

The two investigated systems where CrMTrans and TTMI; the exact composition can be seen in tables 3.1 and 3.2. They were prepared by Zdravka Misic from the Institute of Pharma Technology of the University of Applied Sciences in Muttenz, Switzerland. In order to study the dependence of the periodicity *d* and the correlation length ξ on the water-to-oil ratio, hydration concentrations from 10 - 90 % were prepared[101].

CrMTrans	Generic name	Function	%
Cremophor RH40	Macrogolglycerol hydroxystearate polyoxyl 40 hydrogenated castor oil	Non-ionic solubilizer, surfactant	60
Miglyol 812	Caprylic/Cypric Triglyceride	oil	15
Transcutol HP	Highly purified diethylene glycol monoethyl ether EP/NF	solvent	25

Table 3.1: Composition of CrMTrans.

TTMI	Generic name	Function	%
Tween 80	Polysorbate 80, PEG (80) sorbitan monooleate	surfactant	45
Miglyol 812	Caprylic/Cypric Triglyceride	oil	15
Transcutol HP	Highly purified diethylene glycol monoethyl ether EP/NF	solvent	20
Imwitor 742	Caprylic/Capric Glyceride	co-surfactant	20

Table 3.2: Composition of TTMI.

Figure 3.1 shows the viscosities depending on the hydration concentrations. A single maximum can be observed for both formulations.

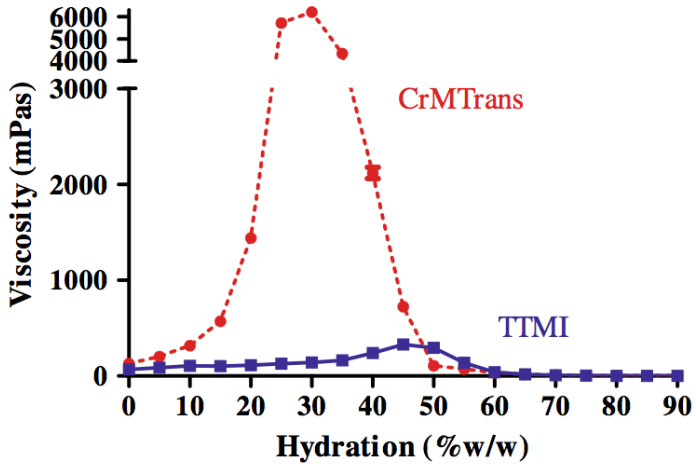

Figure 3.1: Viscosity of CrMTrans and TTMI. Taken from [101].

3.4 SAXS measurements and data treatment

3.4.1 Measurement and fitting

The experimental procedure for both, CrMTrans and TTMI was the same, hydration concentrations from 10% up to 90% were measured in glass

capillaries under vacuum at room temperature. The corrected SAXS intensities were fitted using the Teuber-Strey model (equation 3.4) for microemulsions.
Using equations (3.5) and (3.6) the domain size d and the correlation length ξ were calculated. Figuratively, these two length scales resemble the distance between the domains (i.e. between two water domains or oil domains) and the distance over which these structures are aligned (i.e. they have the same orientation and dimensions). The ratio d/ξ is a measure of the polydispersity of the domain size, the smaller the ratio, the smaller the polydispersity[139,140].

3.4.2 Results and discussion

Figures 3.2 and 3.3 show the scattering curves of five selected measured hydration concentrations of CrMTrans and TTMI. The curves are shifted by a factor of 10 each in order to get a better overview. The fits of the curves using equation 3.4 are shown as continuous lines. The domain size d is directly linked to the position of the peak, while the width of the peak can give a first idea about the correlation length ξ in the system.

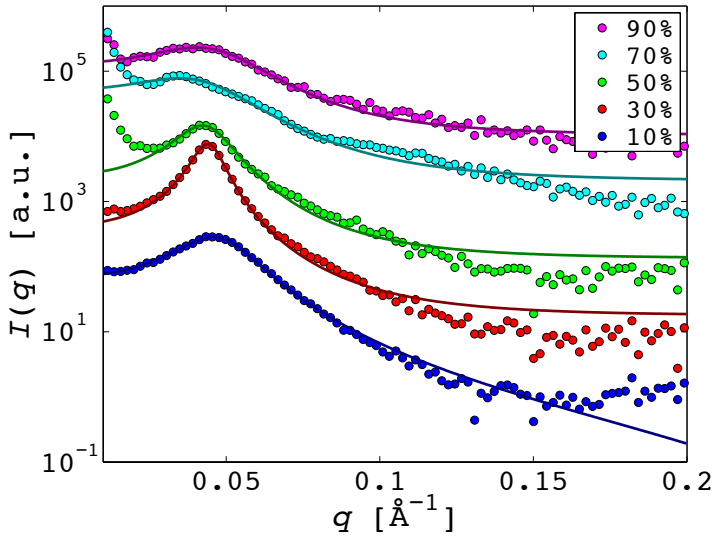

Figure 3.2: Scattering curves of CrMTrans in five selected hydration concentrations. Continuous lines show the fits using the Teubner-Strey model.

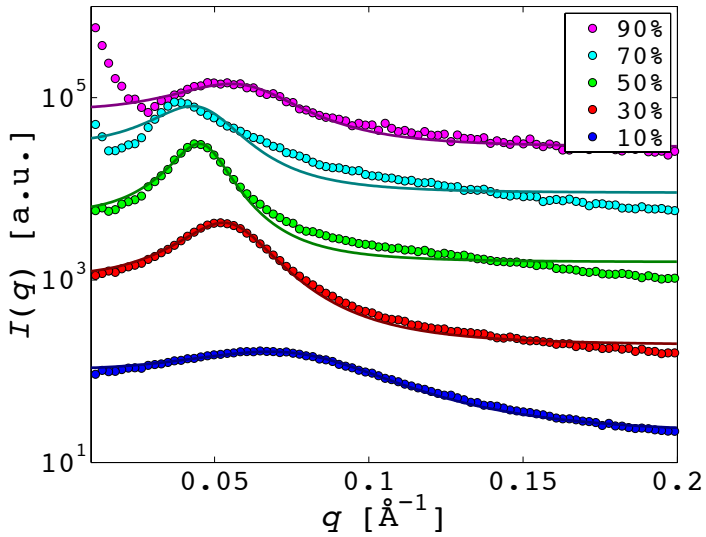

Figure 3.3: Scattering intensities of TTMI in five selected hydration concentrations. Continuous lines show the fits using the Teubner-Strey model.

In both figures we see a prominent peak for all shown hydration concentrations. A general tendency towards smaller q-values of the peak position can be observed with increasing hydration concentration. The fits in both figures show a very good congruency with the scattering data for low hydration concentrations. At higher water content however, the difference between fit and data becomes bigger, possibly due to the additional scattering signal at very small angles, which starts at higher hydration concentrations. Additionally, the peaks at hydration levels above 60% for CrMTrans and above 70% for TTMI become less prominent and their position shifts back to higher q-values.

These two changes suggest that at these concentrations a bigger structure starts forming, which could be a vesicle or a micelle and interferes with the microemulsion. We therefore conclude, that a two phase system forms at higher hydration concentrations: i.e. a coexistence of the microemulsion with a second species, larger than the typical domain size of the emulsion.

For both systems, the domain sizes *d* were calculated and plotted in figure 3.4. They show an evolution towards larger *d* with increasing hydration levels and two maxima, one around the concentration with the highest measured viscosity (shaded areas) and a second, higher one at higher hydration concentration.

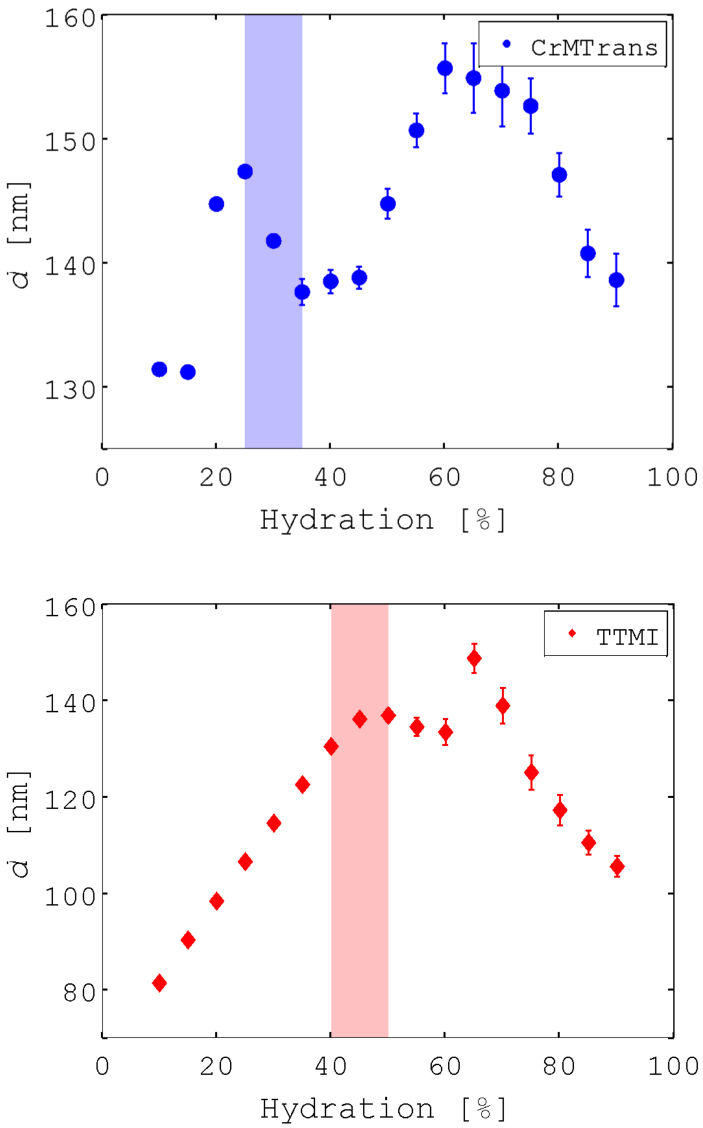

Figure 3.4: Domain sizes of CrMTrans and TTMI at increasing hydration concentrations. The shaded areas indicate the concentration range with the highest measured viscosity (cf. figure 3.1). Two local maxima can be observed in both cases, of which one lays in the range of the shaded area.

The increasing domain sizes suggest a swelling of the domains with addition of water up to a certain concentration. The domain sizes start decreasing exactly at the moment where a second scattering signal appears (i.e. a second phase is formed) in the SAXS measurements. This indicates that the newly formed species is able to absorb more water. Only after further expanding the hydration concentration, the domain sizes increase a second time.

In both systems, the domain sizes decrease after a certain critical hydration concentration (60 % for CrMTrans and 65 % for TTMI). This leads to the assumption, that after a certain hydration level, the microemulsion character of the solution starts to disappear, and the second phase that started forming at lower concentration becomes dominant.

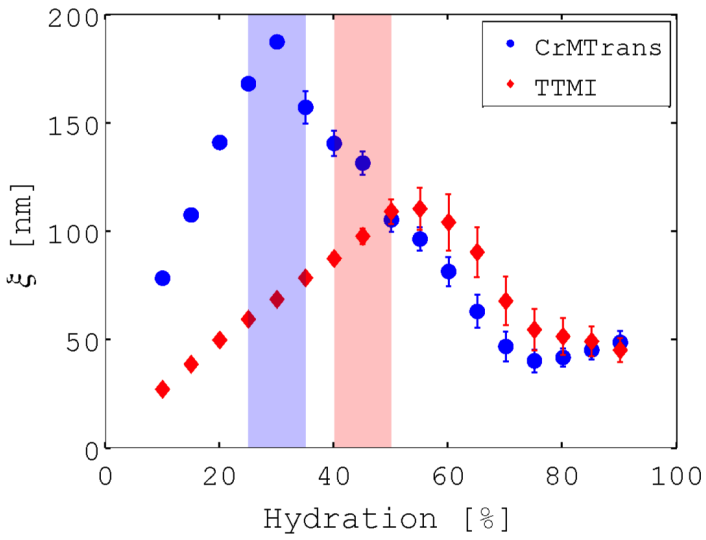

Figure 3.5: Correlation lengths of CrMTrans and TTMI at increasing hydration concentrations. The shaded areas indicate the maximal viscosity measured (cf. figure 3.1).

Figure 3.5 shows a plot of the correlation length ξ of both self-emulsifying systems. The shaded area indicates the water concentrations where a maximal viscosity was measured (cf. figure 3.1). ξ is constantly increasing with higher hydration up to a single maximum and then decreasing with further increase in hydration concentration. Interestingly, the maximal correlation length ξ, the

maximal viscosity and the arising of the additional species are in the same range of hydration concentration. This indicates that the second phase disrupts the order in the system and consequently the viscosity decreases. Unlike the domain sizes, the correlation lengths (and also the viscosities) do not increase again with further increasing hydration concentrations but rather reach a plateau around 75%. This can be explained by the fact that domains and the second phase are further swelling with increasing water concentrations, but remain coexisting. Thus the order in the system is not increasing again.

We also calculated the ratio d/ξ, which is dimensionless and proportional to the polydispersity in the sample. In figure 3.6, d/ξ is plotted for CrMTrans and TTMI.

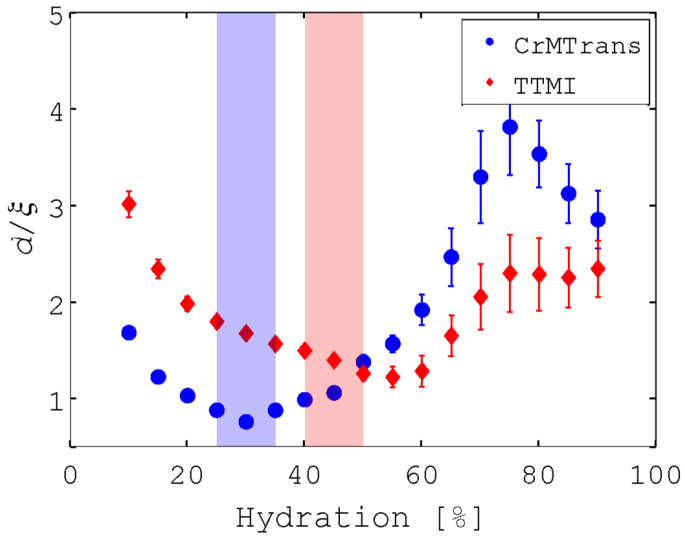

Figure 3.6: d/ξ plotted for both systems over all hydration concentrations. Shaded areas indicate the maximal viscosity measured (cf. figure 3.1). d/ξ is a measure for the polydispersity in the system, the lower the ratio, the smaller the polydispersity[139].

For both systems, d/ξ shows a minimum around the hydration where ξ and the viscosity are maximal and a maximum at 75%. Thus we observe a decreasing polydispersity with increasing correlation length and vice versa. A coexistence of two phases (microemulsion and the second structure at very small scattering angles, i.e. micelles or vesicles) can explain the sudden decrease in correlation

length as well as the increase in polydispersity. At very high hydrations, the ratio remains at least constant (or even decreases), which can be explained by the fact that the microemulsion phase is disappearing and thus only the second phase (larger structures) remains.

3.5 Conclusion

In this experiment, we successfully measured the dependence of the structure of two self-emulsifying systems on the hydration concentration. The Teubner-Strey model derived from the phenomenological Landau theory allowed the calculation of the domain sizes and correlation lengths in the systems.

Upon increase of hydration, the mixtures seem to undergo a transition from a one-phase (microemulsion) to a two-phase (microemulsion and micelles/vesicles) system, which highly affects the two measured length scales as well as the polydispersity. When comparing the behaviour of these parameters with the viscosity of the systems, we can conclude, that the microscopic changes directly affect macroscopic characteristics of these two materials.

Overall, the two measured systems CrMTrans and TTMI show a very similar behaviour. The main difference consists in the hydration concentrations at which the structural changes occur. This might be interesting for further experiments in drug delivery, as these self-emulsifying systems seem to be tuneable according to the needs of their application (i.e. different drugs, specific locations in the body etc.).

4 Fast-mixing microfluidic device for measuring reaction dynamics

4.1 Introduction

Microfluidics has become a widely used tool to investigate chemical and biological reactions (cf. section 1.2). As a reaction typically involves mixing of two or more reactants, fast and complete mixing is a critical parameter. Different mechanisms of decreasing mixing time and increasing efficiency in microfluidics have been introduced in section 1. Parallel and serial lamination and chaotic advection are principles to decrease the mixing time in a microfluidic device. The drawbacks of existing parallel lamination mixers include the large velocity dispersion due to no-slip boundary conditions across the channel that limits temporal resolution. One way to overcome the velocity dispersion in *y*-direction (*x* being the axis along the channel) is hydrodynamic focussing (c.f. section 1.2.1.1). Focussing the sample stream in *y*-direction concomitantly decreases the diffusion time and the velocity dispersion. However, velocity dispersion only decreases in *y*-direction and not in *z*-direction. Moreover, the narrow focussing yields a small sample volume that is measured by SAXS.

In this chapter, we present a device that affords fast mixing, low velocity dispersion in *y*- and *z*-direction and feasibility for in-house SAXS experiments. The latter requires wider channels (300 µm), which provide more material in the measured volume (i.e., the X-ray beam).

4.2 The device

The main goal was to create a fast mixing device for in-house and synchrotron SAXS measurements. The beam size of the Bruker Nanostar on site can be narrowed down to 150 – 200 µm, meaning that the width of the channel in the microdevice should be in a similar range. Moreover, the section of the channel where reactants are mixed and the section where the measurement occurs have significantly different dimensions. While the width of the latter was limited by the beam size of the in-house setup, the mixing section was designed as narrow as standard device fabrication methods would allow for (sections 2.2.4 and 2.2.5).

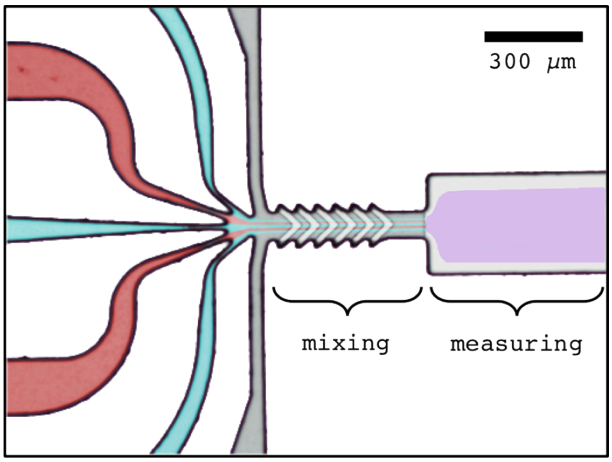

Figure 4.1: Fast mixing device with 5 inlets (coloured) for solutions. Inlet (grey) is for hydrodynamic focussing. Narrow channel section facilitates rapid mixing, while the dimensions of the wider section (purple) fit the in-house beam size (i.e., the full beam is inside the channel without hitting edges).

Figure 4.1 shows an artificially coloured microscopy image of the fast-mixing device where different solutions are represented by different colours. The two main parts of the device are a wide channel for measuring and a combination of narrow channel and additional structures for improved mixing by microfluidics.

The channel section for measuring has a width of 300 µm. This width concurs with using an X-ray beam of 200 µm and at the same time is adequate for avoiding background signals from edges or device material (i.e., NOA 81 or PDMS). The height of the channel is 220 µm. The cross sectional area of the channel for measuring (A) and the diameter of the X-ray beam (d_{beam}) define the temporal resolution of the setup (equation 4.1). Q is the flow rate.

$$t_{res} = \frac{d_{beam} \cdot A}{Q} \tag{4.1}$$

Structures related to mixing have to meet several demands. The reactants have to be fast and efficiently mixed. At the same time, the dead time (i.e., the time elapsed up to the first measuring point) has to be minimized (equation 4.2). Dead time thus depends on the length (l_{m}) and the cross sectional area (A_{m}) of the mixing section of the channel, which both should be as small as possible

$$t_{dead} = \frac{l_m \cdot A_m}{Q} \tag{4.2}$$

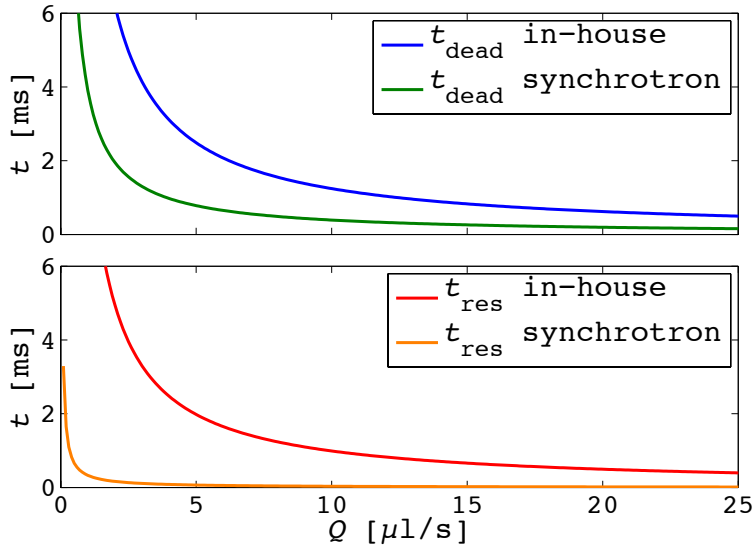

Figure 4.2: Calculated dead times and temporal resolutions of in-house setup and typical synchrotron setup.

In figure 4.2, calculations of dead times and temporal resolutions are shown in dependence of the flow rate for the channel dimensions for in-house and synchrotron measurements. Beam sizes used for calculations are 200 µm for in-house and 10 µm for synchrotron sources, while channel widths are 300 µm/80 µm (measuring channel/mixing channel) for in-house and 150 µm/40 µm for synchrotron devices. The much lower width of the mixing channel compared to the measuring channel does not only reduce the dead time of the device but also decreases the diffusion paths for the reactants in order to mix. Moreover, the respective width of the measuring channel is wide enough to ensure that only sample and no device material is measured in the sampled volume. A wider measuring channel allows us to have more sample material in the X-ray beam. This is crucial especially when investigating weakly scattering biomaterials with in-house SAXS setups that have a 10^6 times lower X-ray intensity compared to synchrotrons. Two other features further decrease the diffusion path. First, we created a parallel lamination by having five inlet channels, two (red in figure 4.1) for one reactant (e.g., a protein solution with folded or unfolded protein) and three (cyan in figure 4.1) for the second reactant (e.g., protein unfolding or refolding buffer) thus reducing the diffusion path (x) by a factor of 2.5 compared to two parallel streams of a conventional T-mixer. A reduction of x by a factor of 2.5 leads to a decrease of the diffusion time (t_D) by a factor of 6.25 as t_D depends on the square of the diffusion path (equation 4.3).

$$t_D = \frac{\langle x \rangle^2}{2D}, \tag{4.3}$$

where D is the diffusion constant.

However, the time needed to flow through the mixing section (t), depends linearly on the width of the channel (equation 4.4) and is thus not reduced in the same manner as t_D in equation 4.3.

$$t = \frac{x \cdot h \cdot l}{Q}, \tag{4.4}$$

where h is the channel height, l the mixing channel length and Q the flow rate. In other words, a narrow mixing channel leads to a better mixing over a given channel length than a wide one.

The diffusion path and therefore the mixing time, is further decreased by a hydrodynamic focus (grey channel in figure 4.1). The extent to which the sample should be hydrodynamically focussed has to be chosen carefully, since a too narrow sample stream leads to an excessive loss of sample volume in the X-ray beam. Another effect of the focussing is the decrease of velocity distribution across the sample stream as it is pushed towards the channel centre which improves temporal resolution of the measurements.

Taken together, by optimizing the dimensions of the measuring channel the diffusion path could be significantly decreased compared to a simple T-mixer.

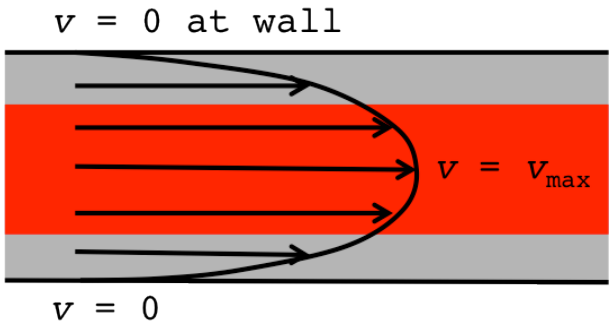

Figure 4.3: The stream of sample fluid and buffer (red) is hydrodynamically focussed in *y*-direction. *v* is the flow velocity. A similar situation results in *z*-direction through focussing by specific flow-defining geometries, as discussed later.

Figure 4.3 shows a sketch of the flow situation in the channel section for measurements (top view). Pushing the sample stream (red) away from the channel walls towards the centre leads to a decrease in velocity dispersion indicating that the measured sample has a more uniform velocity. We can nicely

depict this by calculating the average velocity inside the sample stream for different channel widths in comparison to the full channel (figure 4.4).

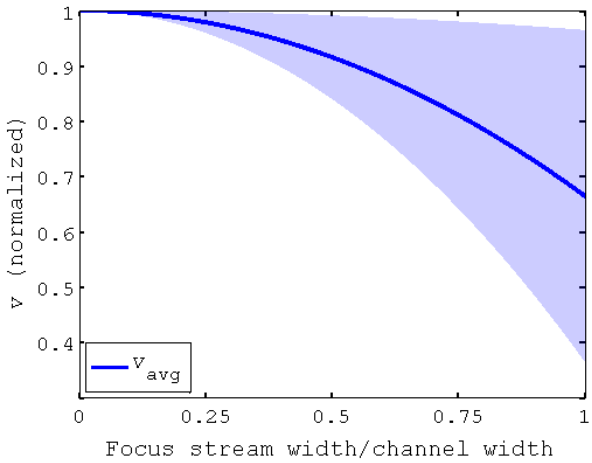

Figure 4.4: Average velocity and its standard deviation inside the focussed sample stream.

As illustrated in figure 4.4, the standard deviation (light blue area) of the mean velocity is much larger for less focussed streams compared to a sample stream that only takes half or even one fourth of the full channel width.

So far, we have developed a fast mixing device with very low velocity dispersion in *y*-direction. However, no-slip boundary conditions also lead to a wide velocity difference along the *z*-axis which eventually decreases the temporal resolution of the device. Several approaches are possible for focussing the sample stream also in *z*-direction, for example, a top and/or bottom inlet (hydrodynamic focus in *z*) or specific flow-defining channel geometries (chevron-like structures on top and bottom of the channel)[65].

Here, we added six flow-defining chevron-like structures at the top and bottom of the mixing channel. The chevrons are 20 µm wide, and they are 10 µm higher than the rest of the channel. The angled structure pointing in flow direction leads to the addition of fluid from the side stream at the top and bottom of the sample stream. Figure 4.5 shows a sketch of the concept of the flow-defining chevrons.

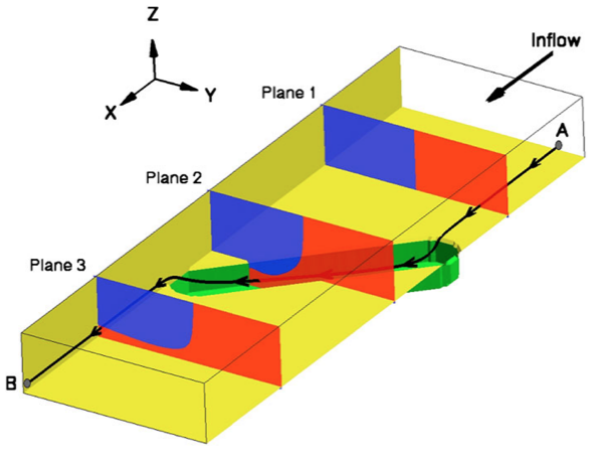

Figure 4.5 The concept of chevrons. The diagonal direction of the lower (or higher) structure leads to the addition of side-fluid (red) on the bottom (or top) of the sample fluid (blue). Taken from [65].

By integrating chevron structures, we obtain a sample stream that is focused in both, *y*- and *z*-direction (cf. figure 4.3). As a result, the velocity dispersion in the sample is very narrow, allowing for the high temporal resolution required for fast dynamics experiments.

4.2.1 Simulations of protein mixing

We performed computational fluid dynamics (CFD) simulations of a protein mixing experiment using COMSOL Multiphysics software. Accordingly, diffusion constants were chosen at 10^{-9} m^2/s in the buffer channels (blue inlets in figure 4.1) and the focussing channel (resembling salt ions or other small molecules) and $5 \cdot 10^{-11}$ m^2/s (typical for a protein) for the sample inlet (red in figure 4.1). The dimensions of the device were assumed to be 60 µm x 50 µm (width x height) for the mixing section with chevrons of 20 µm width and an overall height of 70 µm (i.e., additional 10 µm on the top and bottom compared to the mixing channel), and 240 µm x 70 µm for the measuring channel. The flow rates were set at 60 mm/s for the five mixing inlets, and 300 mm/s for the

focussing inlet. The resulting total flow speed is 1.35 µl/s. This leads to a dead time of t_{dead} = 1 ms. Protein concentration at the inlet was 10 µM.

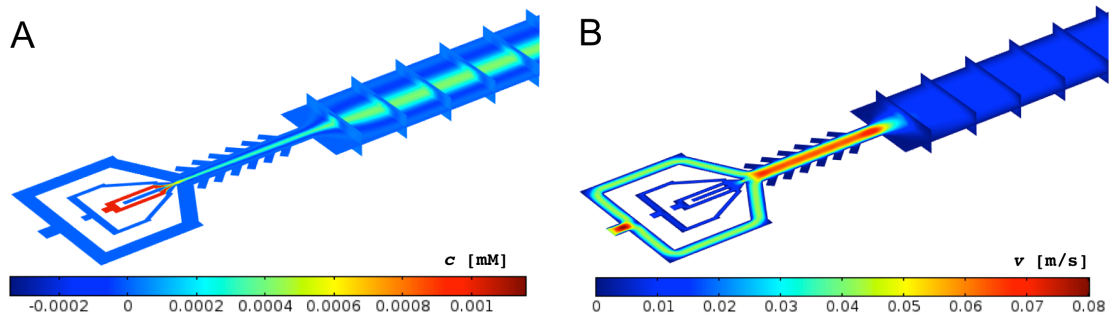

Figure 4.6: CFD simulations of protein concentration (A) and flow velocity (B) in the mixing device. Unit for concentration is mM and for velocity is m/s. General conditions were 293 K, 0.06 m/s flow speed for the five sample inlets, 0.3 m/s flow speed for the focussing inlet and diffusion constants of 10^{-9} m²/s for all blue coloured inlets in (A) and $5 \cdot 10^{-11}$ m²/s for the protein solution (red).

Figure 4.6 shows the simulations of the protein concentration (A) and flow velocity (B) in the fast-mixing device with the parameters indicated above. The simulation of the protein concentration (fig. 4.6 A) reveals that the sample stream (cyan) has a homogenous concentration along the measuring channel; it is approximately 4 µM and thus two fifth of the original protein concentration at the inlet. From the simulation we conclude that 1 ms of mixing time is sufficient to completely mix the buffer solutions with the protein solution. Additionally, the small diffusion coefficient of the protein ensures that the protein itself does not significantly diffuse towards the channel walls. Because protein concentration and the velocity dispersion in the sample stream stay constant along the channel (i.e., along the reaction time axis), we can measure and compare data from different points along the device.

Different sectional views of the protein concentration and the flow velocity in the channel are depicted in figure 4.7. Panel A represents a longitudinal section with a step-wise focussing in *z*-direction (i.e., in the flow direction) by the chevrons. The simulation reveals the temporal evolution of the concentration in the sample stream (i.e., along the *y*-axis) that yields an almost homogeneous protein concentration along the *z*-axis in the measuring channel.

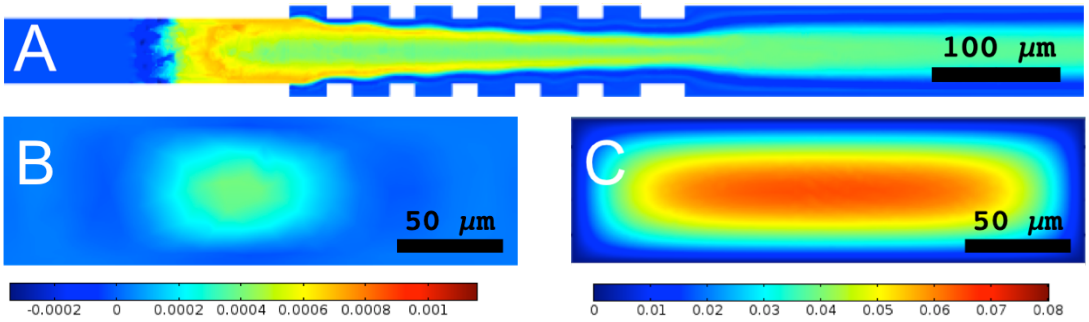

Figure 4.7: Different sections through the channel in figure 4.6. The sectional view of the protein concentration along the flow direction showing the focussing in *z*-direction by the chevrons in the mixing section (A). A transverse cross-section of the protein concentration in the measuring channel, depicting the focussing of the sample stream in *y*- and *z*-direction (B). A cross-section of the velocity distribution at the same place as in B (C).

Panels B and C show cross-sections of the protein concentration and the velocity in the measuring channel. The simulations clearly demonstrate the focussing of the sample stream in *y*- and *z*-direction without protein diffusing out of the stream. The concentration in the sample stream is constant and at a relatively high level of 4 µM, which corresponds to the concentration we would obtain if protein solution was mixed with buffer in bulk at a ratio of 2 : 3. At the same time, the velocity dispersion inside the area of the sample stream (panel B, cyan) is very low when compared with the velocity profile in panel C, which is a prerequisite in order to achieve the high temporal resolution needed for measuring dynamics.

Figure 4.8 A displays combined bright-field/fluorescence microscopy image of the device viewed from the top. A *z*-stack of confocal fluorescence images at the position of the red line is shown in panel B, where the flow of the sample stream (green) is observed from the side. The flow ratio between sample stream (fluorescent) and focus stream (water) is 1 : 4. The *z*-stack along the red line shows the focussing in *z*-direction by the chevrons. Similar to the simulations in figure 4.7 A, we can see a step wise decrease of the jet height along the mixing part of the channel. The stream widens again when entering the measuring

channel. This is due to the increased height of this part compared to the mixing channel.

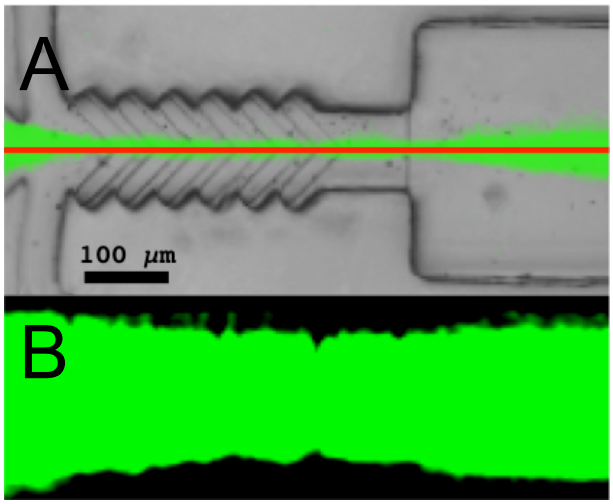

Figure 4.8: Brightfield image of the mixing section overlaid with a fluorescence image (A), the green stream indicates the sample stream. *Z*-stack of the sample stream along the red line in panel A (B). The scale is the same for both images.

4.3 SAXS experiments

The fast mixing device was tested in SAXS experiments at the Swiss Light Source (SLS) in Villigen as well as in-house. We chose lysozyme as a model protein for unfolding and refolding measurements.

4.3.1 Lysozyme

Lysozyme is a small globular protein present in egg white and many secretions such as tears, saliva or mucus. It is a glycoside hydrolase and as such cleaves the sugar chains of peptidoglycans in Gram-positive bacteria[141]. Lysozyme is thus a part of the innate immune system and its lack or decreased levels of lysozyme

could be linked to various chronic diseases, such as bronchiopulmonary dysplasia or conjunctivitis[142-144].

The folding mechanism of lysozyme has been studied intensively, and consecutively lysozyme is one of the best-known models for protein folding. The refolding of lysozyme occurs stepwise, with a fast first step driven by hydrophobic interactions in the time scale of about 1 ms, the folding from this intermediate step into the native state takes approximately 400 ms[145,146]. The shape of lysozyme changes slightly from an ellipsoidal body during the intermediate state to a more spherical shape in native state (see figure 4.9). This is reflected by a decrease of the radius of gyration during the folding process[146].

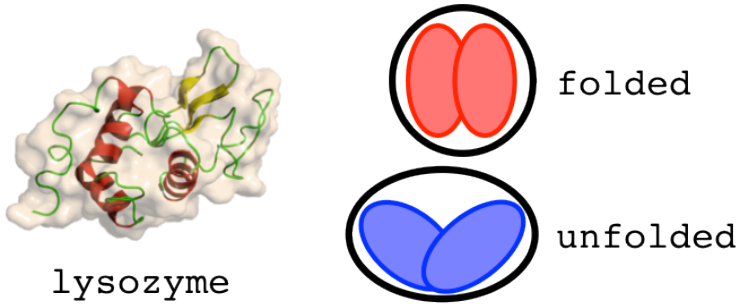

Figure 4.9: Lysozyme has an almost spherical shape in folded state, while in unfolded state it resembles an ellipsoid.

In our experiments, lysozyme was unfolded using high concentrations (3 M) of guanidine hydrochloride (GdmCl) and was refolded by dilution down to 0.6 M GdmCl. These conditions led to fast unfolding and a slow refolding of lysozyme in continuous and stopped flow measurements, performed by Segel *et al.*[146].

4.3.2 Buffers used to fold and unfold lysozyme

In order to measure lysozyme in different conformations and during folding or unfolding reactions, several buffers were needed. For all buffers, the substances were dissolved in Milli-Q water and the pH was not adjusted. Table 4.1 shows the buffers used during the experiments with lysozyme.

Folding and unfolding of lysozyme was mainly controlled through the concentration of guanidine hydrochloride (GdmCl). Consequently, whenever lysozyme was in folded condition, GdmCl concentration was 0.6 M and while in unfolded condition it was 3 M. Buffers 1 and 2 are the starting buffers for unfolding or folding experiments. For unfolding experiments, lysozyme was dissolved in buffer 1 and diluted with buffer 3, whereas for folding experiments, it was dissolved in buffer 2 and diluted with buffer 4. For all measurements in the microfluidic device the ratio of the buffers was 1 : 4 of starting buffer (with dissolved lysozyme) to dilution buffer.

	folded (1)	unfolded (2)	to unfold (3)	to refold (4)	after unfolding (5)	after refolding (6)
GdmCl	0.6 M	3 M	3.6 M	-	3 M	0.6 M
glycine	-	20 mM	25 mM	-	20 mM	4 mM
Na-acetate	50 mM	-	-	62.5 mM	10 mM	50 mM

Table 4.1: Buffer concentrations for different lysozyme states and experiments. 1 & 2 are the starting buffers for mixing experiments, with lysozyme in either folded, or unfolded state. 3 & 4 are the expected end concentrations of unfolding or folding experiments in the microfluidic channel and buffers 5 & 6 are the dilution buffers used to get from buffer 1 to 3 and from 2 to 4, respectively.

To ensure that we are actually able to measure differences in lysozyme states in the microfluidic device, we performed measurements without mixing and thus without any folding or unfolding dynamics. Hence, lysozyme was dissolved in buffers 1 and 2 (referring to the starting conditions for mixing) and in buffers 5 and 6 (corresponding to the end conditions after mixing). These solutions were measured in the device at low flow velocities of 0.05 µl/s for each inlet. We will refer to these experiments in the following as “measurements without mixing”.

4.3.3 Measurements without mixing

The goal to measure fast dynamics of protein folding with an in-house SAXS setup seems very ambitious, considering that the intensity of in-house X-ray sources is about 10^6 times lower than the radiation at synchrotrons, in combination with the very small sample volumes (less than 10 nl) and the weak scattering of biomaterials. Consequently, we started with simple measurements without any reaction dynamics (i.e. without mixing) in order to confirm the possibility to measure lysozyme in a microfluidic device with a lab-source SAXS-setup. We started with high lysozyme concentrations of 30 mg/ml, progressed with lower protein concentrations similar to the ones in the dynamic measurements (6 mg/ml) and finally measured the dynamics of unfolding and folding at SLS and in-house. All measurements were performed using a NOA 81/polystyrene microfluidic device as described in section 2.2.7. For all measurements without mixing, the solutions were pumped through all inlets at low flow rates (0.2 µl/s in total) to avoid beam damage on the protein or sticking of the protein to the channel wall.

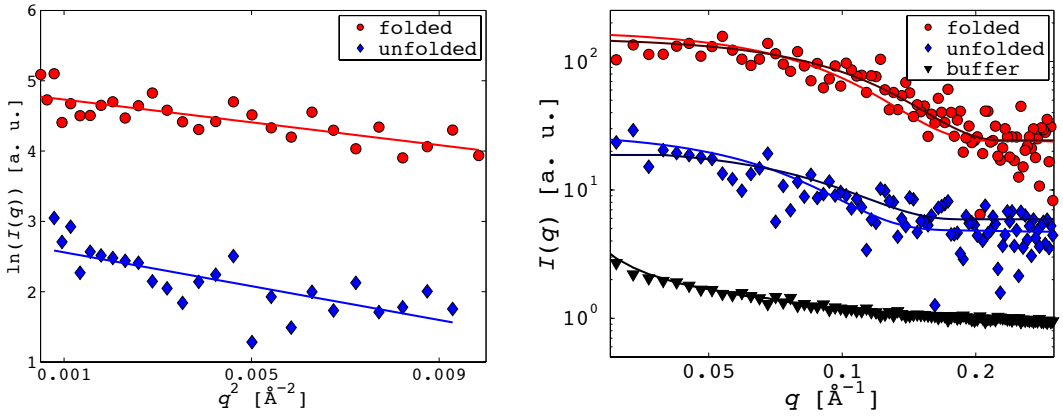

Figure 4.10: Scattering data of lysozyme in folded and unfolded state in the microfluidic device in-house, using buffers 1 and 2. Left image shows the Guinier plot with the fitted line. The right plot displays the scattering intensities, fits for spherical particles with (normal color) and without fixed radii (dark color).

Figure 4.10 shows the scattering intensities of lysozyme (30 mg/ml) dissolved in buffer 1 and 2 for folded and unfolded state respectively. The data was analysed

using the Guinier method to calculate the radius of gyration (left plot in figure 4.10). The calculated radii of gyration in figure 4.10 were $R_{g,\,folded}$ = 15.6 Å ± 0.4 Å and $R_{g,\,unfolded}$ = 19.0 Å ± 0.3 Å. These values are in very good agreement to the data of Segel *et al.* measured in a stopped flow device at synchrotron (R_g = 16.0 Å ± 0.2 Å for folded and R_g = 19.6 Å ± 0.2 Å for unfolded lysozyme)[146]. Subsequently, the calculated radii were used to fit a scattering curve on the collected data (right plot, normal colours). In addition, the data was fitted normally, as described in section 2.5.1 and the radii of gyration were calculated from the resulting radii ($R_g = (3/5)^{0.5} \cdot R$). For these calculations we got $R_{g,\,folded}$ = 14.9 Å and $R_{g,\,unfolded}$ = 18.7 Å. The radii of gyration calculated by Guinier analysis and the ones obtained by fitting have comparable values, indicating a small error of our measurements.

The second step was to measure lysozyme in all four possible buffers (1, 2, 5 and 6). Accordingly, we measured the protein in the two possible starting and in the two corresponding end conditions. The lysozyme concentration was 30 mg/ml.

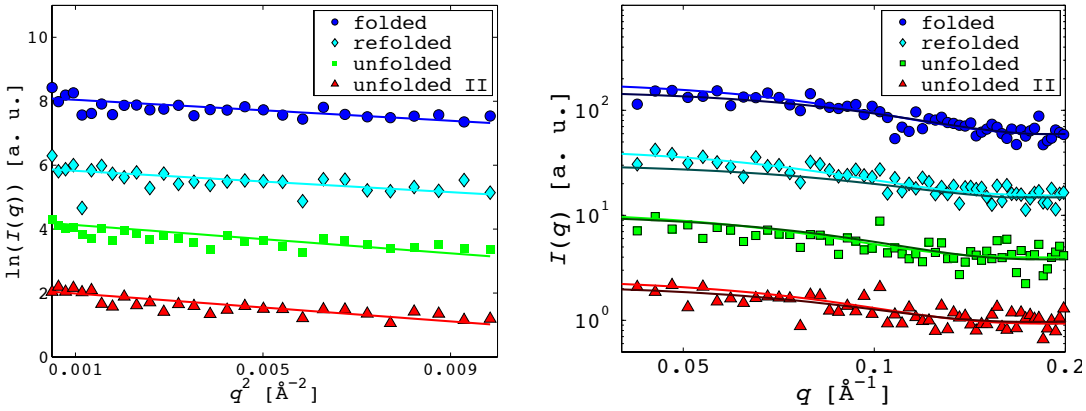

Figure 4.11: Lysozyme dissolved in all four buffers. Starting buffers for folded and unfolded conditions and end conditions with buffer 5 (unfolded II) and buffer 6 (refolded). Left side shows the Guinier plot with linear fits and the right plot contains the data fitted with (normal colours) and without (dark colours) fixed radii.

Figure 4.11 shows the Guinier plots to calculate the R_g and the collected intensity curves including the fits for the calculated R_gs. The values of the radii of gyration were still in reasonable agreement to the data from the literature:

$R_{g,\,folded}$ = 15.7 Å ± 0.3 Å, $R_{g,\,refolded}$ = 15.8 Å ± 0.2 Å, $R_{g,\,unfolded}$ = 18.2 Å ± 0.2 Å and $R_{g,\,unfolded\,II}$ =18.1 Å ± 0.3 Å. The radii obtained by fitting are $R_{g,\,folded}$ = 17.0 Å, $R_{g,\,refolded}$ = 17.5 Å, $R_{g,\,unfolded}$ = 18.8 Å and $R_{g,\,unfolded\,II}$ =19.4 Å. These values are slightly shifted towards higher radii, nevertheless, a clear difference between folded and unfolded samples can be observed. All values, however, are still in reasonable proximity to the ones measured before (figure 4.10).

The last experiment without mixing included the decrease of lysozyme concentration to 6 mg/ml, which should be the final lysozyme concentration during dynamic (i.e. mixing) measurements. Figure 4.12 shows the Guinier plots and the scattering curves of lysozyme dissolved in buffers 5 and 6, thus having the same buffer conditions as after mixing. We calculated radii of gyration of $R_{g,\,refolded}$ = 16.4 Å ± 0.4 Å and $R_{g,\,unfolded}$ = 18.8 Å ± 0.2 Å for the refolded and unfolded lysozyme, respectively. The scattering curves have a larger spreading (i.e. more scattering noise) compared to the measurements with 30 mg/ml, yet the Guinier plots show a clearly linear behaviour and the calculated R_gs are similar to the ones calculated earlier. The radii acquired by fitting are $R_{g,\,refolded}$ = 17.4 Å and $R_{g,\,unfolded}$ = 19.1 Å, showing that even with low protein concentration and higher signal noise we are still able to reliably calculate the radius of gyration.

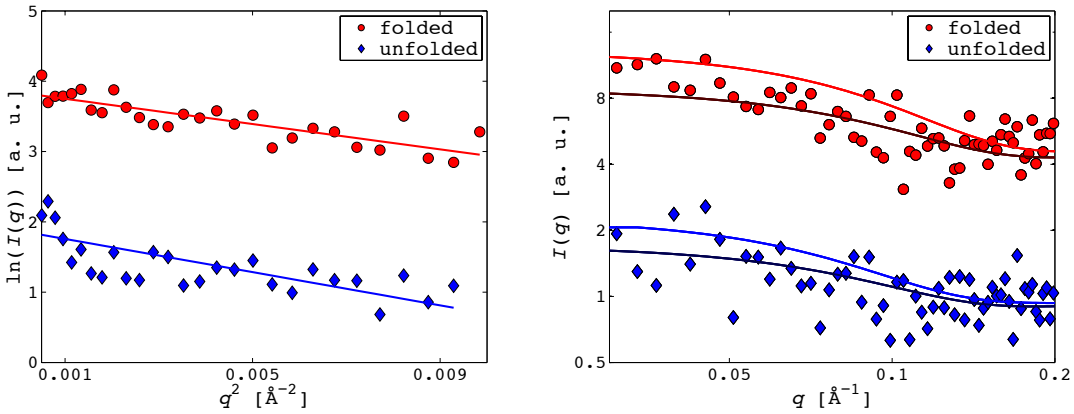

Figure 4.12: Lysozyme in folded and unfolded state (buffers 5 and 6). Linear Guinier plots on the left and fitted scattering curves on the right (normal colour with and dark colour without fixed radii) .

For all measurements without mixing, we were able to calculate meaningful radii of gyration and reasonably fit the scattering data. Hence, the successful measurement of different states of lysozyme even at low concentrations in the microfluidic device could be confirmed. The measured R_gs are all within reasonable range of the values found in literature (measured in stopped flow devices at synchrotron)[146].

4.3.4 Synchrotron experiments of unfolding lysozyme

In a collaborative work together with Ivan Rajkovic and Andreas Menzel from the PSI in Villigen, the fast mixing devices could be tested at synchrotron radiation at the Swiss Light Source (SLS). For unfolding experiments of lysozyme, a Kapton®/PDMS device with a 150 μm wide measuring channel was used. 30 mg/ml Lysozyme was dissolved in 0.6 M GdmCl buffer (buffer 1). The solution was pumped at 0.06 μl/s per inlet (cf. red inlet figure 4.1) and mixed with unfolding buffer (5.6 M GdmCl, 33 mM glycine, 35 mM HCl) in a 2 : 3 ratio resulting in a 12 mg/ml lysozyme solution in 3.6 M GdmCl. Measurements were taken in the channel in periodical distances resembling 10 ms in reaction time. In this manner, the unfolding reaction was monitored in a time window from 10 ms to 400 ms. Exposure time was 200 ms at each position and every position was measured 70 times. Additionally, the beam intensity was attenuated to avoid heavy beam damage on the device, which had been observed in earlier measurements (figure 4.13).

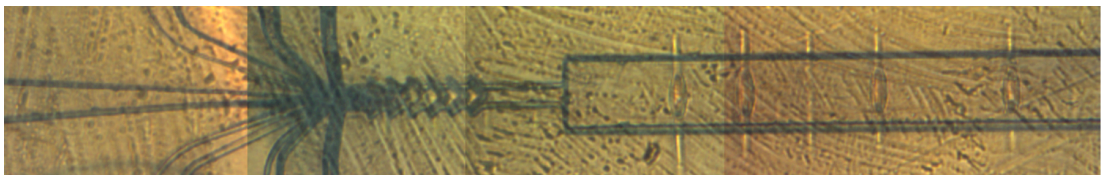

Figure 4.13: Photograph of the microfluidic mixing device after measurements at the synchrotron. Beam damage is clearly visible and resulted in changing background signals during preliminary measurements. As a consequence, the integration times have been drastically reduced in later experiments.

Figure 4.14 shows the scattering intensity of buffer with the final salt concentrations as a background measured in the channel. As can be seen, the device had a strong background signal in a wide *q*-range, also interfering with the signal of lysozyme between 0.05 Å^{-1} and 0.2 Å^{-1}.

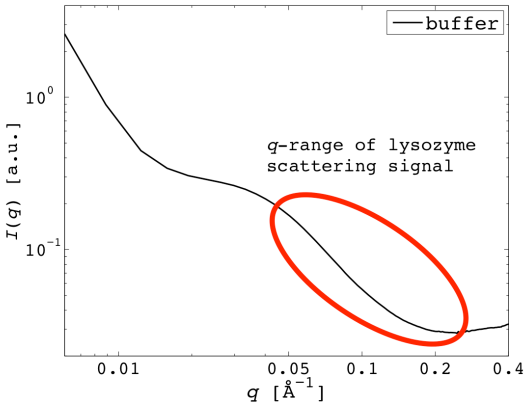

Figure 4.14: Scattering intensity of buffer in the microfluidic device. The red ellipsoid displays the area, where we expect the lysozyme signal.

Still it was possible to measure the scattering intensities of lysozyme during the reaction, showing partial unfolding between 30 ms and 270 ms of elapsed time (figure 4.15). Due to the large noise of scattering signal at very low q-values (around 0.05 Å^{-1}), fitting the linear Guinier plot was not possible. As a consequence, we fitted the data manually for radii of gyration of $R_{g,\,30\,ms}$ = 16.0 Å, $R_{g,\,120\,ms}$ = 16.2 Å and $R_{g,\,270\,ms}$ = 16.4 Å (figure 4.15, left plot). The selected R_gs seemed to be a reasonable choice for the first steps of an unfolding reaction and also fitted our data quite well. A fit for a spherical shape was applied to the scattering data, using the selected radii of gyration as a fixed parameter (figure 4.15, right plot, normal colours). The fits show a good congruency with the collected data and hence prove the plausibility of the selected R_gs. However, when fitting the data without fixed values for the radii, the results differed heavily: $R_{g,\,30\,ms}$ = 12.5 Å, $R_{g,\,120\,ms}$ = 13.0 Å and $R_{g,\,270\,ms}$ = 13.1 Å (figure 4.15, right plot, dark colours).

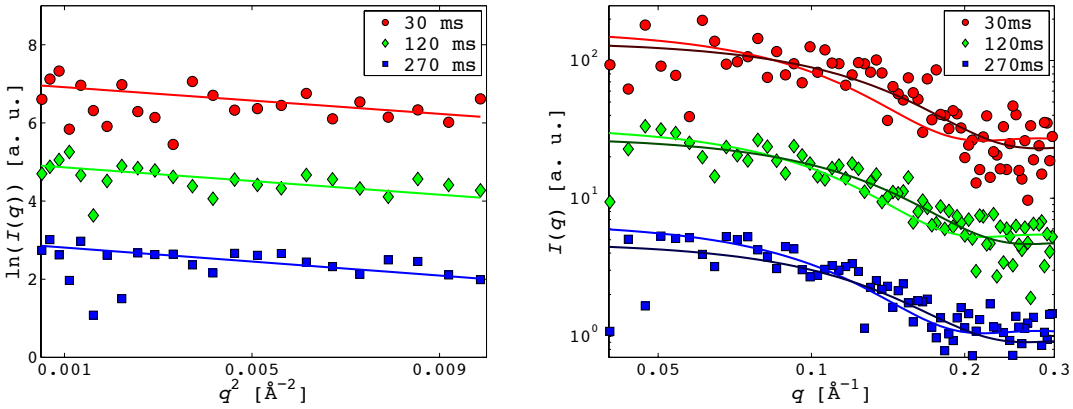

Figure 4.15: Guinier plots and scattering curves of an unfolding reaction of lysozyme at three different time points. The data is very noisy especially at low q-values. Hence, the Guinier plot was manually fitted.

The large differences between the radii calculated by Guinier analysis and the ones obtained by fitting indicate the troubles we encountered when measuring at SLS. This seems to be unintuitive, as higher intensity and smaller beam should lead to a better signal and higher temporal resolution. However, the problem is exactly the high intensity of the synchrotron radiation. As already shown in figures 4.13 and 4.14, the device has a strong background signal and even suffers from radiation damage. Taking into consideration the much stronger background signal compared to the lysozyme signal, it is actually remarkable, that we are at all able to get some intensity curves for lysozyme. This fact is encouraging for future experiments, as we also changed the device to decrease the background signal (cf. section 4.5).

4.3.5 In-house experiments of folding lysozyme

To increase the scattering signal for in-house measurements, the concentration of lysozyme in the starting solutions was set to 50 mg/ml, leading to a final concentration of 10 mg/ml. All measurements were taken at the same spot of the channel with varying flow speeds, resulting in different reaction times from 10 ms to 100 ms. Starting solutions were lysozyme in buffer 2 and dilution buffer 4 (c.f. table 4.1) to refold lysozyme into its native state. The exposure time

for the SAXS measurements was twice 4 hours, limited by the syringe sizes available.

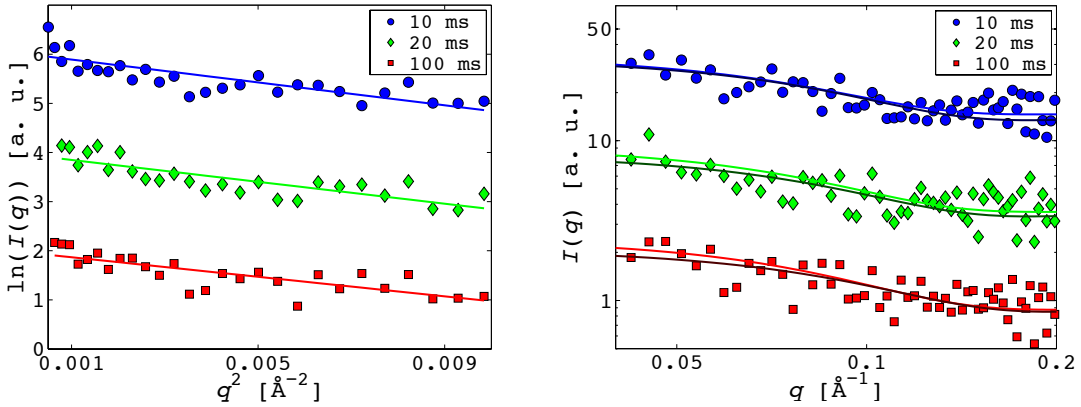

Figure 4.16: Scattering intensities during refolding in the fast mixing device. Guinier plots on the left side to calculate the R_gs and the data fitted with a spherical form factor and a fixed (normal colours) and without fixed (dark colours) radius on the right side.

We compare measurements at a reaction time of 10 ms, 20 ms and 100 ms (figure 4.16) during refolding of lysozyme. Again, the radii of gyration were calculated first, using the Guinier method. The resulting R_gs are: $R_{g,\,10\,ms}$ = 18.7 Å ± 0.3 Å, $R_{g,\,20\,ms}$ = 18.3 Å ± 0.4 Å and $R_{g,\,100\,ms}$ = 17.2 Å ± 0.4 Å. The fits using these radii of gyration (normal colours in figure 4.16 right plot) showed good agreement with the fits without fixed radii (dark colours) and both also accord well with the measured scattering data. Radii of gyration obtained by fitting are $R_{g,\,10\,ms}$ = 19.4 Å, $R_{g,\,20\,ms}$ = 19.1 Å and $R_{g,\,100\,ms}$ = 17.4 Å. The small change in the radii of gyration from 10 ms to 100 ms reaction time suggests, that the folding of lysozyme is still in progress and we did not reach a fully folded state during these experiments.

In figure 4.17 we plotted the three calculated radii of gyration for the folding reaction (light blue) and the radii obtained from the measurement of completely unfolded and completely folded lysozyme at 0 ms and infinite time, respectively (dark blue, data from figure 4.10). There is a clear decrease in R_g along the reaction time axis, however, at 100 ms lysozyme is still present in an intermediate state. Thus we can conclude, that the folding process is not

completed and are likely to be finished at reaction times much higher than 100 ms.

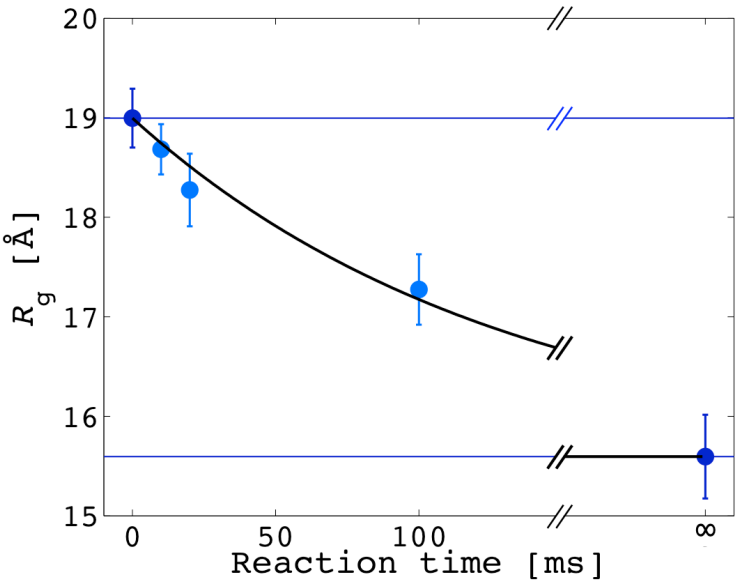

Figure 4.17: Radii of gyration of lysozyme during refolding reaction. Light blue are the values obtained in dynamic measurements (figure 4.16) and dark blue the values of measurements without mixing of folded and unfolded lysozyme (figure 4.10). Black line is a fit using a first order reaction.

The temporal evolution of the radius of gyration was fitted using the equation for a first order reaction (eq. 4.5). In our case, A is the radius of gyration of the folded lysozyme while B is the difference in radius between the fully folded and completely unfolded state. The rate constant k was calculated to be $k = 7.7\ s^{-1} \pm 2.2\ s^{-1}$.

$$R_g(t) = A + B \cdot e^{-kt} \tag{4.5}$$

4.4 Discussion and conclusions

We created a fast mixing device combining different aspects of mixing. Parallel lamination in combination with hydrodynamic focussing provides a very fast and highly controllable mixing. The combination of flow-defining structures (chevrons) on top and bottom of the channel together with the hydrodynamic focus enable the sample jet to be focussed in the centre of the channel and in this manner reducing the velocity distribution in *y*- and *z*-direction, which was approved by confocal microscopy. The flexibility of soft lithography allows the fabrication of various devices with only little additional effort, thus enabling the production of devices suitable for any kind of measurement, be it at synchrotrons or in-house.

We approached the difficulties of measuring protein folding dynamics in microfluidics step by step. First showing, that we are able to distinguish between folded and unfolded lysozyme at high concentrations and subsequently also at lower concentrations on an in-house SAXS setup in microfluidics. Unfolding and folding experiments at synchrotron and in-house proved, that mixing in the device is working and we therefore can measure along the time axis of a reaction. Although the background scattering from the device was very strong when measuring at the SLS, which made it difficult to analyse the scattering data, we were able to calculate the radii of gyration during unfolding of lysozyme in three different states (i.e. at three different positions along the channel).

The folding experiments on our in-house SAXS successfully proved that it is possible to follow the dynamics of protein folding even on much lower intensity of X-ray radiation. We were able to calculate the radii of gyration for lysozyme in different states; folded, unfolded and intermediate state R_gs were in agreement with the values found in literature.

4.5 Outlook

The versatility of soft lithography and microfluidics in general leads to a diversity of possible device fabrication methods (cf. sections 2.2.3 – 2.2.8). Throughout this work, two versions of our fast mixing device were produced, matching the needs of the corresponding setup (synchrotron and in-house SAXS measurements). As radiation damage at synchrotrons is a big issue with polymer films (Kapton®, polystyrene) and device forming material (PDMS, NOA 81), variations of these devices might overcome this problem in future experiments.
A device with a narrow (200 µm) glass capillary instead of the measuring channel could already be fabricated (figure 4.18 A). In this way, the reactants are mixed inside the Kapton®/PDMS device, and the reaction is measured in the capillary.
Combining the easy to handle PDMS device together with a narrow capillary (< 10 µm nozzle) could be an application for fourth generation synchrotron facilities such as the X-FEL[147] or the SwissFEL[148] (cf. figures 2.9 and 2.13).

The ability to measure fast dynamics in an in-house setup will undoubtedly be of high importance, as lab SAXS setups are more available than beam time at synchrotron facilities. Together with the continuously increasing quality of table-top X-ray sources the possibility to measure reaction times down to a few milliseconds opens a variety of applications.
Besides *in situ* observations of rapid protein folding, the packing and unpacking of DNA is another interesting topic in research on biological systems[149]. The interaction between DNA and histones is one important part of DNA packing and can be mimicked using charged spherical molecules (i.e. dendrimers)[77]. Investigating the process of DNA packing and unpacking with SAXS and fast mixing microfluidic devices could help to learn details about the densest way of packing information in both, biology and technology[76,149].
Another application of mixing in microfluidic devices has been the creation of fibres such as silk[73]. The goal of these experiments is to fabricate silk fibres with

similar properties than native silk. Dimensions of the middle jet as well as flow velocity and resulting shear forces at the interface determine the size of resulting fibres and also their secondary structure. The highly controllable environment in our device (five sample inlet, sheath flow for focussing, chevrons for *z*-focus) might improve the creation of artificial silk and other fibres.

5 Flow dynamics in microfluidics measured by XPCS

5.1 Introduction

Third generation synchrotron sources provide partially coherent X-rays with intensities several orders of magnitude higher than previously available. This allows the use of coherent scattering techniques such as X-ray photon correlation spectroscopy (XPCS)[150]. XPCS is based on temporal intensity fluctuations of speckle patterns[150,151]. This phenomenon occurs due to changes in the spatial arrangement of the scattering objects. Time correlations of such speckle patterns are directly related to microscopic motions, such as Brownian diffusion or active transport.

Similar to dynamic light scattering or particle image velocimetry, XPCS can thus be used to study the dynamic processes of colloidal materials[152]. However, due to its high penetration depth and large range of momentum transfer q, XPCS is also applicable to probe opaque samples and access dynamics at much smaller length scales down to few Å[153]. Thus, not only colloidal samples but also polymeric materials can be studied[154].

These advantages of XPCS over other techniques together with the possibility to focus X-ray beams down to several hundred nanometres prove to be ideal to observe the dynamics in microfluidic devices. We used XPCS to measure the impact that different geometrical features of a microfluidic channel can have on the flow. Using a 2D X-ray detector, we were able to calculate the autocorrelation functions for each pixel of the scattering image, resulting in a sequence of correlation images, or in other words a correlation movie.

5.2 Theory of XPCS

The temporal intensity fluctuations $I(q,t)$ of speckle patterns can be analysed by calculating an autocorrelation function of the intensity:

$$g_2(q,t) = \frac{\langle I(q,t) \cdot I(q,t+\tau) \rangle}{\langle I(q,t) \rangle^2} \tag{5.1}$$

Angled brackets denote the time average, q is the scattering vector, t a given time point and τ the time shift relative to t. The intensity correlation function (6.1) is related to the intermediate scattering function g_1 via the Siegert relation[155]:

$$g_2(q,t) = 1 + \beta |g_1(q,t)|^2 . \tag{5.2}$$

Where β is the speckle contrast.

In the case of colloids in laminar flow, the autocorrelation function can be split into three independent parts contributing to the final function: the diffusive motion of the scattering object due to Brownian motion, the transit time of the colloids moving through the scattering volume and the Doppler shifts arising due to particles flowing with different flow velocities in the scattering volume[155].

The contribution of Brownian motion to the autocorrelation function in shear flow is given by

$$|g_1(q,t,\gamma)|^2 = \exp\left[-2Dq^2t\left(1 - \frac{q_{\parallel}q_{\perp}}{q^2}\gamma t + \frac{q_{\parallel}^2(\gamma t)^2}{q^2 3}\right)\right], \tag{5.3}$$

where $q_{\parallel}$ and $q_{\perp}$ are the components parallel and perpendicular to the flow direction of the scattering vector q. γ is the shear rate and D the diffusion

coefficient. In a scattering geometry perpendicular to the flow $q_{\parallel} = 0$, consequently g_1 is independent of the shear rate.

The second contribution to the intensity fluctuation is defined by the constant flow of the particles through the sample volume (i.e. the X-ray beam). This phenomenon is described by the transit frequency $\nu_{tr} \sim v_0/h$, where h is the length of the sample volume and v_0 the flow velocity. With the assumption, that the beam has a Gaussian profile, this leads to

$$\left|g_1(q,t)\right|^2 \propto \exp\left[-\left(\nu_{tr}t\right)^2\right]. \tag{5.4}$$

The third effect, contributing to the intermediate scattering function is due to shear-induced effects, resulting in particles moving with different velocities. This can be described by a double integral over the scattering volume with an approximated form of a line with the length R[156]:

$$\left|g_1(q,t)\right|^2 = \frac{1}{R^2}\int_{-R}^{R}\int_{-R}^{R}\cos\left(qt\delta v\left(r_1,r_2\right)\right)dr_1dr_2, \tag{5.5}$$

where δv is the velocity difference between two particles separated by the distance r_1-r_2. The integral has been solved analytically for a uniform shear rate[157]:

$$\left|g_1(q,t)\right|^2 = \left[\frac{\sin\Gamma_S t}{\Gamma_S t}\right]. \tag{5.6}$$

Γ_s is the shear relaxation rate and depends on q as well as the flow velocity ($\Gamma_s = q_{//}v$). Busch et al.[156] have also calculated a more complex equation for the contribution of shear in Poisseuille flow (i.e. a parabolic flow profile). However, due to the very small beam dimensions in our case we assume a constant average shear rate in y-direction inside our sample volume. This results in a

situation similar to the one for homogeneous flow as discussed by Burghardt *et al.*[153] and Narayanan *et al.*[157]. As a consequence we consider the simpler equation 5.6.

Combining the three contributing factors we get the following two equations for the autocorrelation functions perpendicular and parallel to the flow direction[155]:

$$g_{2,\perp}(q,t) = 1 + \beta \cdot \exp\left[-2Dq^2 t\right] \cdot \exp\left[-\left(v_{tr} t\right)^2\right] \tag{5.7}$$

$$g_{2,\parallel}(q,t) = 1 + \beta \cdot \exp\left[-2Dq^2 t\right] \cdot \exp\left[-\left(v_{tr} t\right)^2\right] \cdot \left[\frac{\sin\left(\Gamma_S t\right)}{\Gamma_S t}\right] \tag{5.8}$$

Equation 5.1 was used to calculate the autocorrelation image sequence from the scattering images. In this project, we used equations 5.7 and 5.8 to fit the calculated autocorrelation functions in directions perpendicular (5.7) and parallel (5.8) to the flow direction in the channel.

5.3 Setup and materials

5.3.1 X-ray setup at DESY

The experiments were carried out at the partially coherent beamline P10 at PETRA III at Deutsches Elektronen Synchrotron (DESY) in Hamburg, Germany. The energy of the X-rays was fixed to 8050 eV, corresponding to a wavelength of λ = 1.54 Å. The beam was focussed using compound refractive lenses down to a size of 5 x 5 μm^2. A Maxipix[34] 2 x 2 detector was installed 4970 mm behind the sample position using an evacuated flight tube. The active area of the detector had 516 x 516 pixels with a pixel size of 55 x 55 μm^2. Figure 5.1 shows an overview over the X-ray setup used for XPCS measurements including a scheme of the three measured channel geometries.

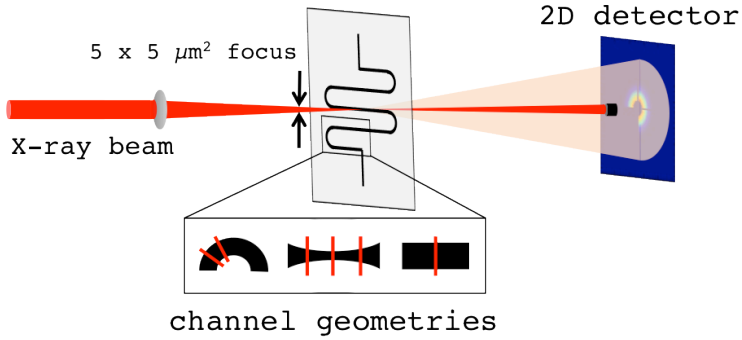

Figure 5.1: Scheme of X-ray setup used for XPCS. The beam was focussed down to 5 x 5 µm². Three different channel geometries where measured.

5.3.2 Colloids

SiO_2 nano-particles were used for XPCS. They had a diameter of 160 nm ± 20 nm. Figure 5.2 shows the scattering intensity of the nanoparticles used in the experiment.

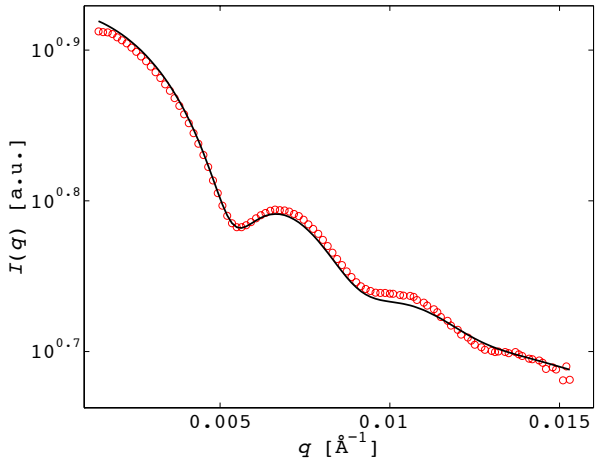

Figure 5.2: Scattering intensity of the used SiO_2-particles including a fit (black line), confirming a radius of 80 nm ± 10 nm.

The colloids were produced by poly-condensation of tetraethyl-orthosilicate [$Si(OC_2H_5)_4$], according to a Stöber synthesis[99]. The particles were further

sterically stabilized with 3-trimethoxysilyl-propyl-methacrylate (TMP, $C_{10}H_{20}O_5Si$) to prevent agglomeration through van der Waals interactions. The nanoparticles were suspended in poly-propylene glycol with an average molecular weight of 4000 g/l and a viscosity of 1300 mPa·s (PPG 4000, Sigma-Aldrich). Synthesis and preparation of the colloids were performed by Fabian Westermeier (Hasylab, Deutsches Elektronen Synchrotron, Hamburg, Germany).

5.3.3 Device

A microfluidic device made of polystyrene foil and UV-curable adhesive (section 2.2.4) and the corresponding holder (section 2.3) were used. The device included a 150 µm wide and 200 µm high main channel with two geometric features: a constriction of 50 µm width and 200 µm length and a curvature of the main channel with a radius of R_c = 0.5 mm. Figure 5.3 shows a schematic overview of the microfluidic channel with the three measurement positions, curved channel (I.), straight channel (II.) channel and constriction (III.).

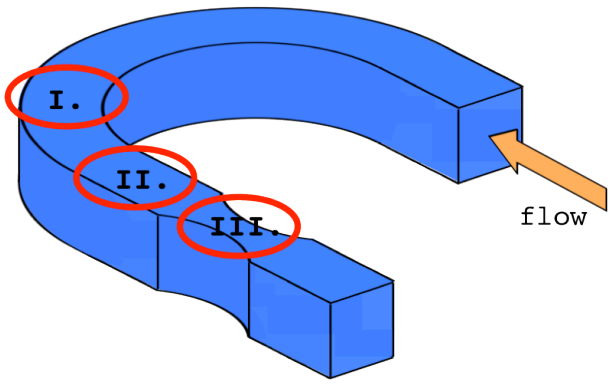

Figure 5.3: Schematic overview of the microfluidic channel used for XPCS experiments. The positions of the measurements were in curvature (I.), straight channel (II.) and constriction (III.).

1 ml plastic syringes (Henke Sass Wolf GmbH, Tuttlingen, Germany) were connected to the device by Teflon (PTFE) tubing. The flow rate was controlled using Nemesys syringe pumps from Cetoni GmbH, Korbussen, Germany.

In each of the three positions, a line scan across the channel was performed. Consequently, we measured 15 – 17 points in straight and curved channels and at 6 – 12 points in the constriction across the channel. The distance between the points was approximately 10 µm. At each of the points, 5000 scattering images were taken with a frame rate of 300 Hz. The line scans in the constriction were located at the narrowest position and 50 µm up- and downstream, respectively. Measurements were taken at flow speeds of 4, 6, 8, 10 and 16 µm/s (average flow velocity at the syringe pump) in straight and curved channels and at flow speeds of 2, 4 and 6 µm/s in the constriction.

5.4 Calculation of full q-range autocorrelation image sequences

For the full analysis of the data, the 5000 scattering images per point were cut to half of the size and binned using a 2 x 2 binning factor. For each of the remaining pixels, an autocorrelation function for the intensity was calculated using equation 5.1. This resulted in a conversion of the scattering images with a time lapse of 3.3 ms between two images to a sequence of full q-space autocorrelation images (i.e. an "autocorrelation movie") representing the intensity correlation functions in each pixel along increasing time shifts (τ) between the scattering images.

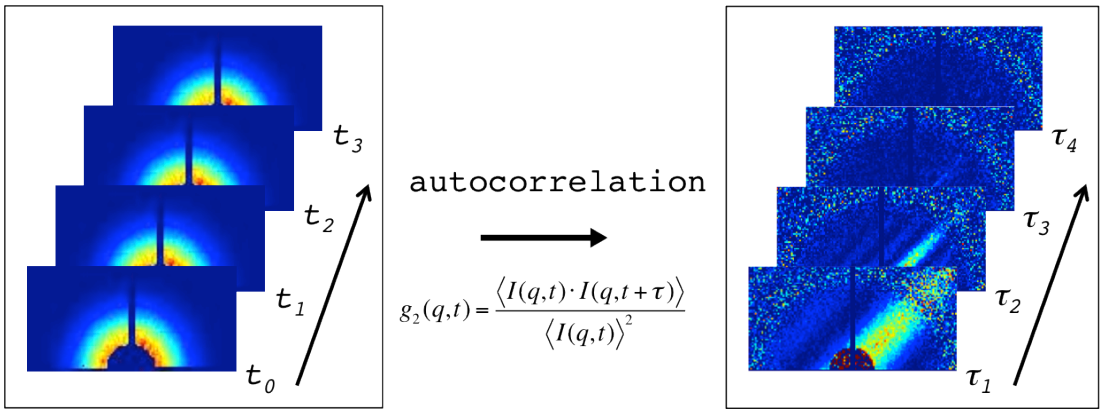

Figure 5.4: Scheme of the conversion of scattering images into a sequence of autocorrelation images. The time axis for the scattering images is the regular time t, while for the correlation image sequence it is the time difference τ between two correlated scattering images (ranging from 3.3 ms up to a maximum of 4999 • 3.3 ms).

The resulting movie or sequence of autocorrelation images provides immediate information about the main properties of the flow in the microchannel. The prominent streak, which is mainly observed at small τ up to 50 - 70 ms (indicated with a red line in figure 5.5), represents the slow decaying correlation in perpendicular direction to the flow. Hence, on the orientation of this streak we can directly monitor the flow direction in the channel (green arrow) and precisely calculate it by plotting the radial intensity distribution. The change of the streaks width with increasing τ depends on the flow velocity, while the length is related to Brownian motion, as the particles move perpendicular to the flow only by diffusion.

Figure 5.5 shows correlation images at four different time shifts τ of a calculated autocorrelation movie. The width of the streak along the red line is rapidly decreasing as τ gets bigger, indicating the much faster flow velocity compared to the diffusion (length of streak is decreasing very slowly). The light blue lines parallel to the red line mainly visible at τ = 10 ms and τ = 30 ms show the effect of multiple particles flowing at different speed inside the sample volume, i.e. the Doppler shift described by equation 5.6.

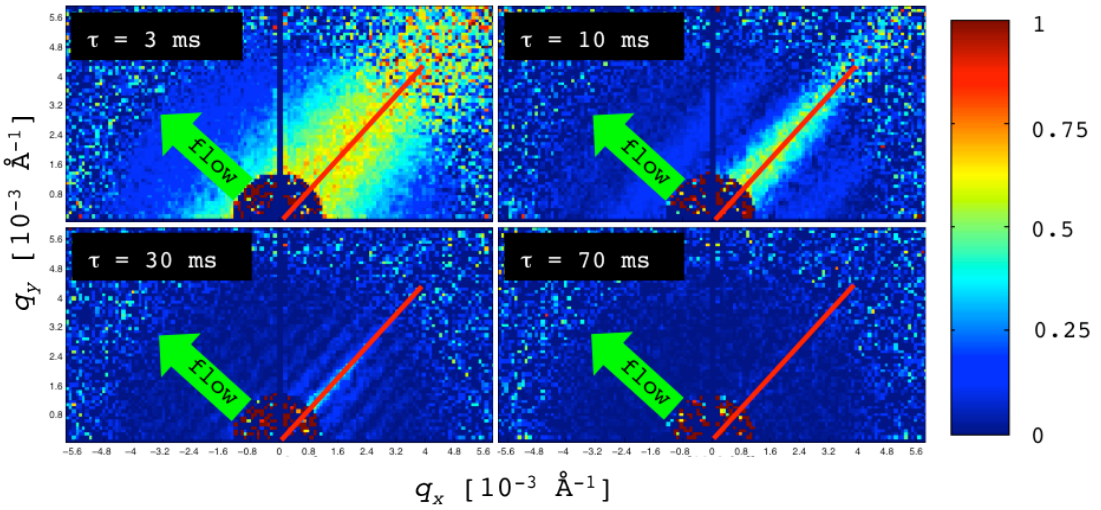

Figure 5.5: Four time points (τ) of a calculated correlation movie. The red line indicates the direction of the slow decaying perpendicular autocorrelation (g_2) and the green arrow shows the flow direction in the channel.

For a more detailed analysis, the autocorrelation functions at a chosen point (i.e. a chosen q-value in x- and y-direction) were recorded from the correlation image sequences. As can be seen on the images in figure 5.5, the correlation is higher for smaller q-values (i.e. decaying faster for increasing q). As a result, a q-value of 0.0015 Å was chosen for all cases when the correlation function g_2 was extracted from the movies. The autocorrelation functions obtained in such manner were fitted using equations 5.7 and 5.8 for the perpendicular ($q_{\parallel} = 0$) and parallel ($q_{\perp} = 0$) case respectively, to access information about flow velocity, shear rate and diffusion constant.

Figure 5.6 shows an example of a correlation image with the two points marked to extract g_2 (green for parallel and red for perpendicular to flow direction). Next to it are the two extracted autocorrelation functions including the according fits. We calculated the average diffusion coefficient by fitting the autocorrelation functions perpendicular to the flow direction of five different velocities (2, 4, 6, 8 and 10 µm/s): $D = 10.5 \cdot 10^{-15}$ m^2/s ± $7.1 \cdot 10^{-15}$ m^2/s. In addition, we fitted the autocorrelation of a no-flow situation with the first part of equation 5.7 (without the second term for transit effects) and got a diffusion coefficient of $D = 13 \cdot 10^{-15}$ m^2/s ± $0.6 \cdot 10^{-15}$ m^2/s.

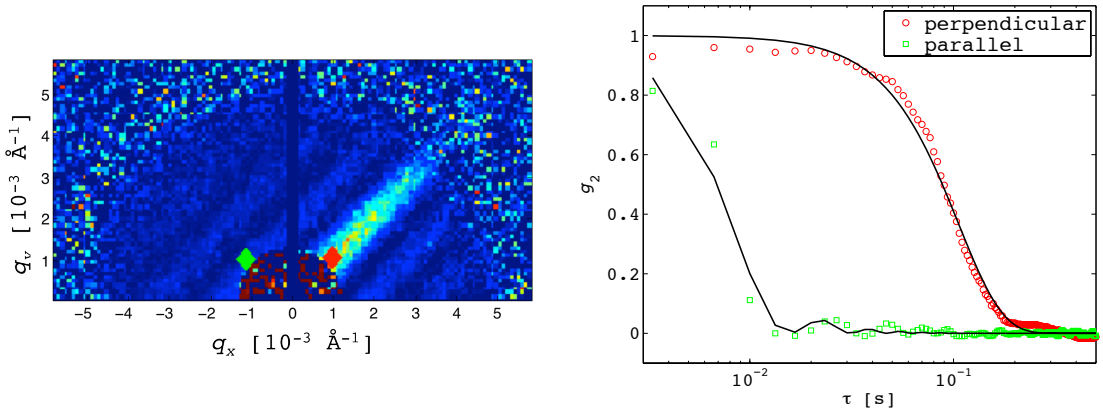

Figure 5.6: Autocorrelation image with the marked points/pixels for extraction of autocorrelation functions in parallel (green) and perpendicular (red) orientation with respect to the flow direction and the two corresponding correlation functions including fits. The measuring position was in the middle of a straight channel for this image. The average flow velocity was 4 µm/s and the correlation image is at τ = 30 ms.

5.5 Results and discussion

This section is divided into two parts, one for the measurements in the constricted channel and another one for the analysis of the flow in curved channels. For both geometries, we first tried to access as much information about the dynamics directly out of the correlation images (e.g. the flow orientation by plotting the radial intensity) and afterwards analysed the extracted correlation functions in order to determine the flow velocities and diffusion constant.

For all the positions in the channels (i.e. the constriction, straight and curved channel), three points of each line scan were chosen, analysed and discussed in detail. For the constricted channel the experiment at $\bar{v}$ = 6 µm/s was selected, while for the curved and straight sections the measurements at $\bar{v}$ = 10 µm/s were considered.

5.5.1 Flow in constrictions

The flow in the constriction was measured at the narrowest part as well as 50 µm up- and downstream. The 2D correlation images of six points were compared. Three points of the line scan in the narrow part and three points in the exit of the constriction 50 µm downstream. Figure 5.7 shows a sketch of the six selected positions in the constriction.

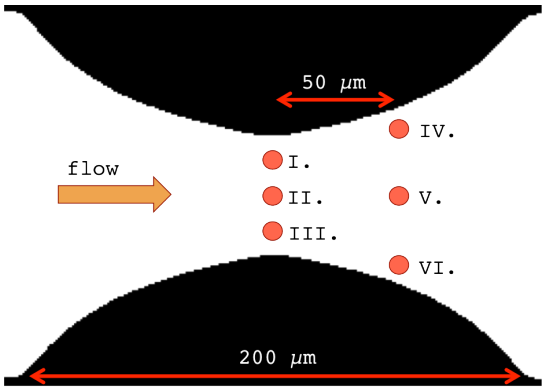

Figure 5.7: Sketch of the constriction with six selected measuring points. I.-III. are in the narrow part and IV.-VI. are in the wider part 50 µm downstream of the narrowest part.

The correlation images at τ = 10 were taken and compared at each point. It has to be noted, that the flow velocity of $\bar{v}$ = 6 µm/s is calculated for the full straight channel meaning that in the narrow constriction (50 µm compared to 150 µm of the full channel) three times higher velocities were observed. For both line scans, we selected a measuring point in the middle of the channel (II. and V.) and one close to each wall (I., III., IV. and VI.). This allowed us to directly see the impact of the wall orientation on the flow direction.

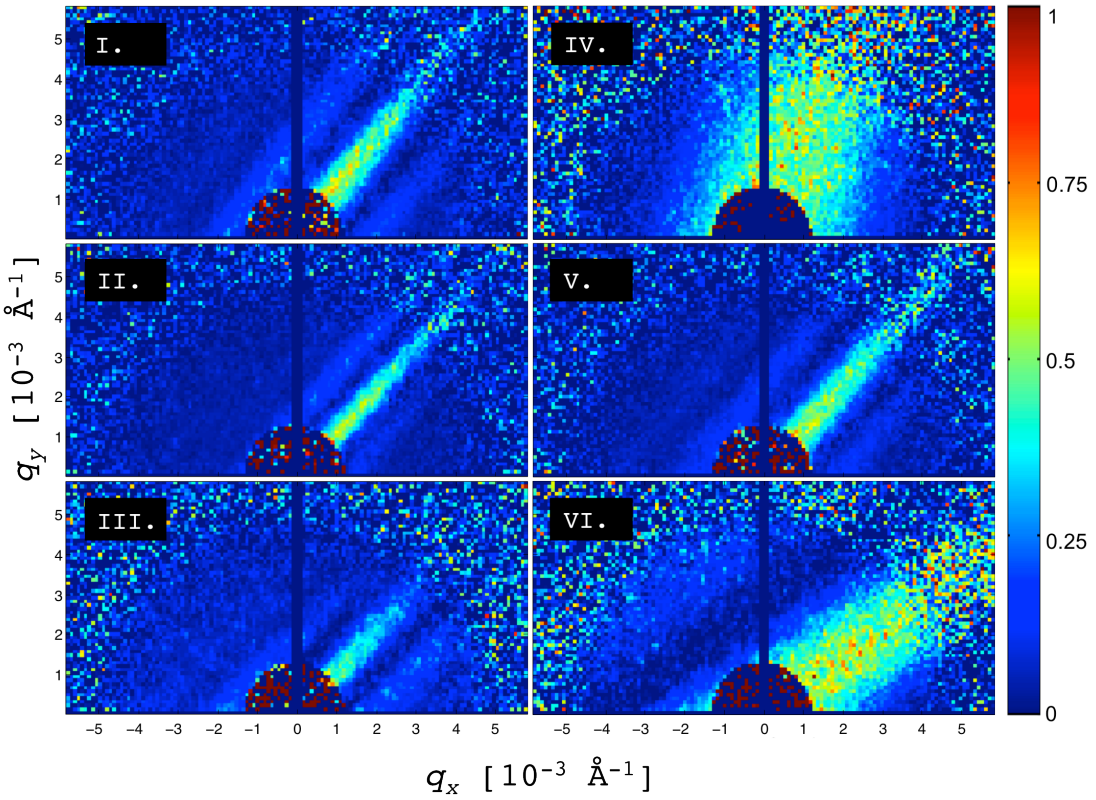

Figure 5.8: Six autocorrelation images of the flow situation in a constriction. I.-III. in the narrowest part, IV.-VI. at a position 50 µm downstream in the constriction. For all six images the time shift is τ = 10 ms and the flow velocity is $\bar{v}$ = 6 µm/s.

Figure 5.8 shows the correlation images of the positions I. – VI.. We tried to access as much information about the device geometry as possible by analysing the images directly rather than the extracted autocorrelation functions. First, the orientation of the flow was analysed. One can see that the flow direction in the narrow part (I. – III.) stays parallel across the three points (i.e. across the channel). This stands in contrast to the situation further downstream (IV. – VI.), where we can observe that the flow direction close to the walls is following the geometry of the channel. The flow in position IV. is slightly tilted to the left (upwards in figure 5.8) in flow direction, whereas in position VI. it is tilted towards the right side in flow direction. The situation in the middle (V.) resembles the positions I. – III. in terms of orientation, showing that the flow in the centre of the channel is not affected by the geometry. We plotted the radial intensity distribution of the images in figure 5.9 A. Compared to the nicely

aligned curves of I. to III., the different positions of the peak maxima for the cases IV. to VI. become obvious in this plot.

Analysing the velocities of the streams, we observe that the difference between the outside streams (I., III., IV., and VI.) and the central streams (II. and V.) is more pronounced in the wider position as compared to the narrow centre position. Still, the velocity difference is visible by comparing the width of the bright streaks. Although the difference in the peak width is not very prominent in the narrow part (I. – III.), it is still possible to see a difference when comparing the distance between the main streak and the first (parallel) streaks of the Doppler shift signal. This situation becomes better visible when looking at figure 6.5 A: the differences in peak width (i.e. the width of the streaks) for situations IV. to VI. are very significant, while for points I. to III. the widths of the peaks differ only slightly. Both the curves for position I. and III. are only slightly wider than the one for position II.. We can also compare the position of the first Doppler signal (i.e. the first peaks on the left side of the prominent main peak) in figure 5.9 A. Here we see, that the green Doppler signal is closer to the main peak, indicating a higher flow velocity.

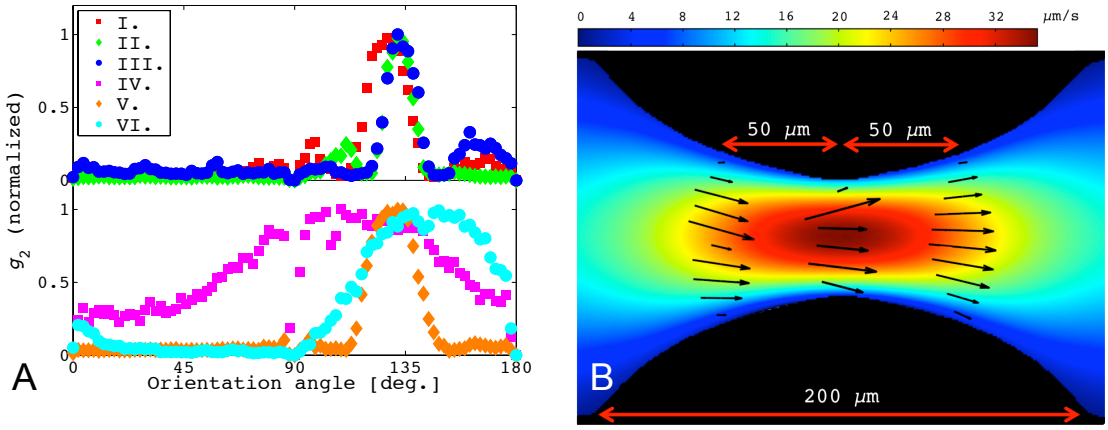

Figure 5.9: Radial intensity plots for the six selected points (A). Calculated flow directions and flow velocities (arrow length) at three different positions across the channel (B).

To get an overview over the flow in the whole constriction, the orientation of the flow was measured at each position across the channel. The autocorrelation

functions parallel to flow direction were extracted and the flow velocities were fitted using equation 5.8. The measured flow directions and velocities are shown in figure 5.9 B. The flow profiles (flow speed corresponds to the lengths of the arrows) of the entrance and exit of the constriction are in very good agreement with the underlaid simulation. Also the fitted velocities in the middle of the constriction are still in good agreement, however, the very high flow velocities at these positions (up to 18 µm/s) make it difficult to fit the autocorrelation functions, due to the limited frame rate of the detector.

The directions of the flow nicely show congruency by all pointing towards the middle of the channel at the entrance of the constriction and towards the channel walls at the exit. In the centre of the constriction one would expect parallel flow streams, which might be the case for the very single point, where the walls are closest. In our case, we probably measured at a very short distance after the narrowest position and therefore the arrows are already pointing towards the channel walls.

5.5.2 Flow in curved channels

For the measurements in curved channels, several line scans along the curvature were measured. For analysis, we chose one line scan in the curvature and compared the results of three points within this scan with a line scan in a straight channel (three points at the same relative position across the channel).

Figure 5.10 shows a sketch of the selected points in the straight channel (I. – III.) and in the curvature (IV. – VI.). The measurement points were at 30 %, 50 % and 70 % relative width of the channel for both the straight and the curved channel (from inside to outside) and the measurements were performed at a mean flow velocity of $\bar{v}$ = 10 µm/s in both channels.

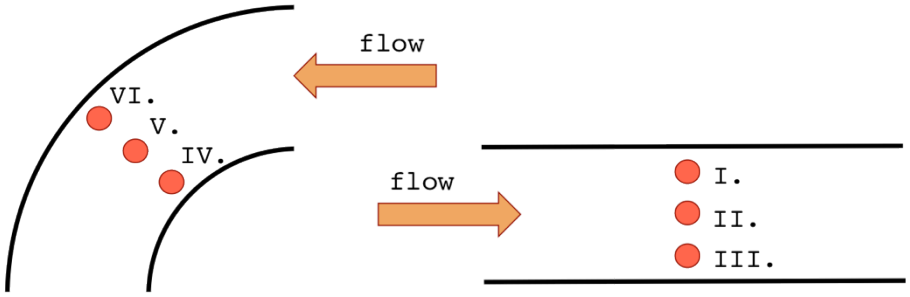

Figure 5.10: Sketch of the selected and analysed points in straight (I. - III.) and curved (IV. - VI.) channel. The exact positions of the points are 30%, 50% and 70% relative width of the channel.

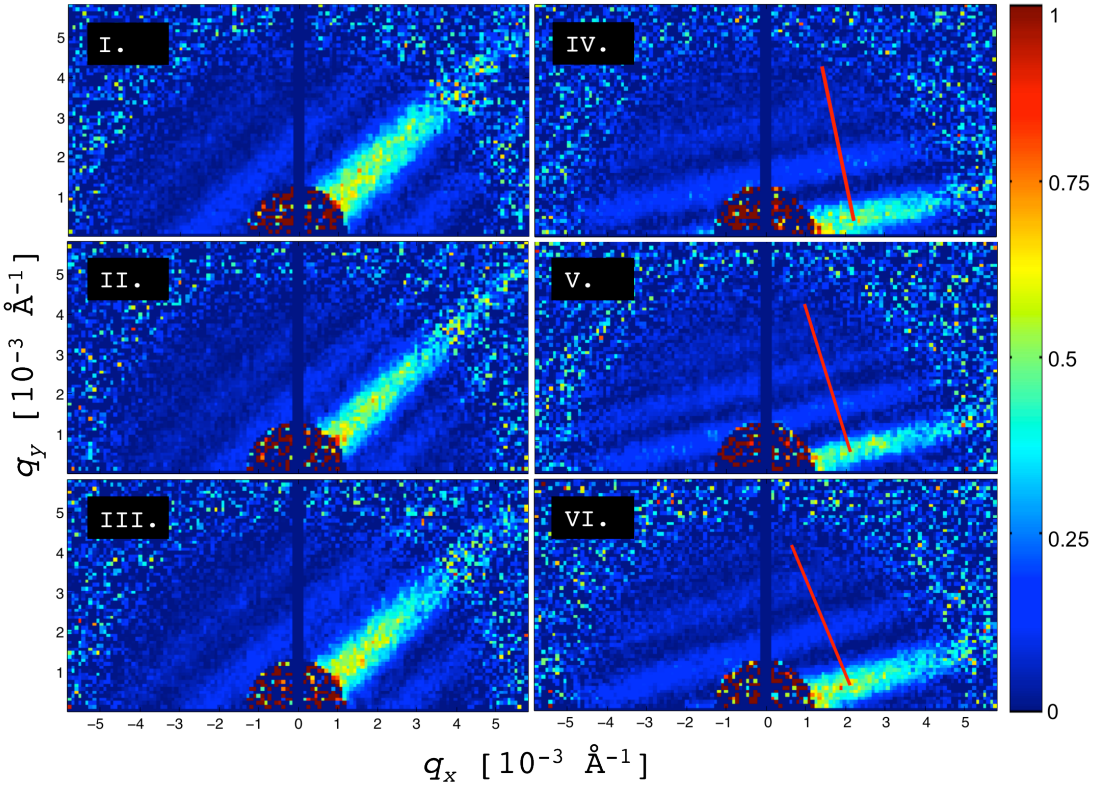

Figure 5.11: Correlation images of six measured points. I. - III. in a straight channel and IV. - VI. in a curved channel with radius 0.5 mm. The flow velocity was 10 µm/s and τ = 20 ms.

The correlation images of the measured spots in curved and straight channel are shown in figure 5.11. For the straight channel, we observe three parallel correlation signals, which is expected, since the flow direction should not change in a linear channel. The width of the streaks shows a higher velocity in the

middle of the channel compared to slower velocities in the outsides (I. and III.). Regarding I. and III., we can also say that the velocities are similar, as the width of the streaks as well as the distances to the first order Doppler signals are comparable.

On pictures IV. to VI., the correlation images of the flow in curve are shown, where IV. is the inmost position and VI. the outmost one. The first feature that can be observed is the change in the general flow direction as we go from the straight section into the curvature. As a second characteristic we can again observe the change in velocity across the channel. The flow at the middle position (V.) is again the fastest, showing a very narrow streak and closely packed Doppler signal. The velocities of the inner and the outer position are very similar, with a slightly narrower streak in image IV., indicating that the velocity is slightly higher at this position. When comparing the flow directions at certain positions in the channel, we observe a rotation of the flow orientation from point IV. (pink) to point VI. (cyan). This is clearly an impact of the geometry, as no change in flow direction can be observed in the straight channel (nor is it expected). The discussed differences in flow direction and velocity are shown as radial intensity plots in figure 5.12.

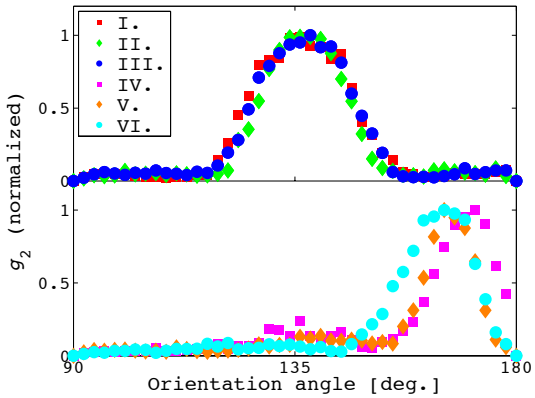

Figure 5.12: Radial intensity plots of images in figure 5.11. I. to III. show no change in position (i.e. flow orientation) while the flow in IV., V. and VI. has different orientations. The impact of the velocity can also be seen, as II. and V. are slightly narrower than the two respective other curves.

Additional to the orientation and the velocity of the flow, we were also interested in the dispersion of the flow orientation inside the sample volume. We expected a larger dispersion at smaller radii (i.e. at the inside of the curve) compared to the outside of the curved channel, as the change in flow direction is larger over a given distance. Figuratively, the difference in flow direction between particles entering and exiting the sample volume (i.e., the X-ray beam) is bigger at smaller radii compared to larger ones. The assumed consequence in the correlation images would be an increasingly smeared out streak from image VI. to IV.. In order to depict this effect, we analysed the intensities of the images IV., V. and VI. along the red lines in figure 5.11. For the main streaks the correlation is too high and thus we do not observe any smearing. However, when comparing the intensities of the Doppler signals plotted in figure 5.13 A, namely the second peak (around 75 relative *q*-value for IV. and VI. and 55 for V.), we get a significant difference in the intensities. There we can see that the peak of the second Doppler signal becomes more prominent with increasing radius (i.e. from image IV. to image VI.)

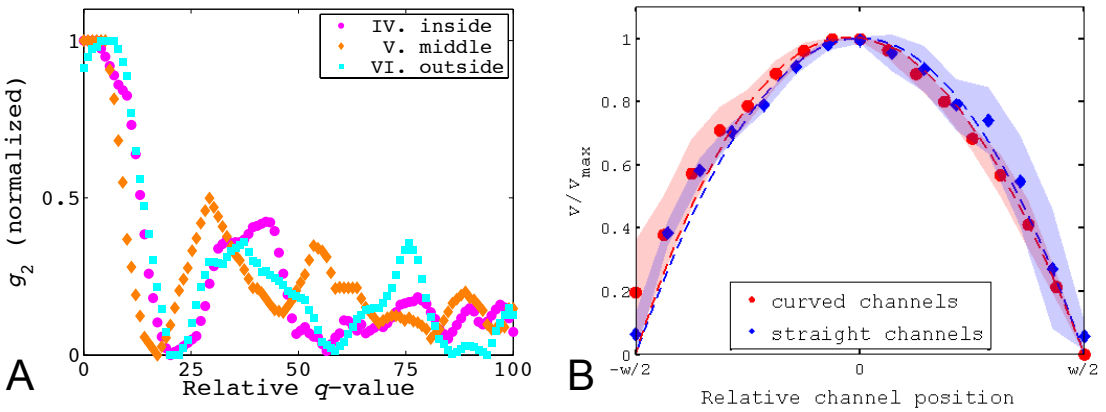

Figure 5.13: Normalized autocorrelation intensities along the red lines in figure 5.11 for the three measurements in the curved channel (A). Flow profiles of straight (blue) and curved (red) channels averaged over 4 and 3 different experiments respectively (B). The coloured area indicates the standard deviation. The velocities were normalized with v_{max} in order to enable the comparison of experiments at different flow velocities. The dashed lines are the calculated flow profiles for the given channel dimensions.

From each of the correlation movies the autocorrelation function in flow direction was extracted. The correlation function was fitted using equation 5.8 to get the flow velocity at that point. The calculated flow profiles of four line scans in straight channels and three line scans in curved channels at different flow velocities were normalized and averaged (figure 5.13 B). The dashed lines show the calculated flow profiles of the corresponding channel geometries for a simple Newtonian fluid. As can be seen, the maximal flow velocity for curved channels is slightly shifted to the centre of the curvature. This effect can also be observed in our measurements for the curved channel, which show a slight offset of the maximal flow speed compared to the blue points of the straight channels.

5.6 Conclusion

Using 160 nm sized particles we studied the flow dynamics in different geometries of a microfluidic device by means of XPCS. An autocorrelation function was calculated for each of the pixels in the scattering image, resulting in a sequence of correlation images, each representing the values of the autocorrelation functions for a given τ. Direct analysis of single correlation images provided information about Brownian motion, the orientation of the flow, its velocity and hence about the geometry of the microfluidic channel. The ability to analyse the full image rather than just one specific q-value is important whenever a possible anisotropy of the device is not known (unlike the situation in a capillary, for instance).

In this way, we could show the flow behaviour in the exit of a narrow constriction, where the direction and the velocity of the flow are changing across the channel. Similarly, we studied the rotation of the flow direction along and across a curved section of the channel. Straightforward analysis of the correlation intensity in flow direction shows the different prominences of correlation signals originating from particles flowing with different velocities (Doppler shifts). In curved channels we could show that a lower radius leads to a

higher dispersion of flow direction and hence the Doppler signals are smeared out and show a lower prominence. All information about these features was accessible in one measurement series, even if the anisotropy of the flow was not known beforehand. This would not be possible with a one dimensional point detector without measuring several q-values.

After analysing the correlation images we could choose and extract the autocorrelation functions at distinct q-values (q_x and q_y). In this way, we were able to access g_2 perpendicular and parallel to the flow direction very precisely. The extracted correlation functions perpendicular to flow direction were fitted in order to get the diffusion coefficient D, which was similar to the one calculated from a no-flow measurement. Fitting g_2 parallel to flow directions, we calculated the flow velocities in the channels. Comparing the flow profiles of straight and curved channels we could show the shift of v_{max} towards smaller radii as predicted by simulations.

5.7 Outlook

With point detectors (i.e. photo diodes) XPCS has been a one-dimensional method for years. The use of a fast 2D detector for XPCS together with the calculation of full q-range correlation image sequences allows fast and intuitive analysis of dynamics in microfluidic devices. Multiple information is obtained in one measurement and pre-experimental knowledge about sample symmetry for instance is no longer needed, as the orientation of the flow is directly visible on the correlation image.

The high intensity third generation (coherent) synchrotron radiation in combination with the rapid developments of fast readout 2D X-ray detectors will surely raise possibilities for this method. The newest generation of 2D X-ray detector, currently under development, will have a frame rate of 22 kHz (Eiger[35]) in full frame mode, compared to a maximal frame rate of 0.3 kHz of the

MAXIPIX[34] used in our experiments. Thus, faster dynamics can be measured and more details observed with a higher temporal resolution.

Measurements of interactions between particles, biomaterials (e.g. proteins) or other macromolecules using XPCS might be possible and hence measuring the changes of these interactions in different environments. In this way, the change of interactions between charged particles upon addition of salt could be investigated. The charge of the individual particles is shielded by the ions of the salt, and thus the electrostatic interactions are strongly influenced, which will change the motion behaviour of the colloids. Figure 5.14 shows a possible setup for a measurement of the screening of electrostatic interactions.

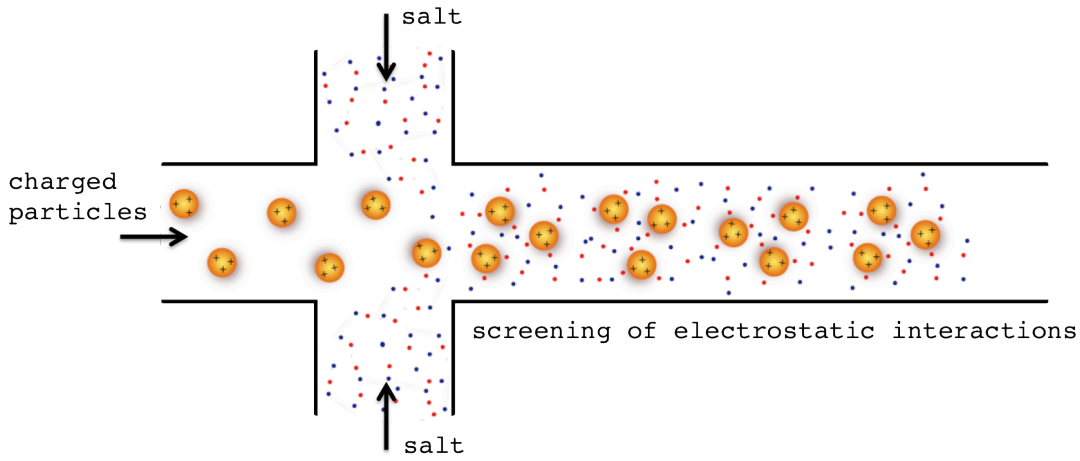

Figure 5.14: Possible setup for measurements of charged particles first without, then with salt. The salt is screening the charge of the particles and hence their interactions change, which affects their dynamics.

Another example of 2D XPCS in microfluidics is the measurement of interlinked particles. This could be small gold particles connected with a short piece of DNA. Measuring the behaviour of the particles in different flow fields (as shown in figure 5.15) provides information about the coiling and stretching of the DNA (or any given polymer) depending on channel geometries.

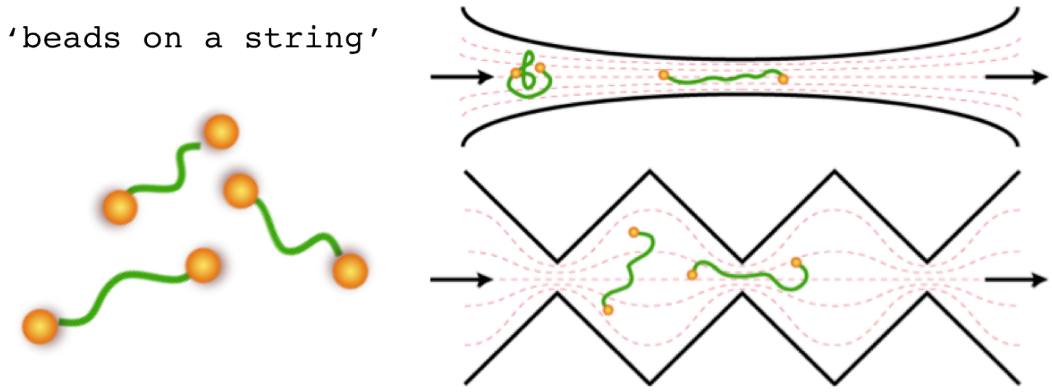

Figure 5.15: Ideas for particles linked with polymers (f.i. DNA). Depending on the channel geometry and the resulting flow field, the polymers crumple or stretch. This could be measured by analysing the movement of the particles using 2D XPCS.

The idea of beads on a string could even be expanded to fully biological systems like DNA-histone complexes. Using 2D XPCS and a microfluidic mixing device, the dynamics of the two binding steps (see figure 5.16) could be analysed by studying the changes in SAXS signals of histones and DNA. The possible implementation of cross correlation with 2D XPCS will be another interesting feature for these and other future applications.

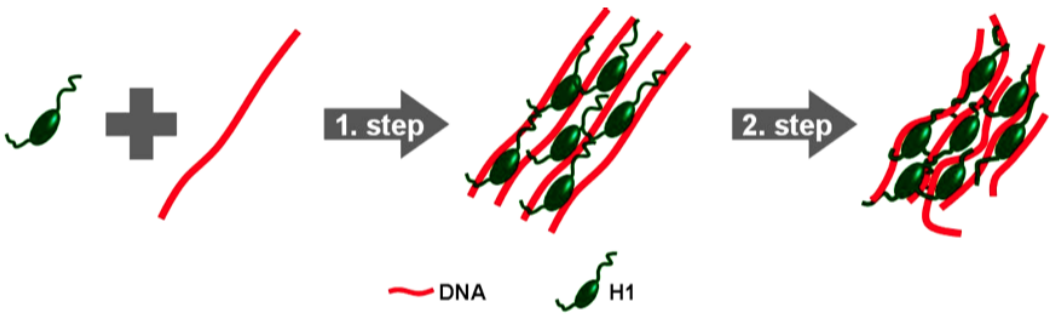

Figure 5.16: Overview of the interaction between DNA and linker histone H1. The compaction takes place in two distinct steps. XPCS could reveal the dynamics of each step. Taken from [158].

Bibliography

(1) Young, A. T. Rayleigh Scattering. *Physics Today* **1982**, *35*, 42–48.

(2) McCartney, E. J. Optics of the Atmosphere: Scattering by Molecules and Particles. *New York, John Wiley and Sons, Inc.* **1976**.

(3) Röntgen, W. C. On a New Kind of Rays. **1896**.

(4) Laue, M. Reflection of X-Rays. *Journal of the Röntgen Society* **1913**.

(5) Friedrich, W.; Knipping, P.; Laue, M. Interferenzerscheinungen Bei Röntgenstrahlen. *Ann. Phys.* **1913**, *346*, 971–988.

(6) Bragg, W. H.; Bragg, W. L. The Reflection of X-Rays by Crystals. *Proceedings of the Royal Society of London* **1913**.

(7) Debye, P. Interferenz Von Röntgenstrahlen Und Wärmebewegung. *Ann. Phys.* **1913**, *348*, 49–92.

(8) Bragg, W. L. Die Struktur Einiger Kristalle, Gedeutet Nach Ihrer Beugung Von Röntgen-Strahlen. *Z. Anorg. Chem.* **1914**, *90*, 185–218.

(9) Robotti, N. The Discovery of X-Ray Diffraction. *Rend. Fis. Acc. Lincei* **2012**, *24*, 7–18.

(10) Thomas, J. M. Centenary: the Birth of X-Ray Crystallography. *Nature* **2012**, *491*, 186–187.

(11) Watson, J. D.; Crick, F. Nature Physics Portal - Looking Back - DNA - a New Twist on Life. *Nature* **1953**.

(12) Schluenzen, F.; Tocilj, A.; Zarivach, R.; Harms, J.; Gluehmann, M.; Janell, D.; Bashan, A.; Bartels, H.; Agmon, I.; Franceschi, F.; *et al.* Structure of Functionally Activated Small Ribosomal Subunit at 3.3 Å Resolution. *Cell* **2000**, *102*, 615–623.

(13) Ramakrishnan, V.; Clemons, W. M.; May, J. L. C.; Wimberly, B. T.; McCutcheon, J. P.; Capel, M. S. Structure of a Bacterial 30S Ribosomal Subunit at 5.5Å Resolution : Abstract : Nature. *Nature* **1999**, *400*, 833–

840.

(14) Ban, N. The Complete Atomic Structure of the Large Ribosomal Subunit at 2.4Å Resolution. *Science* **2000**, *289*, 905–920.

(15) Ehrenberg, W.; Franks, A. Small-Angle X-Ray Scattering. *Nature* **1952**, *170*, 1076–1077.

(16) Guinier, A. Dispositif permettant d'obtenir des diagrammes de diffraction de poudres cristallines tres intenses avec un rayonnement monochromatique. *CR Acad Sci Paris* **1937**.

(17) Kratky, O.; Sekora, A.; Treer, R. Über Die an Kolloiden Systemen Unter Kleinen Winkeln Diffus Abgebeugte Röntgenstrahlung. *Zeitschrift für Elektrochemie und angewandte physikalische Chemie* **1942**.

(18) Debye, P.; Bueche, A. M. Scattering by an Inhomogeneous Solid. *J. Appl. Phys.* **1949**, *20*, 518–525.

(19) Porod, G. Die Röntgenkleinwinkelstreuung von dichtgepackten kolloiden Systemen II. *Kolloid eitschrift.* **1952**.

(20) Guinier, A.; Fournet, G.; Walker, C. B.; Yudowitch, K. L. Small-Angle Scattering of X-Rays. *John Wiley & Sons.* **1955**.

(21) Sisson, W. A. X-Ray Studies of Crystallite Orientation in Cellulose Fibers Natural Fibers. *Ind. Eng. Chem.* **1935**.

(22) Bear, R. S. X-Ray Diffraction Studies on Protein Fibers. I. the Large Fiber-Axis Period of Collagen. *Journal of the American Chemical Society* **1944**, *66*, 1297–1305.

(23) Heyn, A. Small-Angle X-Ray Scattering in Various Cellulose Fibers and Its Relation to the Micellar Structure. *Textile Research Journal* **1949**.

(24) Reinhold, C.; Fischer, E. W.; Peterlin, A. Evaluation of Small-Angle X-Ray Scattering of Polymers. *J. Appl. Phys.* **1964**.

(25) Malmon, A. G. Small Angle X-Ray Scattering Studies of the Size, Shape, and Hydration of Catalase. *Biochimica et biophysica acta* **1957**.

(26) Svergun, D. I. Restoring Low Resolution Structure of Biological Macromolecules From Solution Scattering Using Simulated Annealing. *Biophysical journal* **1999**.

(27) Livet, F. Diffraction with a Coherent X-Ray Beam: Dynamics and Imaging. *Acta Crystallogr Sect A Found Crystallogr* **2007**, *63*, 87–107.

(28) Glatter, O.; Kratky, O. Small Angle X-Ray Scattering. *Academic Press* **1982**.

(29) Guinier, A. La Diffraction Des Rayons X Aux Tres Petits Angles: Applications a L'etude De Phenomenes Ultramicroscopiques. *Paris Masson* **1939**.

(30) Porod, G. Die Röntgenkleinwinkelstreuung Von Dichtgepackten Kolloiden Systemen I. *Kolloid-Zeitschrift* **1951**, *124*, 83–114.

(31) Debye, P.; Anderson, H. R.; Brumberger, H. Scattering by an Inhomogeneous Solid. II. the Correlation Function and Its Application. *J. Appl. Phys.* **1957**, *28*, 679.

(32) Konarev, P. V.; Volkov, V. V.; Sokolova, A. V.; Koch, M. H. J.; Svergun, D. I. PRIMUS: a Windows PC-Based System for Small-Angle Scattering Data Analysis. *Journal of applied crystallography* **2003**, *36*, 1277–1282.

(33) Sutton, M. A Review of X-Ray Intensity Fluctuation Spectroscopy. *Comptes Rendus Physique* **2008**, *9*, 657–667.

(34) Ponchut, C.; Rigal, J. M.; Clément, J.; Papillon, E.; Homs, A.; Petitdemange, S. MAXIPIX, a Fast Readout Photon-Counting X-Ray Area Detector for Synchrotron Applications. *J. Inst.* **2011**, *6*, C01069–C01069.

(35) Johnson, I.; Bergamaschi, A.; Billich, H.; Cartier, S.; Dinapoli, R.; Greiffenberg, D.; Guizar-Sicairos, M.; Henrich, B.; Jungmann, J.; Mezza, D.; *et al.* Eiger: a Single-Photon Counting X-Ray Detector. *J. Inst.* **2014**, *9*, C05032–C05032.

(36) Schavkan, A.; Westermeier, F.; Zozulya, A. Using the MAXIPIX Detector for Coherent X-Ray Scattering Applications - Abstract - Journal of Physics: Conference Series - IOPscience. *Journal of Physics: Conference Series* **2013**.

(37) Whitesides, G. M. The Origins and the Future of Microfluidics. *Nature* **2006**, *442*, 368–373.

(38) Manz, A.; Harrison, D. J.; Verpoorte, E. Planar Chips Technology for

Miniaturization and Integration of Separation Techniques Into Monitoring Systems: Capillary Electrophoresis on a Chip. *Journal of Chromatography* **1992**.

(39) Squires, T. M.; Quake, S. R. Microfluidics: Fluid Physics at the Nanoliter Scale. *Reviews of modern physics* **2005**.

(40) Bruus, H. Bruus: Theoretical Microfluidics. Oxford Master Series in Condensed MAtter Physics. *Oxfort University Press* **2008**.

(41) Batchelor, G. An Introduction to Fluid Mechanics *Press Cambridge UK* **1967**.

(42) Meir, P. G. B. Basics of Fluid Mechanics. Last modified: Version 0.3.4.0. *www.potto.org/downloads.php* **2013**.

(43) Ca, U. Controlled Microfluidic Interfaces. *Nature* **2005**.

(44) Seemann, R.; Brinkmann, M.; Pfohl, T.; Herminghaus, S. Droplet Based Microfluidics. *Rep. Prog. Phys.* **2011**, *75*, 016601.

(45) Zhao, B.; Viernes, N. O. L.; Moore, J. S.; Beebe, D. J. Control and Applications of Immiscible Liquids in Microchannels. *Journal of the American Chemical Society* **2002**, *124*, 5284–5285.

(46) Zhao, B. Surface-Directed Liquid Flow Inside Microchannels. *Science* **2001**, *291*, 1023–1026.

(47) Surmeian, M.; Slyadnev, M. N.; Hisamoto, H.; Hibara, A.; Uchiyama, K.; Kitamori, T. Three-Layer Flow Membrane System on a Microchip for Investigation of Molecular Transport. *Anal. Chem* **2002**, *74*, 2014–2020.

(48) Maruyama, T.; Uchida, J.-I.; Ohkawa, T.; Futami, T.; Katayama, K.; Nishizawa, K.-I.; Sotowa, K.-I.; Kubota, F.; Kamiya, N.; Goto, M. Enzymatic Degradation of P-Chlorophenol in a Two-Phase Flow Microchannel System. *Lab Chip* **2003**, *3*, 308.

(49) Kobayashi, J. A Microfluidic Device for Conducting Gas-Liquid-Solid Hydrogenation Reactions. *Science* **2004**, *304*, 1305–1308.

(50) Giddings, J.; Yang, F.; Myers, M. Flow-Field-Flow Fractionation: a Versatile New Separation Method. *Science* **1976**, *193*, 1244–1245.

(51) Giddings, J. Field-Flow Fractionation: Analysis of Macromolecular,

Colloidal, and Particulate Materials. *Science* **1993**, *260*, 1456–1465.

(52) Williams, P. S.; Levin, S.; Lenczycki, T.; Giddings, J. C. Continuous SPLITT Fractionation Based on a Diffusion Mechanism. *Ind. Eng. Chem. Res.* **1992**, *31*, 2172–2181.

(53) Brody, J. P.; Yager, P.; Goldstein, R. E.; Austin, R. H. Biotechnology at Low Reynolds Numbers. *Biophysical journal* **1996**.

(54) Brody, J. P.; Yager, P. Diffusion-Based Extraction in a Microfabricated Device. *Sensors and Actuators A* **1997**, *58*, 13–18.

(55) Weigl, B. H.; Yager, P. Silicon-Microfabricated Diffusion-Based Optical Chemical Sensor. *Sensors and Actuators B* **1997**.

(56) Hatch, A.; Kamholz, A. E.; Hawkins, K. R.; Munson, M. S.; Schilling, E. A.; Weigl, B. H.; Yager, P. A Rapid Diffusion Immunoassay in a T-Sensor. *Nat Biotechnol* **2001**, *19*, 461–465.

(57) Hansen, C. L.; Skordalakes, E.; Berger, J. M.; Quake, S. R. A Robust and Scalable Microfluidic Metering Method That Allows Protein Crystal Growth by Free Interface Diffusion. *Proceedings of the National Academy of Sciences* **2002**, *99*, 16531–16536.

(58) Deshpande, S.; Pfohl, T. Hierarchical Self-Assembly of Actin in Micro-Confinements Using Microfluidics. *Biomicrofluidics* **2012**, *6*, 034120.

(59) Kakuta, M.; Bessoth, F. G.; Manz, A. Microfabricated Devices for Fluid Mixing and Their Application for Chemical Synthesis. *Chem. Record* **2001**, *1*, 395–405.

(60) Nguyen, N.-T.; Wu, Z. Micromixers—a Review. *J. Micromech. Microeng.* **2004**, *15*, R1–R16.

(61) Kamholz, A. E.; Weigl, B. H.; Finlayson, B. A.; Yager, P. Quantitative Analysis of Molecular Interaction in a Microfluidic Channel: the T-Sensor. *Anal. Chem* **1999**, *71*, 5340–5347.

(62) Kamholz, A. E.; Yager, P. Molecular Diffusive Scaling Laws in Pressure-Driven Microfluidic Channels: Deviation From One-Dimensional Einstein Approximations. *Sensors and Actuators B* **2002**, *82*, 117–121.

(63) Ismagilov, R. F.; Stroock, A. D.; Kenis, P. J. A.; Whitesides, G.; Stone, H. A.

Experimental and Theoretical Scaling Laws for Transverse Diffusive Broadening in Two-Phase Laminar Flows in Microchannels. *Appl. Phys. Lett.* **2000**, *76*, 2376–2378.

(64) Veenstra, T. T.; Lammerink, T. S. J.; Elwenspoek, M. C.; Berg, A. V. D. Characterization Method for a New Diffusion Mixer Applicable in Micro Flow Injection Analysis Systems. *J. Micromech. Microeng.* **1999**, *9*, 199–202.

(65) Golden, J. P.; Justin, G. A.; Nasir, M.; Ligler, F. S. Hydrodynamic Focusing—a Versatile Tool. *Anal Bioanal Chem* **2011**, *402*, 325–335.

(66) Jackman, R. J.; Floyd, T. M.; Ghodssi, R.; Schmidt, M. A.; Jensen, K. F. Microfluidic Systems with on-Line UV Detection Fabricated in Photodefinable Epoxy. *J. Micromech. Microeng.* **2001**, *11*, 263–269.

(67) Mobius, H.; Ehrfeld, W.; Hessel, V.; Richter, T. Sensor Controlled Processes in Chemical Microreactors. *Transducers '95 Eurosensors IX* **1995**.

(68) Branebjerg, J.; Gravesen, P.; Krog, J. P.; Nielsen, C. R. Fast Mixing by Lamination. *MEMS '96 Proceedings* **1996**

(69) Koch, M.; Witt, H.; Evans, A. G. R.; Brunnschweiler, A. Improved Characterization Technique for Micromixers. *J. Micromech. Microeng.* **1999**, *9*, 156–158.

(70) Köster, S.; Pfohl, T. X-Ray Studies of Biological Matter in Microfluidic Environments. *Mod. Phys. Lett. B* **2012**, *26*, 1230018.

(71) Evans, H. M.; Dootz, R.; Köster, S.; Struth, B. X-Ray Microdiffraction on Flow-Controlled Biomolecular Assemblies. Bull. Pol. Ac.: Tech. **2007**.

(72) Martel, A.; Burghammer, M.; Davies, R.; DiCola, E. A Microfluidic Cell for Studying the Formation of Regenerated Silk by Synchrotron Radiation Small- and Wide-Angle X-Ray Scattering. *Biomicrofluidics* **2008**.

(73) Kinahan, M. E.; Filippidi, E.; Köster, S.; Hu, X. Tunable Silk: Using Microfluidics to Fabricate Silk Fibers with Controllable Properties *Biomacromolecules* **2011**.

(74) Brennich, M. E.; Nolting, J. F.; Dammann, C.; Nöding, B. Dynamics of

Intermediate Filament Assembly Followed in Micro-Flow by Small Angle X-Ray Scattering *Lab Chip* **2011**.

(75) Dootz, R.; Toma, A. C.; Pfohl, T. Structural and Dynamic Properties of Linker Histone H1 Binding to DNA. *Biomicrofluidics* **2011**, *5*, 024104.

(76) Dootz, R.; Otten, A.; Köster, S.; Struth, B.; Pfohl, T. Evolution of DNA Compaction in Microchannels. *J. Phys.: Condens. Matter* **2006**, *18*, S639–S652.

(77) Dootz, R.; Toma, A. C.; Pfohl, T. PAMAM6 Dendrimers and DNA: pH Dependent "Beads-on-a-String" Behavior Revealed by Small Angle X-Ray Scattering. *Soft Matter* **2011**, *7*, 8343–8351.

(78) Pfohl, T.; Otten, A.; Köster, S.; Dootz, R.; Struth, B.; Evans, H. M. Highly Packed and Oriented DNA Mesophases Identified Using in Situ Microfluidic X-Ray Microdiffraction. *Biomacromolecules* **2007**, *8*, 2167–2172.

(79) Köster, S.; Evans, H. M.; Wong, J. Y.; Pfohl, T. An in Situ Study of Collagen Self-Assembly Processes. *Biomacromolecules* **2008**, *9*, 199–207.

(80) Köster, S.; Leach, J. B.; Struth, B.; Pfohl, T.; Wong, J. Y. Visualization of Flow-Aligned Type I Collagen Self-Assembly in Tunable pH Gradients. *Langmuir* **2007**, *23*, 357–359.

(81) Pollack, L.; Tate, M. W.; Darnton, N. C.; Knight, J. B.; Gruner, S. M.; Eaton, W. A.; Austin, R. H. Compactness of the Denatured State of a Fast-Folding Protein Measured by Submillisecond Small-Angle X-Ray Scattering. *Proceedings of the National Academy of Sciences* **1999**, *96*, 10115–10117.

(82) Pollack, L.; Tate, M. W.; Finnefrock, A. C.; Kalidas, C.; Trotter, S.; Darnton, N. C.; Lurio, L.; Austin, R. H.; Batt, C. A.; Gruner, S. M.; *et al.* Time Resolved Collapse of a Folding Protein Observed with Small Angle X-Ray Scattering. *Phys. Rev. Lett.* **2001**, *86*, 4962–4965.

(83) Russell, R.; Millett, I. S.; Tate, M. W.; Kwok, L. W.; Nakatani, B.; Gruner, S. M.; Mochrie, S. G. J.; Pande, V.; Doniach, S.; Herschlag, D.; *et al.* Rapid Compaction During RNA Folding. *Proceedings of the National Academy*

of Sciences **2002**, *99*, 4266–4271.

(84) Robinson, I.; Gruebel, G.; Mochrie, S. Focus on X-Ray Beams with High Coherence. *New J. Phys.* **2010**, *12*, 035002.

(85) Utada, A. S. Monodisperse Double Emulsions Generated From a Microcapillary Device. *Science* **2005**, *308*, 537–541.

(86) Barrett, R.; Faucon, M.; Lopez, J.; Cristobal, G.; Destremaut, F.; Dodge, A.; Guillot, P.; Laval, P.; Masselon, C.; Salmon, J.-B. X-Ray Microfocussing Combined with Microfluidics for on-Chip X-Ray Scattering Measurements. *Lab Chip* **2006**, *6*, 494–499.

(87) Otten, A.; Köster, S.; Struth, B.; Snigirev, A.; Pfohl, T. Microfluidics of Soft Matter Investigated by Small-Angle X-Ray Scattering. *J Synchrotron Rad* **2005**, *12*, 745–750.

(88) Dootz, R.; Evans, H.; Köster, S.; Pfohl, T. Rapid Prototyping of X-Ray Microdiffraction Compatible Continuous Microflow Foils. *Small* **2007**, *3*, 96–100.

(89) Yadav, M. K.; Gerdts, C. J.; Sanishvili, R.; Smith, W. W.; Roach, L. S.; Ismagilov, R. F.; Kuhn, P.; Stevens, R. C. In Situdata Collection and Structure Refinement From Microcapillary Protein Crystallization. *Journal of applied crystallography* **2005**, *38*, 900–905.

(90) Zheng, B.; Tice, J. D.; Roach, L. S.; Ismagilov, R. F. A Droplet-Based, Composite PDMS/Glass Capillary Microfluidic System for Evaluating Protein Crystallization Conditions by Microbatch and Vapor-Diffusion Methods with on-Chip X-Ray Diffraction. *Angew. Chem. Int. Ed.* **2004**, *43*, 2508–2511.

(91) Kratky, O. Neues Verfahren Zur Herstellung Von Blendenstreuungsfreien Röntgen-Kleinwinkelaufnahmen. *Zeitschrift für Elektrochemie* **1954**.

(92) Jørgensen, J. M.; Erlacher, K.; Pedersen, J. S.; Gothelf, K. V. Preparation Temperature Dependence of Size and Polydispersity of Alkylthiol Monolayer Protected Gold Clusters. *Langmuir* **2005**, *21*, 10320–10323.

(93) Sundblom, A.; Oliveira, C. L. P.; Palmqvist, A. E. C.; Pedersen, J. S.

Modeling in Situ Small-Angle X-Ray Scattering Measurements Following the Formation of Mesostructured Silica. *J. Phys. Chem. C* **2009**, *113*, 7706–7713.

(94) Polte, J.; Erler, R.; Thuenemann, A. F.; Sokolov, S.; Ahner, T. T.; Rademann, K.; Emmerling, F.; Kraehnert, R. Nucleation and Growth of Gold Nanoparticles Studied via in Situ Small Angle X-Ray Scattering at Millisecond Time Resolution. *Acs Nano* **2010**, *4*, 1076–1082.

(95) Angelov, B.; Angelova, A.; Mutafchieva, R.; Lesieur, S.; Vainio, U.; Garamus, V. M.; Jensen, G. V.; Pedersen, J. S. SAXS Investigation of a Cubic to a Sponge (L3) Phase Transition in Self-Assembled Lipid Nanocarriers. *Phys. Chem. Chem. Phys.* **2011**, *13*, 3073.

(96) Parnell, A. J.; Cadby, A. J.; Mykhaylyk, O. O.; Dunbar, A. D. F.; Hopkinson, P. E.; Donald, A. M.; Jones, R. A. L. Nanoscale Phase Separation of P3HT PCBM Thick Films as Measured by Small-Angle X-Ray Scattering. *Macromolecules* **2011**, *44*, 6503–6508.

(97) Hirose, R.; Yoshioka, T.; Yamamoto, H.; Reddy, K. R.; Tahara, D.; Hamada, K.; Tashiro, K. In-House Simultaneous Collection of Small-Angle X-Ray Scattering, Wide-Angle X-Ray Diffraction and Raman Scattering Data From Polymeric Materials. *Journal of applied crystallography* **2014**, *47*, 922–930.

(98) Fischer, B.; Wagner, J.; Gutt, C.; Westermeier, F.; Grübel, G. Structure and Dynamics of Glassy Charged Colloids Studied with Coherent Small Angle X-Ray Scattering. *J. Phys.: Conf. Ser.* **2010**, *247*, 012026.

(99) Stöber, W.; Fink, A.; Bohn, E. Controlled Growth of Monodisperse Silica Spheres in the Micron Size Range. *Journal of Colloid and Interface Science* **1968**.

(100) Misic, Z.; Muffler, K.; Sydow, G.; Kuentz, M. Novel Starch-Based PVA Thermoplastic Capsules for Hydrophilic Lipid-Based Formulations. *J. Pharm. Sci.* **2012**, *101*, 4516–4528.

(101) Misic, Z.; Urbani, R.; Pfohl, T.; Muffler, K.; Sydow, G.; Kuentz, M. Understanding Biorelevant Drug Release From a Novel Thermoplastic

Capsule by Considering Microstructural Formulation Changes During Hydration. *Pharm Res* **2013**, *31*, 194–203.

(102) Rogers, J. A.; Nuzzo, R. G. Recent Progress in Soft Lithography. *Materials Today* **2005**, *8*, 50–56.

(103) Anderson, J. R.; Chiu, D. T.; Wu, H. Fabrication of Microfluidic Systems in Poly (Dimethylsiloxane). *Electrophoresis* **2000**.

(104) Whitesides, G.; Stroock, A. Flexible Methods for Microfluidics. *Phys Today* **2001**.

(105) Levenberg, K. A Method for the Solution of Certain Problems in least squares. *J Appl Math* **1944**.

(106) Marquardt, D. W. Least-Squares Estimation of Nonlinear. Parameters. *A Fortran IV Program* **1966**.

(107) Gauß, C. F. Theoria Motvs Corporvm Coelestivm in Sectionibvs Conicis Solem Ambientivm. *Hambvrgi Svmtibvs Rid. Pertes et I. H. Besser* **1809**.

(108) Svergun, D. I.; Koch, M. H. J. Small-Angle Scattering Studies of Biological Macromolecules in Solution. *Rep. Prog. Phys.* **2003**, *66*, 1735–1782.

(109) Reich, G. Formulation and Physical Properties of Soft Capsules. *Pharmaceutical Press* **2004**.

(110) Achieve, H. Oral Lipid-Based Formulations: Enhancing the Bioavailability of Poorly Water-Soluble Drugs. *Pharmaceutical Press* **2013**.

(111) López-Montilla, J. C.; Herrera-Morales, P. E. Spontaneous Emulsification: Mechanisms, Physicochemical Aspects, Modeling, and Applications. *J. Dispersion Science and Technology* **2002**.

(112) Pouton, C. W. Formulation of Self-Emulsifying Drug Delivery Systems. *Advanced drug delivery reviews* **1997**.

(113) Regev, O.; Ezrahi, S.; Aserin, A.; Garti, N.; Wachtel, E.; Kaler, E. W.; Khan, A.; Talmon, Y. A Study of the Microstructure of a Four-Component Nonionic Microemulsion by Cryo-TEM, NMR, SAXS, and SANS. *Langmuir* **1996**, *12*, 668–674.

(114) Biradar, S. V.; Dhumal, R. S.; Paradkar, A. R. Rheological Investigation of

Self-Emulsification Process: Effect of Co-Surfactant. *Journal of Pharmacy & Pharmaceutical Sciences* **2009**, *12*, 164–174.

(115) Patil, S. S.; Venugopal, E.; Bhat, S.; Mahadik, K. R.; Paradkar, A. R. Microstructural Elucidation of Self-Emulsifying System: Effect of Chemical Structure. *Pharm Res* **2012**, *29*, 2180–2188.

(116) Patil, S. S.; Venugopal, E.; Bhat, S.; Mahadik, K. R.; Paradkar, A. R. Probing Influence of Mesophasic Transformation on Performance of Self-Emulsifying System: Effect of Ion. *Mol. Pharmaceutics* **2012**, *9*, 318–324.

(117) Fanun, M. Oil Type Effect on Diclofenac Solubilization in Mixed Nonionic Surfactants Microemulsions. *Colloids and Surfaces A: Physicochemical and Engineering Aspects* **2009**.

(118) Teubner, M.; Strey, R. Origin of the Scattering Peak in Microemulsions. *J. Chem. Phys.* **1987**, *87*, 3195–3200.

(119) Hoar, T. P.; Schulman, J. H. Transparent Water-in-Oil Dispersions: the Oleopathic Hydro-Micelle. *Nature* **1943**, *152*, 102–103.

(120) Danielsson, I.; Lindman, B. Danielsson: the Definition of Microemulsion. *Colloids and Surfaces* **1981**.

(121) Robb, I. D. Microemulsions. *Springer US* **1982**.

(122) Lichterfeld, F.; Schmeling, T.; Strey, R. Microstructure of Microemulsions of the System Water-N-Tetradecane-Alkyl Polyglycol Ether (C12E5). *J. Phys. Chem.* **1986**, *90*, 5762–5766.

(123) Auvray, L.; Cotton, J. P.; Ober, R.; Taupin, C. Evidence for Zero Mean Curvature Microemulsions. *J. Phys. Chem.* **1984**, *88*, 4586–4589.

(124) Guest, D.; Auvray, L.; Langevin, D. Persistence Length Measurements in Middle Phase Microemulsions. *J. Phyique Lett.* **1985**, *46*, 1055–1063.

(125) Debye, P.; Menke, H. The Determination of the Inner Structure of liquids by X-ray means. *Physikal Zeit* **1930**.

(126) Zernike, F.; Prins, J. A. The Bending of X-Rays in Liquid as an Effect. *Z Phys* **1927**.

(127) Griffiths, R. B. Thermodynamic Model for Tricritical Points in Ternary

and Quaternary Fluid Mixtures. *J. Chem. Phys.* **1974**, *60*, 195.

(128) Kilpatrick, P. K.; Gorman, C. A.; Davis, H. T. Patterns of Phase Behavior in Ternary Ethoxylated Alcohol-N-Alkane-Water Mixtures. *J. Phys. Chem.* **1986**.

(129) Kahlweit, M.; Strey, R. Phase Behavior of Ternary Systems of the Type H2O-Oil-Nonionic Amphiphile (Microemulsions). *Angew. Chem. Int. Ed.* **1985**, *24*, 654–668.

(130) Abe, M.; Schechter, D.; Schechter, R. S.; Wade, W. H.; Weerasooriya, U.; Yiv, S. Microemulsion Formation with Branched Tail Polyoxyethylene Sulfonate Surfactants. *Journal of Colloid and Interface Science* **1986**, *114*, 342–356.

(131) Kahlweit, M.; Lessner, E.; Strey, R. Influence of the Properties of the Oil and the Surfactant on the Phase Behavior of Systems of the Type Water-Oil-Nonionic Surfactant. *J. Phys. Chem.* **1983**, *87*, 5032–5040.

(132) Kahlweit, M.; Strey, R.; Firman, P.; Haase, D. Phase Behavior of Ternary Systems: Water-Oil-Nonionic Surfactant as a Near-Tricritical Phenomenon. *Langmuir* **1985**, *1*, 281–288.

(133) Kahlweit, M.; Strey, R.; Firman, P. Search for Tricritical Points in Ternary Systems: Water-Oil-Nonionic Amphiphile. *J. Phys. Chem.* **1986**, *90*, 671–677.

(134) Bromberg, S.; Dill, K. Molecular Driving Forces. *New York: Garland Science* **2002**.

(135) Landau, L. D.; Lifshitz, E. M. Statistische Physik. *Berlin: Akademie-Verlag* **1984**.

(136) Nič, M.; Jirát, J.; Košata, B.; Jenkins, A.; McNaught, A. IUPAC Compendium of Chemical Terminology 2nd ed. *IUPAC: Research Triagle Park, NC* **2009**.

(137) Cahn, J. W.; Hilliard, J. E. Free Energy of a Nonuniform System. I. Interfacial Free Energy. *J. Chem. Phys.* **1958**.

(138) Fisher, M. E. Correlation Functions and the Critical Region of Simple Fluids. *J. Math. Phys.* **1964**, *5*, 944.

(139) Chen, S. H.; Chang, S. L.; Strey, R.; Samseth, J. Structural Evolution of Bicontinuous Microemulsions. *J. Phys. Chem.* **1991**.

(140) Chen, S. H.; Chang, S. L.; Strey, R. On the Interpretation of Scattering Peaks From Bicontinuous Microemulsions. In *Trends in Colloid and Interface Science IV* **1990**; 81, pp. 30–35.

(141) Peters, C. W. B.; Kruse, U.; Pollwein, R.; Grzeschik, K.-H.; Sippel, A. E. The Human Lysozyme Gene. Sequence Organization and Chromosomal Localization. *Eur J Biochem* **1989**, *182*, 507–516.

(142) Revenis, M. E.; Kaliner, M. A. Lactoferrin and Lysozyme Deficiency in Airway Secretions: Association with the Development of Bronchopulmonary Dysplasia. *The Journal of Pediatrics* **1992**, *121*, 262–270.

(143) Sen, D. K.; Sarin, G. S. Immunoassay of Tear Lysozyme in Conjunctival Diseases. *British Journal of Ophthalmology* **1982**, *66*, 732–735.

(144) Lönnerdal, B. Nutritional and Physiologic Significance of Human Milk Proteins. *The American Journal of Clinical Nutrition* **2003**.

(145) Wildegger, G.; Kiefhaber, T. Three-State Model for Lysozyme Folding: Triangular Folding Mechanism with an Energetically Trapped Intermediate. *J Mol Biol* **1997**.

(146) Segel, D. J.; Bachmann, A.; Hofrichter, J.; Hodgson, K. O.; Doniach, S.; Kiefhaber, T. Characterization of Transient Intermediates in Lysozyme Folding with Time-Resolved Small-Angle X-Ray Scattering. *J Mol Biol* **1999**, *288*, 489–499.

(147) Weise, H. The Tesla X-Fel Project. *Proceedings of EPAC* **2004**.

(148) Patterson, B. D.; Abela, R.; Braun, H.-H.; Flechsig, U.; Ganter, R.; Kim, Y.; Kirk, E.; Oppelt, A.; Pedrozzi, M.; Reiche, S.; *et al.* Coherent Science at the SwissFEL X-Ray Laser. *New J. Phys.* **2010**, *12*, 035012.

(149) Lieberman-Aiden, E.; van Berkum, N. L.; Williams, L.; Imakaev, M.; Ragoczy, T.; Telling, A.; Amit, I.; Lajoie, B. R.; Sabo, P. J.; Dorschner, M. O.; *et al.* Comprehensive Mapping of Long-Range Interactions Reveals Folding Principles of the Human Genome. *Science* **2009**, *326*, 289–293.

(150) Grübel, G.; Zontone, F. Correlation Spectroscopy with Coherent X-Rays. *Journal of alloys and compounds* **2004**.

(151) Sutton, M.; Mochrie, S. G. J.; Greytak, T.; Nagler, S. E.; Berman, L. E.; Held, G. A.; Stephenson, G. B. Observation of Speckle by Diffraction with Coherent X-Rays. *Nature* **1991**, *352*, 608–610.

(152) Dierker, S.; Pindak, R.; Fleming, R.; Robinson, I.; Berman, L. X-Ray Photon Correlation Spectroscopy Study of Brownian Motion of Gold Colloids in Glycerol. *Phys. Rev. Lett.* **1995**, *75*, 449–452.

(153) Burghardt, W. R.; Sikorski, M.; Sandy, A. R.; Narayanan, S. X-Ray Photon Correlation Spectroscopy During Homogenous Shear Flow. *Physical Review E* **2012**, *85*, 021402–021402.

(154) Falus, P.; Borthwick, M. A.; Mochrie, S. Fluctuation Dynamics of Block Copolymer Vesicles. *Phys. Rev. Lett.* **2005**.

(155) Fluerasu, A.; Moussaïd, A.; Falus, P.; Gleyzolle, H.; Madsen, A. X-Ray Photon Correlation Spectroscopy Under Flow. *J Synchrotron Rad* **2008**, *15*, 378–384.

(156) Busch, S.; Jensen, T. H.; Chushkin, Y.; Fluerasu, A. Dynamics in Shear Flow Studied by X-Ray Photon Correlation Spectroscopy. *Eur. Phys. J. E* **2008**, *26*, 55–62.

(157) Narayanan, T.; Cheung, C.; Tong, P.; Goldburg, W. I.; Wu, X.-L. Measurement of the Velocity Difference by Photon Correlation Spectroscopy: an Improved Scheme. *Applied optics* **1997**, *36*, 7639–7644.

(158) Dootz, R. Tuning DNA Compaction. *Georg-August Universität Göttingen, Fakultät für Physik* **2008**.

Acknowledgments

Of course such a thesis and all the work associated to it is not done by itself. Neither can one man alone achieve anything similar without help. Help in any sense you can possibly think of, materialistic, intellectual or just by trusting you and your actions. In my case I feel grateful to a whole bunch of people, some of them might not even have thought about the expression “help”, when they actually helped me, but for me it meant the world. It’s the occasion here, to say thank you, thank you for making this happen.

“Every good leader needs a big cup of coffee.” Well I’m sure you used it a lot, Thomas, as you surely needed a lot of patience during the last years. When I started, you were proud to announce your first Swiss PhD (even before Stefan Willitsch had one), however, I never felt reduced to that position only, as every member of your group gets a lot of respect and even more important a good portion of trust at any time! I had the opportunity to work on many interesting (also some less interesting) projects during my time and I would like to thank you for this possibility. You were not only a good mentor, but also a jolly fellow during all group activities, which is at least of similar importance (to me).

Very important of course were the people, who directly participated in my projects. Fabian Westermeier, you did not only provide us with the colloids for XPCS measurements, but also guaranteed a smooth working process at DESY. The same holds true for Bernd Struth, who also participated in many other visits at PETRA III in Hamburg, and always brought a nice atmosphere to the hutch. A special thanks goes to Benni for analysing loads of XPCS data, surely not the most entertaining thing you ever did, but very important, thank you! From DESY to SLS; Ivan, we (Marzia and me that is) started calling you “il gigante buono”, freely

translated “the good-natured giant” and I actually couldn’t find a better way to describe your patience, your friendliness and your helpfulness during our stays at PSI! My gratitude also goes to Andreas Menzel, Marianne and Ana who were always helpful when we visited the cSAXS beamline. Another thanks goes to Adi, who willingly helped with confocal microscopy, something I have never done before.

I would especially like to thank all the people involved in collaborations that working with SAXS made possible. Jens, your gold particles drove me nuts sometimes. Should there be dumbbells or not? I was never sure if what we measured was what you expected. However, this project was the perfect introduction to the work with X-ray scattering and its methods of analysis for me. Kasper, well, you do not only belong here because we worked together. I’m not sure if I had taken this position without knowing that you are just one floor below. We had a sometimes bit unbalanced work-life-balance… But I enjoyed every minute and I am very happy, that it even ended in a fruitful collaboration. I have never heard of self-emulsifying systems before. Thanks to Zdravka, I know quite a bit about them by know. This was surely one of the most challenging collaborations, not only because the topic was completely new for me, but also because of this pesky book we tried to find everywhere.
There were several other small projects that did not (yet) end in publications unfortunately. Nevertheless, they made my work even more interesting: another round of thermosomes with Tinu, calcification of serum with Andreas Pasch, scanning teeth with Lucy or liposomes with Marzia. You all again and again showed me, how versatile and exciting “my” machine is.

So far about pure science, but everyone knows, that working without a good atmosphere is very hard, if not impossible. I stayed a long time in this group, maybe a bit too long. However, many nice personalities crossed my way due to this. First I would like to mention Eric; I went to Göttingen to learn about microfluidics from you, my first steps with soft lithography, PDMS molds and

syringe pumps were under your supervision. Soon after we discovered our common love for bicycles, and I was very happy to show you some nice spots of my “bike-city”, Basel, although you had hard times to understand my German. A very important part when you start something new, are always the more experienced co-workers. Adriana, you spent hours of building up the labs in Basel, you did the first SAXS measurements with me. And you always joined our group trips, although it was obvious that you didn’t really enjoy them completely. Axel, now you even finish before me, tststs ;-). We were not meant to become friends, sometimes it just doesn’t happen. Still we had some great moments together, like the conference in Budapest, or the skiing trip in Sedrun (“I hate you, I really do! Honestly!”). Natalja, I can’t deny it, I was happy when I heard from Thomas that you should also do SAXS, and take over some measurements for externals. You had a tough start with the machine and its software. Many times I heard you saying: “what should I do when you’re gone?” It will soon be there, this point, and guess what? I’m very confident that you will manage this SAXS story very well, and even better than me. I would also like to thank you for some image that you willingly gave me to use in this thesis. Starting with two PhD students and one post doc, we had crowded offices full with six PhD students and several master and project students after the two Michaels joined. Michael? Michi? Mike? Michael G.? Difficult to distinguish between the two. “Sitz-Michi” and “Steh-Michi” seemed to be two possibilities that Nora introduced. I don’t see both of you very often, as you don’t share my office, or not even the institute in case of “Steh-Michi”. Still you were both always very comfortable to work or discuss with. Nora, I’m sorry, I didn’t want to put you under pressure by saying you were Siddharths replacement. I was just happy that having you next to my desk didn’t feel strange at all, “au contraire”, it was always a joy to talk or even gossip with you! I would also like to thank Cora, with your experience and widespread biological knowledge, you brought many new aspects into our group. I am also very grateful for correcting my thesis, I am sure this helps me a lot to improve my scientific writing.

There were many project students in our group during these years. Most of them were not supervised by me, but many of them still returned to our office and asked a question now and then. Some of them even joined beamtimes at synchrotron. And surely all of them contributed to the nice atmosphere in our group. At last the two master students, Zoe and Joel. You both stayed for a long time, considering you were doing "only" a master thesis. I guess this is also a proof of the good spirit in our group.

Did I forget someone? I didn't, because this guy needs his own paragraph. I think it says everything when I state that four years with you seemed to pass by faster than one year without you. Siddhu, thanks for being here, I hope we will have many joyful moments together in the future as we had them in the past! Remember the Becks Lime we put outside the window in Göttingen? I bet it must still be there, as we really didn't like it. I still can't avoid laughing when I think of the short episode on the stairs with Karthik (is that the right spelling?), or the future president of India, trying to shutdown shutdown shutdown three times. One of the most touching moments for me though was the day when India won the championship. I would have understood if you wanted to celebrate with other Indians, I mean, there are plenty, haha! But no, you preferred celebrating with me, as you brought cricket close to me, and taught me everything about it. I am a bit sad though, that you can't make it for my defence, but maybe I'll show you the presentation another time.

Another very important thanks goes to the mechanical workshop. You guys are awesome! First of course I want to thank you for producing the holder for our microfluidic devices and other parts we needed for our sessions at various synchrotrons. But also beside that, Dieter Wild and especially Philipp and Grischa never denied help or a favour. Even after their official opening hours, when I thought I'm already lost, I found someone down in the basement to help me. Thank you guys! Keep up the great work!

Many other, sometimes unseen people are actually essential for a smoothly operating department. Danni, we joked a lot and whenever I needed something I couldn't find anywhere else, I asked you. Most of the time successfully! I hope not every packet will be as difficult to handle as the ones we tried to send to Bruker (and back). Maya, thank you for keeping bills and stuff organized. You never lost patience, even when I forgot to handle a very important bill. In every building, there is this one guy, who knows everything, and can handle almost everything. The German expression “Mädchen für alles” is probably not respectful enough, but without Jean-Pierre and his perceptive ways to help in any problem you could possibly think of, I think this house would quickly go down. Many others helped me with smaller or bigger problems, Urs and Mike with computers and computer software, Georg with electronics and Anatoly with Labview issues. Thanks to all of you!
Talking about making things working there is one guy not to forget. Arek, I’m sorry for calling you so often, whenever the SAXS machine was broken. Although you are a very nice guy, I wish we didn’t have to meet so often during my PhD. On the other hand, I learned a lot from you so your visits became rarer over time and I could fix more things by myself.

Willy, haha, we fought a lot when we were kids but from the moment we didn’t live in the same spot anymore, a friendship started forming more and more. I am very happy to call you not only my sister but also a very good friend! Thanks a lot also for correcting my limited English writing and for not stopping with critical comments! Haha, I’m sure even in this short paragraph you would find some unnecessary comas.

At last I have to thank my friends and my family, first of all of course Petra, my girlfriend. I am not sure who of us suffered more during the last weeks and months. I very often felt like a zombie at home, just wanting to hang around and I’m sure you noticed this as well. Thanks for being patient, and doing one or the other of actually my works in our household as well. I am looking so much

forward to our next challenge, which will be something completely different and hopefully bring us even more together.

My parents, I would like to thank you for all the support during my education. Not only the financial support, but also the pride you showed when a new step was achieved, although you didn't always manage to show it as much as you felt it. I hope you understand a little bit of my work here, and much more how much it means to me to have finished this chapter as well. Omi ☺, yes I know you didn't like being called like this, but you never really complained and you always had an open ear for my problems. Your enthusiasm for topics, my sister and me were studying was always surprising me. Suddenly you came up with a newspaper article about some nanotechnology or whatever other scientific news. Thanks, for being a great grandmother at all times I hope you can forgive me that my last feelings towards you were not the best; may you rest in peace.

Well, I have been very lucky during my life so far, having many friends along with me. Two of them I already mentioned (Siddhu and Willy) but many more didn't refuse a helpful hand or a calming word whenever needed. I would like to thank all of you. Stef and Petra for encouraging me whenever I was doubting my PhD decision, they both know how to go through this and I'm very glad to count you to my best friends. Bref and Walthi, haha, we all finish at almost the same time and everybody knows, that doing something "together" makes it much easier. Many more of you were always kind and open eared. Meret, I will miss our coffee breaks, Hermeto, lets go on talking about anything (but usually girls), Sevi and Sandra, you belong to me as much as my family, I hope I will have more time for you in the future! And at last my unihockey team mates, your constant questions about the end of my PhD were probably the best motivation to finally finish it!

Again, thanks to all of you for being part of my PhD, of my studies in Basel or of my life in general. I hope we will all have a good time together in the future as well.

Publications and meeting

Publications

Urbani, R., Westermeier, F., Banusch, B., Sprung M., Struth, B., & Pfohl, T. Full *q*-range XPCS scanning microscopy. *In preparation*.

Renggli, K., Nussbaumer, M. G., **Urbani, R.**, Pfohl, T., & Bruns, N. (2014). A Chaperonin as Protein Nanoreactor for Atom-Transfer Radical Polymerization. *Angewandte Chemie International Edition*, *53*(5), 1443-1447.

Misic, Z., **Urbani, R.**, Pfohl, T., Muffler, K., Sydow, G., & Kuentz, M. (2014). Understanding Biorelevant Drug Release from a Novel Thermoplastic Capsule by Considering Microstructural Formulation Changes During Hydration. *Pharmaceutical research*, *31*(1), 194-203.

Hermes, J. P., Sander, F., Fluch, U., Peterle, T., Thompson, D., **Urbani, R.**, ... & Mayor, M. (2012). Monofunctionalized Gold Nanoparticles Stabilized by a Single Dendrimer Form Dumbbell Structures upon Homocoupling. *Journal of the American Chemical Society*, *134*(36), 14674-14677.

Hermes, J. P., Sander, F., Peterle, T., **Urbani, R.**, Pfohl, T., Thompson, D., & Mayor, M. (2011). Gold Nanoparticles Stabilized by Thioether Dendrimers. *Chemistry-A European Journal*, *17*(48), 13473-13481.

Urbani, R., Evans, H. M., & Pfohl, T. (2011, August). Encapsulation and study of fibrillar networks in nanocompartments. In *EUROPEAN BIOPHYSICS JOURNAL*

WITH BIOPHYSICS LETTERS (Vol. 40, pp. 94-95). 233 SPRING ST, NEW YORK, NY 10013 USA: SPRINGER.

Meetings

2013	Swiss Nano Convention, Basel, Switzerland (poster)
2013	DPG spring meeting, Regensburg, Germany (poster)
2011	EBSA European Biophysics Congress, Budapest, Hungary (poster)
2010	International Nano Bio Conference, Zürich, Switzerland (poster)